

Air Force Institute of Technology

AFIT Scholar

Theses and Dissertations

Student Graduate Works

2-2004

Outside Loop Control in Asymmetrical Trimmed Flight Conditions

Gary D. Miller

Follow this and additional works at: <https://scholar.afit.edu/etd>



Part of the [Navigation, Guidance, Control and Dynamics Commons](#)

Recommended Citation

Miller, Gary D., "Outside Loop Control in Asymmetrical Trimmed Flight Conditions" (2004). *Theses and Dissertations*. 3930.

<https://scholar.afit.edu/etd/3930>

This Thesis is brought to you for free and open access by the Student Graduate Works at AFIT Scholar. It has been accepted for inclusion in Theses and Dissertations by an authorized administrator of AFIT Scholar. For more information, please contact AFIT.ENWL.Repository@us.af.mil.



**OUTER-LOOP CONTROL IN ASYMMETRICAL
TRIMMED FLIGHT CONDITIONS**

THESIS

Gary D. Miller, Captain, USAF

AFIT/GAE/ENY/04-M12

**DEPARTMENT OF THE AIR FORCE
AIR UNIVERSITY**

AIR FORCE INSTITUTE OF TECHNOLOGY

Wright-Patterson Air Force Base, Ohio

APPROVED FOR PUBLIC RELEASE; DISTRIBUTION UNLIMITED.

The views expressed in this thesis are those of the author and do not reflect the official policy or position of the United States Air Force, Department of Defense, or the United States Government.

AFIT/GAE/ENY/04-M12

OUTER-LOOP CONTROL IN ASYMMETRICAL TRIMMED FLIGHT CONDITIONS

THESIS

Presented to the Faculty

Department of Aeronautical and Astronautical Engineering

Graduate School of Engineering and Management

Air Force Institute of Technology

Air University

Air Education and Training Command

In Partial Fulfillment of the Requirements for the

Degree of Master of Science in Aeronautical Engineering

Gary D. Miller, BS

Captain, USAF

February 2004

APPROVED FOR PUBLIC RELEASE; DISTRIBUTION UNLIMITED.

AFIT/GAE/ENY/04-M12

OUTER-LOOP CONTROL IN ASYMMETRICAL TRIMMED FLIGHT CONDITIONS

Gary D. Miller, BS
Captain, USAF

Approved:

David R. Jacques, Professor, USAF (Advisor)

date

Meir Pachter, Professor, AFIT (Reader)

date

Russell G. Adelgren, Maj, USAF (Reader)

date

Abstract

Traditionally flight control systems have used linearized equations of motion solved around a single trim point. This thesis proposes a nested-loop controller directly solved from the equations of motion.

The control equations were developed as a solution to asymmetrically trimmed flight conditions. A two-loop design was proposed for the controller. The outer loop modeled the aircraft as a point mass and all forces were balanced to find the aircraft states. The equations input the control variables and output the aircraft states. The inner-loop utilizes the six-degree of freedom model of the aircraft to solve the moment equations. With the input states, the required control surface deflections are calculated.

The control equations were investigated for typical flight conditions to find the predicted aircraft control settings. The control equations were implemented using aeromodel data for a Learjet-25. The aeromodel data was updated in flight test. The predictions from the control equations were then compared to flight test results. The model was able to predict the required elevator deflection for simple longitudinal cases in level and climbing flight to within tolerances. The simple lateral-directional cases were not as accurate as the longitudinal investigations. As complex maneuvers were investigated, the model predictions did not match the flight test results. The complex maneuvers were not reproduced in flight test to match the flight parameters calculated with the model. Also the lateral-directional stability derivatives and measurements had larger errors than the longitudinal variables.

Acknowledgements

I would like to express my sincere appreciation the HAVE TRIM test team at United States Air Force Test Pilot School, including 1Lt Fabrizio “Beast” Beccarisi, Capt Matt “Sieg” Higer, Capt “Dragon” Teichert, and Capt Pete “Whiz” Wenell for all your hard work. PeST is a four-letter word for all of us now. I would also like to thank Dr. David Jacques and Dr. Meir Pachter for their advice and help at Air Force Institute of Technology.

Gary Miller

Table of Contents

	Page
Abstract.....	v
Acknowledgements.....	vi
List of Figures.....	xi
List of Tables.....	xiii
List of Symbols.....	xiv
I. Introduction.....	1
Background.....	1
Overview.....	2
II. Model Definition.....	5
Overview.....	5
Axes Definition.....	5
Body Axes.....	6
Navigation Axes.....	7
Wind Axes.....	8
Outer-Loop Model Development.....	8
Background.....	9
Point-Mass Model Definition.....	10
Straight and Level Flight.....	12
Steady Turn Flight.....	13
Steady Rolling Flight.....	13
Learjet-25 Aeromodel.....	14
Summary.....	16
III. Inner-Loop Analysis.....	18
Overview.....	18
Inner-Loop Model Development.....	18
Navigation Axes Rotation.....	19
Wind Axes Rotation.....	20
Wind to Navigation Axes Rotation.....	21
Combined Rotations.....	21
Navigation Angle Determination.....	22

	Page
Trim Condition Definitions.....	24
Trim Condition <u>1</u>	25
Trim Condition <u>2</u>	26
Trim Condition <u>3</u>	26
Trim Condition <u>4</u>	27
Trim Condition <u>5</u>	28
Trim Condition <u>6</u>	30
Trim Condition <u>7</u>	32
Trim Condition <u>8</u>	32
Trim Condition <u>9</u>	34
Trim Condition <u>10</u>	36
Aircraft Rotation Rate Determination.....	36
Control Surface Deflection Determination.....	38
Moment Model Definition.....	39
Roll Moment Definition.....	40
Pitch Moment Definition.....	41
Yaw Moment Definition.....	41
Control Surface Deflection Equations.....	42
Summary.....	44
 IV. Aircraft Flight Trajectories.....	 45
Overview.....	45
Trim Condition Investigation.....	46
Trim Condition <u>1</u> Investigation.....	46
Altitude Effect Investigation.....	48
Weight Effect Investigation.....	50
Velocity Effect Investigation.....	52
Asymmetrical Thrust Effect Investigation.....	54
Trim Conditions <u>2</u> and <u>3</u> Investigation.....	55
Trim Condition <u>4</u> Investigation.....	57
Trim Condition <u>5</u> Investigation.....	58
Trim Condition <u>6</u> Investigation.....	60
Trim Condition <u>7</u> Investigation.....	61
Trim Condition <u>8</u> Investigation.....	62
Trim Condition <u>9</u> Investigation.....	63
Trim Condition <u>10</u> Investigation.....	66
Summary.....	67

	Page
V. Stability Derivative Sensitivity Analysis.....	68
Overview.....	68
Sensitivity Analysis.....	68
Longitudinal Stability Derivative Sensitivity.....	69
Straight and Level Flight.....	69
Climbing Flight.....	70
Lateral-Directional Stability Derivative Sensitivity.....	70
Crabbing Flight.....	71
Steady Turn Flight.....	72
Summary.....	73
VI. Flight Test Results.....	76
Overview.....	76
Aeromodel Data.....	76
Flight Test Data.....	77
Straight and Level Flight Test.....	78
Altitude Effects.....	79
Weight Effects.....	83
Velocity Effects.....	87
Longitudinal Maneuvers, Straight and Level Flight Summary.....	90
Asymmetrical Thrust Effects.....	91
Lateral-Directional Maneuvers, Straight and Level Flight Summary.....	94
Climbing and Descending Flight Test.....	95
Crabbing Flight Test.....	97
Level, Steady Turn Flight Test.....	99
Pitch-Over Flight Test.....	100
Summary.....	100
VII. Conclusions and Recommendations.....	102
Conclusions.....	102
Model Development.....	102
Trim Conditions.....	102
Model Implementation.....	103
Predicted Results.....	103
Predicted Derivative Sensitivity.....	104
Flight Test Results.....	105
Error Sources.....	105
Stability Derivative Variability.....	106
Instrumentation Errors.....	106
Non-linear Effects.....	107

	Page
Recommendations.....	107
Validate Turn Predictions.....	108
Improve Thrust Model.....	108
Include Wind Effect in Model.....	108
Investigate Transitions between Trim Conditions.....	109
Determine Stability Derivatives Accurately.....	109
Measure Weight Accurately.....	109
Automate Matlab® Routine.....	110
Appendix A: Sample Calculations.....	111
Introduction.....	111
Open-Loop Calculations.....	111
Trim Conditions <u>1</u> , <u>2</u> , <u>3</u> , and <u>4</u>	113
Trim Conditions <u>5</u> , <u>6</u> , <u>7</u> , and <u>9</u>	116
Trim Conditions <u>9</u>	119
Appendix B: Matlab® Routine.....	121
Bibliography.....	126
Vita.....	127

List of Figures

Figure	Page
1. Navigation-to-Body Axes Transformation.....	7
2. Navigation-to-Wind Axes Transformation.....	7
3. Wind-to- Body Axes Transformation.....	8
4. Force Definitions.....	10
5. Aircraft Climb Definition.....	26
6. Aircraft Crabbing Flight Definition.....	27
7. Aircraft Steady Turn Definition.....	28
8. Aircraft Climbing Turn Definition.....	30
9. Aircraft Barrel Roll Definition.....	32
10. AC-130 Gunship Maneuver Definition.....	34
11. Aircraft Pitch-over Definition.....	36
12. Three Dimensional Aircraft Moments and Forces.....	39
13. Elevator Control Surface Deflection (δ_e) and Angle of Attack (α) verses Altitude (h).....	48
14. Thrust (T) verses Altitude (h).....	49
15. Elevator Control Surface Deflection (δ_e) and Angle of Attack (α) verses Aircraft Weight (W).....	50
16. Thrust (T) verses Aircraft Weight (W).....	51
17. Elevator Control Surface Deflection (δ_e) and Angle of Attack (α) verses Aircraft Velocity (V).....	52
18. Thrust (T) verses Aircraft Velocity (V).....	53
19. Aileron Surface Deflection (δ_a) and Rudder Surface Deflection (δ_r) verses Percent of Right Engine Thrust.....	54

Figure	Page
20. Elevator Surface Deflection (δ_e), Angle of Attack (α) and Pitch Angle (θ) versus Flight Path Angle (γ).....	55
21. Thrust (T) versus Flight Path Angle (γ).....	56
22. Aileron Surface Deflection (δ_a), Rudder Surface Deflection (δ_r) and Bank Angle (ϕ) versus Sideslip Angle (β).....	58
23. Level Flight Aileron Surface Deflection (δ_a), Rudder Surface Deflection (δ_r) and Sideslip Angle (β) vs. Bank Angle (ϕ_v).....	59
24. Climbing Flight Aileron Surface Deflection (δ_a), Rudder Surface Deflection (δ_r) and Sideslip Angle (β) vs. Bank Angle (ϕ_v).....	60
25. Descending Flight Aileron Surface Deflection (δ_a), Rudder Surface Deflection (δ_r) and Sideslip Angle (β) vs. Bank Angle (ϕ_v).....	61
26. Barrel Roll Aileron Surface Deflection (δ_a), Rudder Surface Deflection (δ_r) and Sideslip Angle (β) vs. Bank Angle (ϕ_v).....	62
27. AC-130 Gunship Weapon Depression Angle (ϵ) and Load Factor (n) verses Height (h).....	64
28. AC-130 Gunship Orbit Bank Angle (ϕ_v) and Radius (r_t) versus Height (h).....	65
29. Pitch-Over Elevator Surface Deflection (δ_e) versus Pitch Rate (Q).....	66
30. Regime 1 Elevator Deflection (δ_e) vs. Altitude (h) Effect.....	79
31. Regime 2 Elevator Deflection (δ_e) vs. Altitude (h) Effect.....	80
32. Regime 1 Angle of Attack (α) and Pitch Angle (θ) vs. Altitude (h) Effect.....	81
33. Regime 2 Angle of Attack (α) and Pitch Angle (θ) vs. Altitude (h) Effect.....	82
34. Thrust (T) vs. Altitude (h) Effect.....	83
35. Elevator Deflection (δ_e) vs. Weight (W) Effect.....	84
36. Angle of Attack (α) and Pitch Angle (θ) vs. Weight (W) Effect.....	85

Figure	Page
37. Thrust (T) vs. Weight (W) Effect.....	87
38. Elevator Deflection (δ_e) vs. Velocity (V) Effect.....	88
39. Angle of Attack (α) and Pitch Angle (θ) vs. Velocity (V) Effect.....	89
40. Thrust (T) vs. Velocity (V) Effect.....	90
41. Aileron (δ_a) and Rudder (δ_r) Surface Deflection vs. Asymmetric Thrust (T) Effect.....	92
42. Sideslip (β) and Bank Angle (ϕ) vs. Asymmetric Thrust (T) Effect.....	93
43. Elevator Deflection (δ_e) vs. Flight Path Angle (γ) Effect.....	95
44. Angle of Attack (α) and Pitch Angle (θ) vs. Flight Path Angle (γ) Effect.....	96
45. Thrust (T) vs. Flight Path Angle (γ) Effect	97
46. Aileron (δ_a) and Rudder (δ_r) Surface Deflections vs. Sideslip Angle (β) Effect.....	98
47. Bank Angle (ϕ) vs. Sideslip Angle (β) Effect.....	99
48. Force Definitions.....	111

List of Tables

Table	Page
1. Learjet Aircraft Data.....	15
2. Stability Derivative Sensitivity Analysis	75

List of Symbols

Symbol	Unit
b Wing Span	ft
\bar{c} Wing Chord	ft
C_{D_o} Zero-Lift Drag Coefficient	---
C_{D_q} Drag Coefficient due to Pitch Rate	s/rad
$C_{D_{\dot{\alpha}}}$ Drag Coefficient due to Angle of Attack	rad ⁻¹
C_{l_p} Roll Moment Coefficient due to Roll Rate	s/rad
C_{l_r} Roll Moment Coefficient due to Yaw Rate	s/rad
C_{l_b} Roll Moment Coefficient due to Sideslip (Dihedral Stability)	rad ⁻¹
$C_{l_{\dot{\alpha}_a}}$ Roll Moment Coefficient due to Aileron Deflection (Roll Control Power)	rad ⁻¹
$C_{l_{\dot{\alpha}_r}}$ Roll Moment Coefficient due to Rudder Deflection	rad ⁻¹
C_{L_o} Zero-Lift Coefficient	---
C_{L_q} Lift Coefficient due to Pitch Rate	s/rad
$C_{L_{\dot{\alpha}}}$ Lift Coefficient due to Angle of Attack (Lift Curve Slope)	rad ⁻¹
$C_{L_{\dot{\alpha}_e}}$ Lift Coefficient due to Elevator Deflection	rad ⁻¹
C_{m_o} Zero-Lift Pitch Moment Coefficient	---
C_{m_q} Pitch Coefficient due to Pitch Rate	s/rad
$C_{m_{\dot{\alpha}}}$ Pitch Coefficient due to Angle of Attack	rad ⁻¹
$C_{m_{\dot{\alpha}_c}}$ Pitch Coefficient due to the change in Angle of Attack	s/rad
$C_{m_{\dot{\alpha}_e}}$ Pitch Coefficient due to Elevator Deflection	rad ⁻¹
C_{n_p} Yaw Moment Coefficient due Roll Rate	s/rad
C_{n_r} Yaw Moment Coefficient due Yaw Rate	s/rad
C_{n_b} Yaw Moment Coefficient due to Sideslip (Weathercock Stability)	rad ⁻¹
$C_{n_{\dot{\alpha}_a}}$ Yaw Moment Coefficient due to Aileron Deflection (Adverse Yaw)	rad ⁻¹
$C_{n_{\dot{\alpha}_r}}$ Yaw Moment Coefficient due to Rudder Deflection (Rudder Control Power)	rad ⁻¹
C_{y_p} Side Force Coefficient due Roll Rate	s/rad
C_{y_r} Side Force Coefficient due Yaw Rate	s/rad
C_{y_b} Side Force Coefficient due to Sideslip	rad ⁻¹
$C_{y_{\dot{\alpha}_a}}$ Side Force Coefficient due to Aileron Deflection	rad ⁻¹
$C_{y_{\dot{\alpha}_r}}$ Side Force Coefficient due to Rudder Deflection	rad ⁻¹

Symbol	Unit	
cg	Center of Gravity (percent \bar{c})	---
deg/°	Degrees	deg
ft	Feet	ft
F _y	Side Force	lbs
g	Gravity (Number times Earth's gravity – 32.174 ft/s ²)	---
h	Altitude	ft
H	Course Angle (Navigation Axes)	deg
\dot{H}	Rate of Change in Course Angle	deg/s
I _{xx}	Mass Moment of Inertia (x _b -axis)	$\frac{\text{slug}}{\text{ft}^2}$
I _{xz}	Product of Inertia (x _b - and z _b -axes)	$\frac{\text{slug}}{\text{ft}^2}$
I _{yy}	Mass Moment of Inertia (y _b -axis)	$\frac{\text{slug}}{\text{ft}^2}$
I _{zz}	Mass Moment of Inertia (z _b -axis)	$\frac{\text{slug}}{\text{ft}^2}$
KIAS	Knots Indicated Airspeed	knots
lbs	Pounds	lbs
L	Lift	lbs
\bar{L}	Roll Moment	ft-lbs
\bar{L}_P	Roll Moment due to Roll Rate	ft-lbs
\bar{L}_R	Roll Moment due to Yaw Rate	ft-lbs
\bar{L}_T	Roll Moment due to Thrust	ft-lbs
\bar{L}_b	Roll Moment due to Sideslip	ft-lbs
\bar{L}_{d_a}	Roll Moment due to Aileron Deflection	ft-lbs
\bar{L}_{d_r}	Roll Moment due to Rudder Deflection	ft-lbs
M	Pitch Moment	ft-lbs
M _o	Zero-Lift Pitch Moment	ft-lbs
M _Q	Pitch Moment due to Pitch Rate	ft-lbs
M _T	Pitch Moment due to Thrust	ft-lbs
M _á	Pitch Moment due to Angle of Attack	ft-lbs
M _{á̇}	Pitch Moment due to the Change in Angle of Attack	ft-lbs
M _{d_e}	Pitch Moment due to Elevator Deflection	ft-lbs
MSL	Mean Sea Level	ft
n	Load Factor	---
N	Yaw Moment	ft-lbs
N _P	Yaw Moment due to Roll Rate	ft-lbs
N _R	Yaw Moment due to Yaw Rate	ft-lbs

Symbol		Unit
N_T	Yaw Moment due to Thrust	ft-lbs
N_b	Yaw Moment due to Sideslip	ft-lbs
N_{d_a}	Yaw Moment due to Aileron Deflection	ft-lbs
N_{d_r}	Yaw Moment due to Rudder Deflection	ft-lbs
NED	North-East-Down (Navigation Axes)	---
P	Roll Rate	rad/s
psi	Pounds per Square Inch	psi
q	Dynamic Pressure	$\frac{\text{lbs}}{\text{ft}^2}$
Q	Pitch Rate	rad/s
r_b	Barrel Roll Radius	ft
r_t	Steady Turn Radius	ft
r_θ	Pitch-Over Radius	ft
rad	Radians	rad
R	Yaw Rate	rad/s
\bar{R}	Universal Gas Constant ($1718 \frac{\text{ft} \cdot \text{lbs}}{\text{slug} \cdot ^\circ\text{R}}$)	---
$^\circ\text{R}$	Degrees Rankine	deg
s	Seconds	s
S_t	Horizontal Tail Surface Area	ft ²
S_w	Wing Surface Area	ft ²
t	Time	s
T	Thrust	lbs
T_o	Standard Sea Level Temperature	$^\circ\text{R}$
T_1	Thrust from Right Engine	lbs
T_2	Thrust from Left Engine	lbs
TPS	Test Pilot School	---
UAV	Unmanned Aerial Vehicle	---
V	Velocity	ft/s
W	Aircraft Weight	lbs
x_b	X-Body Axis	---
x_n	X-Navigation Axis	---
x_T	Distance from Center of Gravity to Center of Thrust along x_b -axis	ft
x_w	X-Wind Axis	---
x_1	Intermediate X-Axis (Navigation to Body Axes Rotation)	---
x_2	Intermediate X-Axis (Navigation to Body Axes Rotation)	---
x_3	Intermediate X-Axis (Navigation to Wind Axes Rotation)	---
x_4	Intermediate X-Axis (Navigation to Wind Axes Rotation)	---
x_5	Intermediate X-Axis (Wind to Body Axes Rotation)	---
y_b	Y-Body Axis	---
y_n	Y-Navigation Axis	---

Symbol		Unit
y_T	Distance from Center of Gravity to Center of Thrust along y_b -axis	ft
y_w	Y-Wind Axis	---
y_1	Intermediate Y-Axis (Navigation to Body Axes Rotation)	---
y_2	Intermediate Y-Axis (Navigation to Body Axes Rotation)	---
y_3	Intermediate Y-Axis (Navigation to Wind Axes Rotation)	---
y_4	Intermediate Y-Axis (Navigation to Wind Axes Rotation)	---
y_5	Intermediate Y-Axis (Wind to Body Axes Rotation)	---
z_b	Z-Body Axis	---
z_n	Z-Navigation Axis	---
z_T	Distance from Center of Gravity to Center of Thrust along z_b -axis	ft
z_w	Z-Wind Axis	---
z_1	Intermediate Z-Axis (Navigation to Body Axes Rotation)	---
z_2	Intermediate Z-Axis (Navigation to Body Axes Rotation)	---
z_3	Intermediate Z-Axis (Navigation to Wind Axes Rotation)	---
z_4	Intermediate Z-Axis (Navigation to Wind Axes Rotation)	---
z_5	Intermediate Z-Axis (Wind to Body Axes Rotation)	---
α	Angle of Attack	deg
α_T	Angle of Thrust from x_b -axis	deg
β	Angle of Sideslip	deg
γ	Flight Path Angle	deg
δ	Control Surface Deflection Angle	deg
δ_a	Aileron Deflection Angle	deg
$d_{a_{max}}$	Learjet-25 Maximum Aileron Deflection Angle	rad
$d_{a_{min}}$	Learjet-25 Minimum Aileron Deflection Angle	rad
δ_e	Elevator Deflection Angle	deg
$d_{e_{max}}$	Learjet-25 Maximum Elevator Deflection Angle	rad
$d_{e_{min}}$	Learjet-25 Minimum Elevator Deflection Angle	rad
δ_r	Rudder Deflection Angle	deg
$d_{r_{max}}$	Learjet-25 Maximum Rudder Deflection Angle	rad
$d_{r_{min}}$	Learjet-25 Minimum Rudder Deflection Angle	rad
ϵ	Weapon Depression Angle	deg
ϕ	Bank Angle (Body Axes)	deg
ϕ_v	Velocity Bank Angle (Navigation Axes)	deg
ρ_o	Standard Sea Level Air Density	$\frac{\text{slug}}{\text{ft}^3}$
θ	Pitch Angle (Body Axes)	deg
ω_ϕ	Aircraft Roll Rate (about x_b -axis)	rad/s
ω_θ	Aircraft Pitch Rate (about y_b -axis)	rad/s
ω_ψ	Aircraft Turn Rate (about z_b -axis)	rad/s
ψ	Yaw Angle (Body Axes)	deg

OUTER-LOOP CONTROL IN ASYMMETRICAL TRIMMED FLIGHT CONDITIONS

I. Introduction

Background

Automatic flight control systems are a vital part of most aircraft designs. The autopilot controls both the longitudinal and lateral-directional motion of the vehicle to perform the desired mission. The control system decreases pilot workload, enhances flight safety, and increasingly is used to stabilize aircraft that otherwise would not be stable. Also, with the increased use of Unmanned Aerial Vehicles (UAVs), the automatic flight control system is vital to achieve the required performance. Traditionally, automatic flight control systems have used linearized equations of motion to simplify aircraft motion around an equilibrium point. Linearization methods have been studied extensively and are implemented on most modern aircraft (1: Chapter 5). It is proposed to solve the aircraft equations of motions to find the necessary control surface deflections to achieve a desired flight path and orientation. The developed equations are applicable to most of the flight envelope and not fixed to the equilibrium point.

From the time of the Wright brothers, aircraft stability and control has been a central concern of aircraft design. To meet design performance requirements, a balance must be achieved between aircraft stability and maneuverability. Increasingly, modern

aircraft are designed to be inherently unstable to meet increased operational demands.

The F-16 fighter aircraft is unstable in the unaugmented airframe configuration, and requires an automatic flight control system to maintain steady flight (2: Class 2).

Automatic flight control systems have been studied extensively, and many schemes have been designed (3: 367, 386).

The traditional design method for flight control systems is to assume flight at a stable equilibrium point with small perturbations from that point. The aircraft equations of motion are linearized, and small angle assumptions are normally made to simplify the equations. This method is generally only valid for a small region and must be recalculated if flight conditions change from the equilibrium point. This requires the automatic flight control system to be divided into small regions of applicability (gain scheduling). Changing from one gain region to another may cause discontinuities in the equilibrium point and jumps in the commanded control inputs. Therefore, it is desirable to design an automatic flight control system that is applicable for most of the flight envelope.

Overview

A design is envisioned to solve the required control surface deflection angles from the aircraft equations of motion for a desired flight condition. A design was proposed utilizing a nested loop controller to solve the equations of motion (reference 4). The outer-loop dynamics of the aircraft were modeled as a point mass, using nonlinear equations of motion. The flight state variables (velocity (V), glide path angle (γ) and course angle (H) change rate) were nondimensionalized and used to describe the desired trimmed steady state flight trajectory. The flight trajectory is defined as the path the

aircraft center of gravity travels through the atmosphere. Additionally, to solve the equations either sideslip angle (β) or bank angle (ϕ_v) must be specified for the given flight condition. Equations were developed to output angle of attack (α), thrust setting (T), sideslip angle, and bank angle from the state variable inputs.

The remainder of the design was developed and implemented for verification on an actual aircraft. The outer-loop outputs were dimensionalized for the aircraft model data. The results of the outer-loop equations were in the wind axis, which were then transformed to the body axis to become the inputs into the inner-loop equations. The inner-loop equations use the calculated α , T, β , ϕ_v and specified flight orientation to find the required aileron (δ_a), elevator (δ_e), and rudder (δ_r) surface deflection angles. The flight orientation is defined as the aircraft rotation and angular acceleration about the center of gravity. As long as the required deflections are smaller than the deflection limits, the desired trimmed flight path can be achieved by commanding the control surfaces. The control laws were implemented using a Learjet-25 model to determine the validity of the approach. Finally, the trim condition parameters were established in flight tests to verify the predicted results.

The remainder of the paper is in the following format. In Chapter 2, the three axes used for the equations of motions (wind axis, navigation axis, and body axis) are introduced. The Learjet-25 aircraft model is also presented and all model parameters are listed in Table 1. Next, the equations previously derived to calculate the outer-loop are reviewed and modified to match the defined axes. The aircraft trim equations for the inner-loop dynamics are derived in Chapter 3. In Chapter 4, selected flight trajectories are investigated for trimmed equilibrium flight conditions. First, straight and level flight

is explored. A wings level climb and wings level descent are then calculated. Next, crabbing flight (sideslip angle not equal to zero) is determined. Steady, level turn and corkscrew turn (climbing and descending) maneuvers are then investigated. Next, a barrel roll maneuver (constantly changing roll angle) is reproduced. Then the AC-130 gunship level orbit, firing maneuver is examined. Finally, a steady pitch-over maneuver is modeled. In Chapter 5, the effect of errors in the stability derivatives are investigated by varying the known derivative values $\pm 40\%$ to determine the change in the control surface predictions. Control surface deflection changes greater than 1.0 degree are considered to have a significant impact on the equation predictions. In Chapter 6 the predictions from Chapter 4 were validated by flight test data. Selected trim conditions were examined in the flight test program and compared to the theoretically calculated values. Chapter 7 includes the conclusions and recommendations.

II. Model Definition

Overview

In Chapter 2, the point mass model is developed to provide a basis for the control laws for the trajectory of the aircraft. The outer-loop equations are found from the nonlinear equations of motion and applied to the actual Learjet-25 parameters. The outer-loop model equations are reviewed to provide a basis for the rest of the study. The equations were previously developed (reference 4), but are reviewed for clarity due to the need to redefine the reference axes. The control equations are developed from balancing the forces and moments (trimmed flight). In Chapter 3, the outer-loop equation outputs are used with the transformation matrices and the remainder of the equations of motion to find the control surface deflections required to achieve the desired flight trajectory and orientation. In Chapter 4, the equations developed in the previous two chapters are used to simulate selected flight trajectories. By choosing the correct input states, the required control surface deflections for the desired flight path are found. The impacts of variations in the stability derivatives are investigated in Chapter 5 to determine which parameters require the most accuracy. Finally, in Chapter 6 the theoretical values tested using the Learjet-25 in flight tests are compared to the theoretical calculations.

Axes Definition

Background information and the aircraft model are now presented. First, the pertinent reference frames are introduced, including the coordinate transformations. The

outer-loop equations are re-derived including the necessary changes for the redefined axes. Finally, the Learjet-25 aerodynamic parameters are provided.

Three reference frames are used in the development of the control equations: body axes, wind axes and the navigation frame. The body axes are affixed to and move with the aircraft. The body axes parameters are easiest to measure since they remain constant with respect to the aircraft. The wind axes are fixed to the aircraft center of gravity (cg) and utilize the free-stream airflow as a reference. Wind axes reference frames are used extensively in analyzing flight mechanics. The navigation frame is attached to the earth and provides an approximate inertial reference frame. The axes definition and relationships between reference frames follow.

Body Axes.

The body axes frame is specified in relation to the structure of the aircraft. The body x-axis (x_b) points out of the nose of the aircraft. The body y-axis (y_b) is orthogonal to the x_b -axis, passing out the right wing, and the body z-axis (z_b) completes the right-handed coordinate system, pointing in a downward direction. The body axes system is defined relative to the North-East-Down (NED) navigation axes frame by specifying the 3-2-1 Euler angles: First, the heading angle (ψ) is the rotation about the navigation z-axis (z_n) to establish the intermediate 1-axes. Next, the pitch angle (θ) is the rotation about the y_1 -axis to find the intermediate 2-axes. Finally, the roll angle (ϕ) is the rotation about the x_2 -axis to produce the body axes. The rotations and angles are shown in Figure 1. The inner-loop calculations are performed in the navigation axes frame.

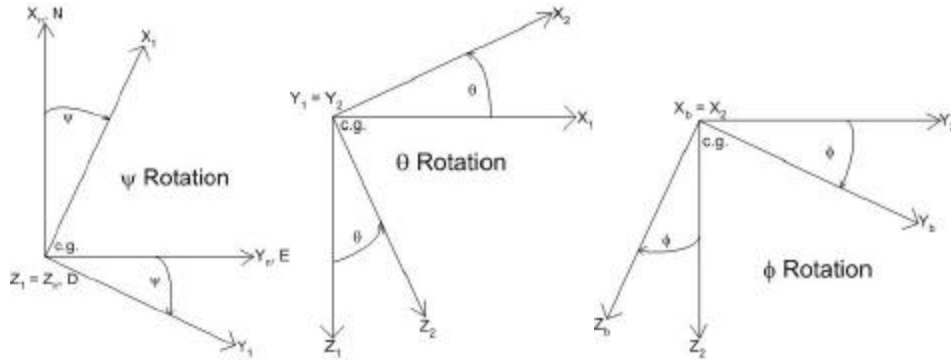


Figure 1. Navigation-to-Body Axes Transformation

Navigation Axes.

The navigation axes provide an approximate inertial reference frame and are used for most performance calculations. In flight mechanics though, the wind axes frame is typically used. The navigation axes are also related to the wind axes by a set of 3-2-1 Euler angles. First, the course angle (H) is defined as the rotation about the z_n -axis to find the intermediate 3-axes. Next, the flight path angle (γ) is defined as the rotation about the y_3 -axes to find the intermediate 4-axes. Finally, ϕ_v is defined as the rotation about the x_4 -axis to produce the wind axes. The Euler angles H , γ , and ϕ_v are shown in Figure 2.

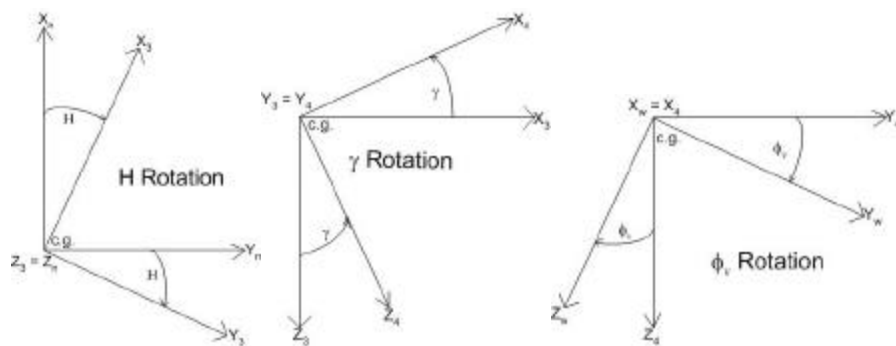


Figure 2. Navigation-to-Wind Axes Transformation

Wind Axes.

The outer-loop control model equations use the wind-axes system. The wind axes are defined as the x_w -axis pointing along the forward velocity vector of the free-stream airflow. The z_w -axis is defined negative along the aircraft lift vector, perpendicular to the x_w -axis. The y_w -axis is orthogonal to both the x_w - and z_w -axis, pointing to the right. The relationship between the wind axes and the body axes is found by first rotating the aircraft about the z_w -axis by the sideslip angle to find the intermediate y_s -axes. The wind axes are then defined as the rotation of the angle of attack about the new y_s -axis. The rotations and angles are shown in Figure 3.

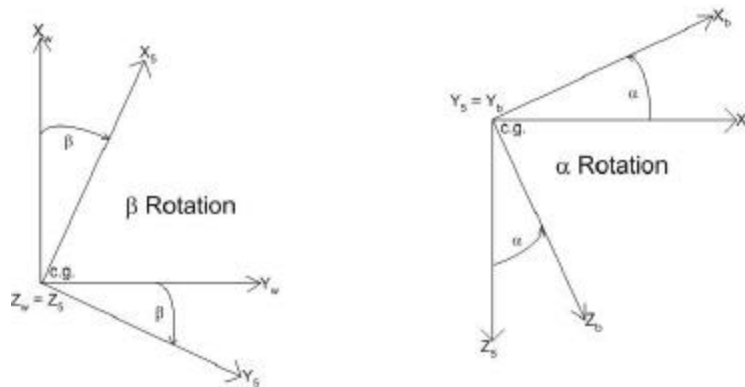


Figure 3. Wind-to- Body Axes Transformation

Outer-Loop Model Development

This is the definition of the aerodynamic angles used in this paper. Unfortunately, there is no standard definition of the aerodynamic angles, α and β (1:62), (5:36 and 88). Sideslip angle, β , is normally assumed to be small, so this is not normally a significant

issue. For large angles the correct definition of α and β is important and a rotation order must be specified. Sideslip is chosen as the first rotation angle because in a wind-tunnel, the model would normally be first rotated by β , and then α for each test condition. When the aerodynamic angles are small, roll angle, ϕ_v , is approximately equal to ϕ . The pitch angle, θ , is approximately equal to the sum of the angles α and γ . The yaw angle, ψ , is approximately equal to the combined angle of H and β . The previous outer-loop study (reference 4) had different definitions for the axes, but with the above definitions of the axes, existing aircraft performance data could be used without modifications. The previous aircraft equations of motion were altered to reflect the new axes definitions.

Background.

The outer-loop equations were previously derived for a generic fighter aircraft. The derivation of the equations of motion is reviewed with the new definition of the coordinate axes. Even though the y_b - and z_b - axes were rotated 180 degrees, the only difference in the equations is the definition of the flight path angle, γ , which is now negative with the new definitions. The side-force (F_y) has the same sign, but now is defined as positive to the right. The forces acting on the aircraft are shown on Figure 4.

Point-Mass Model Definition.

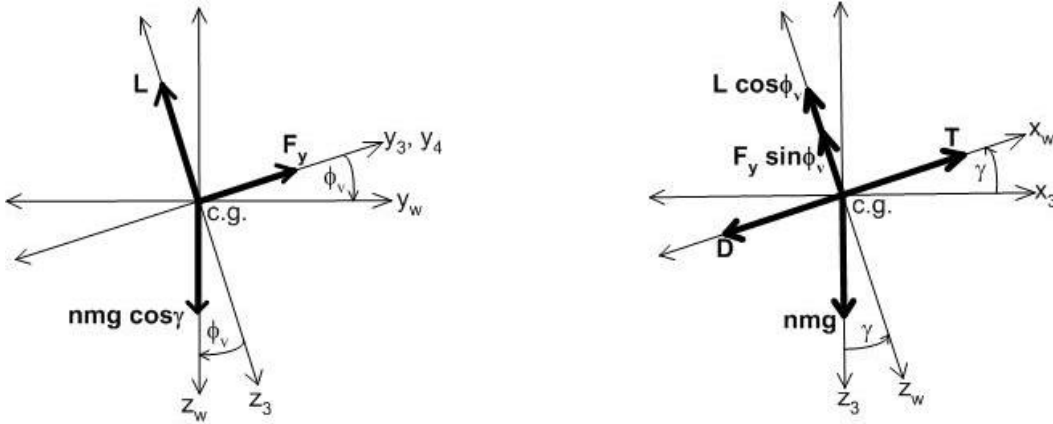


Figure 4. Force Definitions

The aerodynamic forces are

$$L = \bar{q} \frac{V^2}{V_o^2} C_{L\dot{\alpha}} (\alpha + \dot{\alpha}_{o_L}) \quad (1)$$

where $\bar{q} = \frac{1}{2} \bar{\rho} V_o^2 S_w$ (dynamic pressure)

$$D = \bar{q} \frac{V^2}{V_o^2} (C_{D\dot{\alpha}} \alpha + C_{D_o}) \quad (2)$$

$$F_y = \bar{q} \frac{V^2}{V_o^2} \frac{S_t}{S_w} C_{y\dot{\alpha}} \beta \quad (3)$$

$$T = mg\mu \text{ (thrust)} \quad (4)$$

The non-dimensionalized thrust setting is μ .

The aircraft equations of motion using wind axes are

$$\dot{V} = \frac{T - D}{m} - ng \sin \tilde{\alpha} \quad (5)$$

$$\dot{\tilde{\alpha}} = \frac{L \cos \mathbf{f}_v + F_y \sin \mathbf{f}_v}{mV} - \frac{ng}{V} \cos \tilde{\alpha} \quad (6)$$

$$\dot{H} = \frac{-L \sin \mathbf{f}_v + F_y \cos \mathbf{f}_v}{mV \cos \tilde{\alpha}} \quad (7)$$

The same assumptions and simplifications of the previous study (reference 4) to the equations were applied to find the control variables μ , α , β , and ϕ_v as functions of the state variables (V , γ and H). Details of the calculations are found in Appendix A. With the equations of motion derived, specific trim conditions are then examined. By describing the trimmed flight condition with respect to the state variables, control settings were obtained for the trim conditions.

The stability derivative $C_{D\dot{\alpha}}$ was used for the Learjet-25 model. Often the drag is defined as a function of $(C_{L\dot{\alpha}}^2 \alpha^2 + C_{D_0})$, but the available model used $C_{D\dot{\alpha}}$. The model will not be as accurate as the trim condition gets farther from flight condition where $C_{D\dot{\alpha}}$ was determined since $C_{D\dot{\alpha}}$ does not account for the second-order effects of $C_{L\dot{\alpha}}^2$. Using $C_{L\dot{\alpha}}^2$ may increase the accuracy away from the point where the stability derivatives were calculated.

Straight and Level Flight.

For trimmed flight, the derivatives of the state variables (\dot{V} , $\dot{\alpha}$, and \dot{H}) are set equal to zero. Details of the calculations are found in Appendix A. Again, one of the control variables β or ϕ_v must be chosen for the specified trim condition.

The trim control law for a specified trim β is

$$\sin\phi_v = \frac{C_{y_a} S_t \bar{q}}{V_o^2 n m g S_w} \frac{V^2 \hat{a}}{\cos \tilde{a}} \quad (8)$$

$$\cos\phi_v = \sqrt{1 - \left(\frac{C_{y_a} S_t \bar{q} V^2 \hat{a}}{V_o^2 n m g S_w \cos \tilde{a}} \right)^2} \quad (9)$$

$$\alpha = \frac{1}{C_{L_d}} \left(\sqrt{\left(\frac{V_o^2 n m g \cos \tilde{a}}{\bar{q} V^2} \right)^2 - \left(\frac{C_{y_a} S_t \hat{a}}{S_w} \right)^2} \right) - \hat{a}_{o_L} \quad (10)$$

$$\mu = \frac{\bar{q} V^2}{m g V_o^2} (C_{D_o} - C_{D_d} \hat{a}_{o_L}) + \sqrt{\left(\frac{C_{D_d} n \cos \tilde{a}}{C_{L_d}} \right)^2 - \left(\frac{C_{D_d} C_{y_a} S_t \bar{q} V^2 \hat{a}}{C_{L_d} V_o^2 n m g S_w} \right)^2} + n \sin \tilde{a} \quad (11)$$

and the trim control law for a specified trim ϕ_v is

$$\beta = \frac{V_o^2 n m g S_w \cos \tilde{a}}{C_{y_a} S_t \bar{q}} \frac{\cos \tilde{a}}{V^2} \sin f_v \quad (12)$$

$$\mathbf{a} = \frac{1}{C_{L_a}} \left(\frac{V_o^2 n m g \cos \tilde{a}}{\bar{q} V^2} \cos f_v \right) - \mathbf{a}_{o_L} \quad (13)$$

$$\mathbf{m} = \frac{C_{D_a}}{C_{L_a}} (n \cos \tilde{a} \cos f_v) + \frac{\bar{q} V^2}{m g V_o^2} (C_{D_o} - C_{D_a} \mathbf{a}_{o_L}) + n \sin \tilde{a} \quad (14)$$

Steady Turn Flight.

For steady turning flight, $\dot{\psi}$ and $\dot{\alpha}$ are set equal to zero, but $\dot{\chi}$ is a constant specified course change rate, \mathbf{v}_ψ . Therefore, $H(t)$ is equal to $\mathbf{v}_\psi t$. For a specified trim β , the control law is

$$\cos \mathbf{f}_v = \frac{\bar{q}V^2}{mV_o^2 \cos \tilde{\alpha} [(ng)^2 + (V\mathbf{v}_\psi)^2]} \left[ng \sqrt{\left(\frac{V_o^2}{\bar{q}V^2} m \cos \tilde{\alpha} \right)^2 [(ng)^2 + (V\mathbf{v}_\psi)^2]} - \left(\frac{S_t}{S_w} C_{y_b} \mathbf{b} \right)^2 + V\mathbf{v}_\psi \frac{S_t}{S_w} C_{y_b} \mathbf{b} \right] \quad (15)$$

$$\sin \mathbf{f}_v = \frac{\bar{q}V^2}{mV_o^2 \cos \tilde{\alpha} [(ng)^2 + (V\mathbf{v}_\psi)^2]} \left[-V\mathbf{v}_\psi \sqrt{\left(\frac{V_o^2}{\bar{q}V^2} m \cos \tilde{\alpha} \right)^2 [(ng)^2 + (V\mathbf{v}_\psi)^2]} - \left(\frac{S_t}{S_w} C_{y_b} \mathbf{b} \right)^2 + ng \frac{S_t}{S_w} C_{y_b} \mathbf{b} \right] \quad (16)$$

$$\mathbf{a} = \frac{1}{C_{L_a}} \sqrt{\left(\frac{V_o^2}{\bar{q}V^2} m \cos \tilde{\alpha} \right)^2 [(ng)^2 + (V\mathbf{v}_\psi)^2]} - \left(\frac{S_t}{S_w} C_{y_b} \mathbf{b} \right)^2 - \mathbf{a}_{o_L} \quad (17)$$

$$\mathbf{m} = \frac{\bar{q}V^2}{mgV_o^2} \left(\frac{C_{D_a}}{C_{L_a}} \sqrt{\left(\frac{V_o^2}{\bar{q}V^2} m \cos \tilde{\alpha} \right)^2 [(ng)^2 + (V\mathbf{v}_\psi)^2]} - \left(\frac{S_t}{S_w} C_{y_b} \mathbf{b} \right)^2 - C_{D_a} \mathbf{a}_{o_L} + C_{D_o} \right) + ng \sin \tilde{\alpha} \quad (18)$$

Steady Rolling Flight.

For steady rolling flight, $\dot{\psi}$, $\dot{\chi}$ and $\dot{\alpha}$ are set equal to zero, but the velocity vector roll rate $\dot{\phi}$ is a constant specified rate, \mathbf{v}_f . Therefore, $\phi_v(t)$ is equal to $\mathbf{v}_f t$. Again, for a specified \mathbf{v}_f , the trim control law is

From equation (12)

$$\beta(t) = \frac{V_o^2 n m g S_w \cos \tilde{\alpha}}{C_{y_{\tilde{\alpha}}} S_t \bar{q}} \frac{\cos \tilde{\alpha}}{V^2} \sin \bar{\omega}_f t \quad (19)$$

From equation (13)

$$\alpha(t) = \frac{1}{C_{L_{\tilde{\alpha}}}} \left(\frac{V_o^2 n m g \cos \tilde{\alpha} \cos \bar{\omega}_f t}{\bar{q} V^2} \right) - \dot{\alpha}_{o_L} \quad (20)$$

From equation (14)

$$\mu(t) = \frac{\bar{q} V_o^2}{m g V_o^2} (C_{D_o} - C_{D_{\tilde{\alpha}}} \dot{\alpha}_{o_L}) + \frac{C_{D_{\tilde{\alpha}}}}{C_{L_{\tilde{\alpha}}}} n \cos \tilde{\alpha} \cos \bar{\omega}_f t + n \sin \tilde{\alpha} \quad (21)$$

Learjet-25 Aeromodel.

The aircraft model used is the Learjet-25 aircraft operated by Veridian for United States Air Force Test Pilot School (TPS). The aircraft data is listed in Table 1 (reference 7).

Table 1. Learjet Aircraft Data

<u>AIRCRAFT PARAMETER</u>	<u>VARIABLE</u>	<u>VALUE</u>	<u>UNITS</u>
Weight (Standard Fuel Load)	W	13,500	lbs
Wing Area	S_w	231.8	ft ²
Wing Span	b	39.5	ft
Mean Aerodynamic Chord	\bar{c}	9	ft
Vertical Tail Area	S_t	76.5	ft ²
Aircraft Lift-Curve Slope	$C_{L_{\dot{\alpha}}}$	4.967	rad ⁻¹
Aircraft Zero-Lift Coefficient	C_{L_o}	0.0105	-----
Lift Coefficient due to Elevator	$C_{L_{\dot{\alpha}_e}}$	0.3631	rad ⁻¹
Lift Coefficient due to Pitch Rate	C_{L_q}	37.357	s/rad
Aircraft Drag Coefficient due to Lift	$C_{D_{\dot{\alpha}}}$	0.1146	rad ⁻¹
Aircraft Zero-Lift Drag Coefficient	C_{D_o}	0.0235	-----
Drag Coefficient due to Pitch Rate	C_{D_q}	4.927	s/rad
Mass Moment of Inertia (x_b -axis)	I_{xx}	20,000	slug ft ²
Mass Moment of Inertia (y_b -axis)	I_{yy}	22,900	slug ft ²
Mass Moment of Inertia (z_b -axis)	I_{zz}	40,000	slug ft ²
Product of Inertia (x_b - and z_b -axes)	I_{xz}	1,980	slug ft ²
Side-Force Coefficient due to Sideslip	$C_{y_{\dot{\alpha}}}$	-0.7620	rad ⁻¹
Side-Force Coefficient due to Rudder	$C_{y_{\dot{\alpha}_r}}$	0.1423	rad ⁻¹
Side-Force Coefficient due to Aileron	$C_{y_{\dot{\alpha}_a}}$	-0.0613	rad ⁻¹
Side-Force Coeff. due to Roll Rate	C_{y_p}	8.549	s/rad
Side-Force Coeff. due to Yaw Rate	C_{y_r}	47.423	s/rad
Roll Moment Coeff. due to Sideslip	$C_{l_{\dot{\alpha}}}$	-0.0945	rad ⁻¹
Roll Moment Coeff. due to Rudder	$C_{l_{\dot{\alpha}_r}}$	0.0198	rad ⁻¹
Roll Moment Coeff. due to Aileron	$C_{l_{\dot{\alpha}_a}}$	-0.0791	rad ⁻¹
Roll Moment Coeff. due to Roll Rate	C_{l_p}	-25.573	s/rad
Roll Moment Coeff. due to Yaw Rate	C_{l_r}	22.221	s/rad
Yaw Moment Coeff. due to Sideslip	$C_{n_{\dot{\alpha}}}$	0.0830	rad ⁻¹
Yaw Moment Coeff. due to Aileron	$C_{n_{\dot{\alpha}_a}}$	-0.0011	rad ⁻¹
Yaw Moment Coeff. due to Rudder	$C_{n_{\dot{\alpha}_r}}$	-0.0516	rad ⁻¹
Yaw Moment Coeff. due to Roll Rate	C_{n_p}	-3.676	s/rad
Yaw Moment Coeff. due to Yaw Rate	C_{n_r}	-6.666	s/rad

(cont.)

Table 1. (cont.)

AIRCRAFT PARAMETER	VARIABLE	VALUE	UNITS
Pitch Coeff. due to Angle of Attack	$C_{m_{\dot{\alpha}}}$	-0.8921	rad^{-1}
Pitch Coefficient due Alpha Change	$C_{m_{\dot{\alpha}\zeta}}$	-5.615	s/rad
Zero-Lift Pitch Coefficient	C_{m_0}	0.0529	-----
Pitch Coefficient due to Pitch Rate	$C_{m_{\dot{q}}}$	-864.347	rad^{-1}
Pitch Coefficient due to Elevator	$C_{m_{\dot{\delta}_e}}$	-0.8434	rad^{-1}
Maximum Thrust Right Engine	$T_{1\text{max}}$	5000	lbs
Maximum Thrust Left Engine	$T_{2\text{max}}$	5000	lbs
X-direction Distance c.g. to Thrust	x_T	0.1	ft
Y-direction Distance c.g. to Thrust	y_T	3	ft
Z-direction Distance c.g. to Thrust	z_T	0.1	ft
Engine Thrust Angle	$\dot{\alpha}_T$	0.0	rad
Maximum Elevator Deflection Angle	$\ddot{\alpha}_{e\text{max}}$	0.2618	rad
Minimum Elevator Deflection Angle	$\ddot{\alpha}_{e\text{min}}$	-0.2618	rad
Maximum Aileron Deflection Angle	$\ddot{\alpha}_{a\text{max}}$	0.5236	rad
Minimum Aileron Deflection Angle	$\ddot{\alpha}_{a\text{min}}$	-0.5236	rad
Maximum Rudder Deflection Angle	$\ddot{\alpha}_{r\text{max}}$	0.6109	rad
Minimum Rudder Deflection Angle	$\ddot{\alpha}_{r\text{min}}$	-0.6109	rad
Sea-level Air Density	ρ_0	2.3769×10^{-3}	slug/ft^3
Universal Gas Constant	\bar{R}	1718	$\text{ft lbs/slug}^\circ \text{R}$
Sea-level Temperature	T_0	518.69	$^\circ \text{R}$
Gravitational Acceleration	g	32.174	ft/sec^2

Summary

In this chapter the aircraft model was first described. New axes definitions were presented and the relationships between body, wind and navigation axes were detailed. The outer-loop equations of motion were then redefined, to produce new control laws. With the new control laws, state variable values were chosen to describe a desired flight trajectory, and the resulting control settings were determined. Therefore, the outer loop model uses the state variables (V , γ , and H) and a specified value for either β or ϕ_v , and

outputs the necessary control variables (α , β , ϕ_v , and μ). The inner-loop equations use the aircraft state values and the above control settings to determine the aircraft control surface deflections (δ_a , δ_e , and δ_r) in the next chapter. Finally, the Learjet aircraft parameters necessary to calculate the inner- and outer-loops were provided.

III. Inner-Loop Analysis

Overview

In Chapter 2, the point mass model was developed to provide a basis for the control laws for the trajectory of the aircraft. The outer-loop equations were found from the nonlinear equations of motion and applied to the actual Learjet-25 parameters. In Chapter 3, the outer-loop equation outputs are used with the transformation matrices and the remainder of the equations of motion to find the control surface deflections required to achieve the desired flight trajectory and orientation. With the outer-loop equations developed in the last chapter, the inner-loop equations are established to provide aircraft control laws for the Learjet-25. Selected trim conditions are then examined to determine the equations to predict the required control surface deflections. In Chapter 4, the equations developed in the previous two chapters are used to simulate selected flight trajectories. By choosing the correct input states, the required control surface deflections for the desired flight path are found. The impacts of variations in the stability derivatives are investigated in Chapter 5 to determine which parameters require the most accuracy. Finally, in Chapter 6 the theoretical values tested using the Learjet-25 in flight tests are compared to the theoretical calculations.

Inner-Loop Model Development

The inner-loop model uses the trim state variables and the trim control variables from Chapter 2 to determine the needed trimmed aircraft control surface deflections. First, the navigation axes Euler angles are calculated from the known wind axes using the

relevant transformation matrix. With the Euler angles and the specified angular rotations for the desired flight trajectory and orientation, the aircraft's angular rates resolved in the body axes are determined. Next, with the six-degree-of-freedom aircraft equations of motion, a steady-state trim condition was chosen to find the required control surface deflections from the known aircraft parameters. Finally, assumptions were made for the aircraft to simplify the control surface deflection equations for the specific trim conditions.

The body, wind and navigation axes were defined in Chapter 2, with the required rotation angles to translate between coordinate systems. The angles (α , β , ϕ_v , γ , and H) are used in the outer-loop. The inner-loop equations use the Euler angles (ψ , θ , and ϕ). The relevant axes conversion matrix is used to determine the Euler angles.

Navigation Axes Rotation.

First, the navigation-to-body axes conversion matrix was determined using Figure

1. The following three rotations define the axes rotations

$$C_{\Psi} = \begin{bmatrix} \cos \Psi & -\sin \Psi & 0 \\ \sin \Psi & \cos \Psi & 0 \\ 0 & 0 & 1 \end{bmatrix}$$

$$C_{\theta} = \begin{bmatrix} \cos \theta & 0 & \sin \theta \\ 0 & 1 & 0 \\ -\sin \theta & 0 & \cos \theta \end{bmatrix}$$

$$C_{\phi} = \begin{bmatrix} 1 & 0 & 0 \\ 0 & \cos \phi & -\sin \phi \\ 0 & \sin \phi & \cos \phi \end{bmatrix}$$

The coordinate transformation matrix is given by

$$C_b^n = C_\emptyset \cdot C_\psi \cdot C_f$$

$$C_b^n = \begin{bmatrix} \cos \psi \cos \Psi & \sin f \sin \psi \cos \Psi - \cos f \sin \Psi & \cos f \sin \psi \cos \Psi + \sin f \sin \Psi \\ \cos \psi \sin \Psi & \sin f \sin \psi \sin \Psi + \cos f \cos \Psi & \cos f \sin \psi \sin \Psi - \sin f \cos \Psi \\ -\sin \psi & \sin f \cos \psi & \cos f \cos \psi \end{bmatrix} \quad (18)$$

Wind Axes Rotation.

The wind-to-body axes rotations are shown in Figure 2. The following two transformations define the axes rotations

$$C_a = \begin{bmatrix} \cos \hat{\alpha} & -\sin \hat{\alpha} & 0 \\ \sin \hat{\alpha} & \cos \hat{\alpha} & 0 \\ 0 & 0 & 1 \end{bmatrix}$$

$$C_{\hat{\alpha}} = \begin{bmatrix} \cos \acute{\alpha} & 0 & \sin \acute{\alpha} \\ 0 & 1 & 0 \\ -\sin \acute{\alpha} & 0 & \cos \acute{\alpha} \end{bmatrix}$$

where the transformation matrix is

$$C_b^w = C_{\hat{\alpha}} \cdot C_a = \begin{bmatrix} \cos \acute{\alpha} \cos \hat{\alpha} & -\sin \hat{\alpha} & \sin \acute{\alpha} \cos \hat{\alpha} \\ \cos \acute{\alpha} \sin \hat{\alpha} & \cos \hat{\alpha} & \sin \acute{\alpha} \sin \hat{\alpha} \\ -\sin \acute{\alpha} & 0 & \cos \acute{\alpha} \end{bmatrix} \quad (19)$$

Wind to Navigation Axes Rotation.

The wind-to-navigation axes rotations are shown in Figure 3. The following three transformations define the axes rotation

$$C_H = \begin{bmatrix} \cos H & -\sin H & 0 \\ \sin H & \cos H & 0 \\ 0 & 0 & 1 \end{bmatrix}$$

$$C_{\tilde{a}} = \begin{bmatrix} \cos \tilde{a} & 0 & \sin \tilde{a} \\ 0 & 1 & 0 \\ -\sin \tilde{a} & 0 & \cos \tilde{a} \end{bmatrix}$$

$$C_{f_v} = \begin{bmatrix} 1 & 0 & 0 \\ 0 & \cos f_v & -\sin f_v \\ 0 & \sin f_v & \cos f_v \end{bmatrix}$$

where the transformation matrix is

$$C_w^n = C_H \cdot C_{\tilde{a}} \cdot C_{f_v}$$

$$C_w^n = \begin{bmatrix} \cos \tilde{a} \cos H & \sin f_v \sin \tilde{a} \cos H - \cos f_v \sin H & \cos f_v \sin \tilde{a} \cos H + \sin f_v \sin H \\ \cos \tilde{a} \sin H & \sin f_v \sin \tilde{a} \sin H + \cos f_v \cos H & \cos f_v \sin \tilde{a} \sin H - \sin f_v \cos H \\ -\sin \tilde{a} & \sin f_v \cos \tilde{a} & \cos f_v \cos \tilde{a} \end{bmatrix} \quad (24)$$

Combined Rotations.

Now the combined wind and body axes rotation is given by

$$C_b^n = C_w^n \cdot C_b^w \quad (25)$$

$$\begin{aligned}
& \begin{bmatrix} \cos \epsilon \cos \Psi & \sin f \sin \epsilon \cos \Psi - \cos f \sin \Psi & \cos f \sin \epsilon \cos \Psi + \sin f \sin \Psi \\ \cos \epsilon \sin \Psi & \sin f \sin \epsilon \sin \Psi + \cos f \cos \Psi & \cos f \sin \epsilon \sin \Psi - \sin f \cos \Psi \\ -\sin \epsilon & \sin f \cos \epsilon & \cos f \cos \epsilon \end{bmatrix} = \\
& = \begin{bmatrix} \cos \tilde{\alpha} \cos H & \sin f_v \sin \tilde{\alpha} \cos H - \cos f_v \sin H & \cos f_v \sin \tilde{\alpha} \cos H + \sin f_v \sin H \\ \cos \tilde{\alpha} \sin H & \sin f_v \sin \tilde{\alpha} \sin H + \cos f_v \cos H & \cos f_v \sin \tilde{\alpha} \sin H - \sin f_v \cos H \\ -\sin \tilde{\alpha} & \sin f_v \cos \tilde{\alpha} & \cos f_v \cos \tilde{\alpha} \end{bmatrix} \cdot \\
& \begin{bmatrix} \cos \acute{\alpha} \cos \hat{\alpha} & -\sin \hat{\alpha} & \sin \acute{\alpha} \cos \hat{\alpha} \\ \cos \acute{\alpha} \sin \hat{\alpha} & \cos \hat{\alpha} & \sin \acute{\alpha} \sin \hat{\alpha} \\ -\sin \acute{\alpha} & 0 & \cos \acute{\alpha} \end{bmatrix} = \begin{bmatrix} c_{11} & c_{12} & c_{13} \\ c_{21} & c_{22} & c_{23} \\ c_{31} & c_{32} & c_{33} \end{bmatrix}
\end{aligned}$$

where

$$\begin{aligned}
c_{11} &= \cos \tilde{\alpha} \cos H \cos \acute{\alpha} \cos \hat{\alpha} + (\sin f_v \sin \tilde{\alpha} \cos H - \cos f_v \sin H) \cos \acute{\alpha} \sin \hat{\alpha} + \\
& \quad - (\cos f_v \sin \tilde{\alpha} \cos H + \sin f_v \sin H) \sin \acute{\alpha} \\
c_{12} &= -\cos \tilde{\alpha} \cos H \sin \hat{\alpha} + (\sin f_v \sin \tilde{\alpha} \cos H - \cos f_v \sin H) \cos \hat{\alpha} \\
c_{13} &= \cos \tilde{\alpha} \cos H \sin \acute{\alpha} \cos \hat{\alpha} + (\sin f_v \sin \tilde{\alpha} \cos H - \cos f_v \sin H) \sin \acute{\alpha} \sin \hat{\alpha} + \\
& \quad + (\cos f_v \sin \tilde{\alpha} \cos H + \sin f_v \sin H) \cos \acute{\alpha} \\
c_{21} &= \cos \tilde{\alpha} \sin H \cos \acute{\alpha} \cos \hat{\alpha} + (\sin f_v \sin \tilde{\alpha} \sin H + \cos f_v \cos H) \cos \acute{\alpha} \sin \hat{\alpha} + \\
& \quad - (\cos f_v \sin \tilde{\alpha} \sin H - \sin f_v \cos H) \sin \acute{\alpha} \\
c_{22} &= -\cos \tilde{\alpha} \sin H \sin \hat{\alpha} + (\sin f_v \sin \tilde{\alpha} \sin H + \cos f_v \cos H) \cos \hat{\alpha} \\
c_{23} &= \cos \tilde{\alpha} \sin H \sin \acute{\alpha} \cos \hat{\alpha} + (\sin f_v \sin \tilde{\alpha} \sin H + \cos f_v \cos H) \sin \acute{\alpha} \sin \hat{\alpha} + \\
& \quad + (\cos f_v \sin \tilde{\alpha} \sin H - \sin f_v \cos H) \cos \acute{\alpha} \\
c_{31} &= -\sin \tilde{\alpha} \cos \acute{\alpha} \cos \hat{\alpha} + \sin f_v \cos \tilde{\alpha} \cos \acute{\alpha} \sin \hat{\alpha} - \cos f_v \cos \tilde{\alpha} \sin \acute{\alpha} \\
c_{32} &= \sin \tilde{\alpha} \sin \hat{\alpha} + \sin f_v \cos \tilde{\alpha} \cos \hat{\alpha} \\
c_{33} &= -\sin \tilde{\alpha} \sin \acute{\alpha} \cos \hat{\alpha} + \sin f_v \cos \tilde{\alpha} \sin \acute{\alpha} \sin \hat{\alpha} + \cos f_v \cos \tilde{\alpha} \cos \acute{\alpha}
\end{aligned}$$

Navigation Angle Determination.

From the above matrix equations, the navigation axes angles were determined.

Equations for both the sine and cosine of the angles were determined to resolve the

quadrant of the angle. For an angle between 0 and $\frac{\delta}{2}$ both sine and cosine values are

positive. For positive sine values and negative cosine values, the angle is between $\frac{\delta}{2}$ and

$\frac{3\delta}{2}$. In the third quadrant (0 to $-\frac{\delta}{2}$), sine values are negative and cosine values are

positive. For an angle between $-\frac{\delta}{2}$ and $-\frac{3\delta}{2}$ both sine and cosine values are negative.

The navigation axes angles were found by solving the following equations. Setting individual elements of the transformation matrix equal

The first row, first column terms of both matrices are

$$\cos \delta \cos \Psi = c_{11}$$

The second row, first column terms of both matrices are

$$\cos \delta \sin \Psi = c_{21}$$

Squaring both equations and adding them together

$$\cos^2 \delta \cos^2 \Psi + \cos^2 \delta \sin^2 \Psi = c_{11}^2 + c_{21}^2$$

which with $\cos^2 \Psi + \sin^2 \Psi = 1$ yields

$$\cos \delta = \sqrt{c_{11}^2 + c_{21}^2} \quad (26)$$

From the third row, the first column terms are

$$\sin \delta = -c_{31} \quad (27)$$

From the first row, first column terms

$$\cos \Psi = \frac{c_{11}}{\cos \epsilon} = \frac{c_{11}}{\sqrt{c_{11}^2 + c_{21}^2}} \quad (28)$$

From the second row, first column terms

$$\sin \Psi = \frac{c_{21}}{\cos \epsilon} = \frac{c_{21}}{\sqrt{c_{11}^2 + c_{21}^2}} \quad (29)$$

From the third row, third column terms

$$\cos \mathbf{f} = \frac{c_{33}}{\cos \epsilon} = \frac{c_{33}}{\sqrt{c_{11}^2 + c_{21}^2}} \quad (30)$$

From the third row, second column terms

$$\sin \mathbf{f} = \frac{c_{32}}{\cos \epsilon} = \frac{c_{32}}{\sqrt{c_{11}^2 + c_{21}^2}} \quad (31)$$

Trim Condition Definitions

Therefore, two expressions were found for each of the navigation axes angles, ψ , θ , and ϕ , as functions of the wind axes variables. Specific trim conditions are then

examined, to determine simplified control laws. The equations are not defined at $\theta = 90^\circ$, therefore the flight with the nose straight up is not allowed.

Trim condition 1 corresponds to steady, straight and level flight. A straight and steady climb is described by trim condition 2. Trim condition 3, a straight and steady descent, is the opposite of trim condition 2. In trim condition 4, level crabbing flight is examined. Trim condition 5 is a steady level turn at a constant angular rate. Next, a steady climbing turn is defined in trim condition 6. Trim condition 7 is a steady descending turn, the opposite of trim condition 6. Trim condition 8 corresponds to a barrel roll. Next, trim condition 9 describes a steady turn orbit with a weapon pointing at a stationary target. Finally, trim condition 10 defines a steady level pitch-over.

Equations for each trim condition are now developed.

Trim Condition 1.

Trim condition 1, steady, straight and level flight is defined as $\gamma = \phi_v = H = 0^\circ$. The pitch angle, θ , is therefore equal to the angle of attack, α . The ϕ_v is zero and the heading angle, H , is equal to the sideslip angle, β . Sideslip angle is assumed to be zero for trim condition 1, so H is also zero. The Euler angles are therefore reduced to

$$\begin{aligned}\theta &= \alpha \\ \phi &= 0^\circ \\ \psi &= 0^\circ\end{aligned}\tag{32}$$

Trim Condition 2.

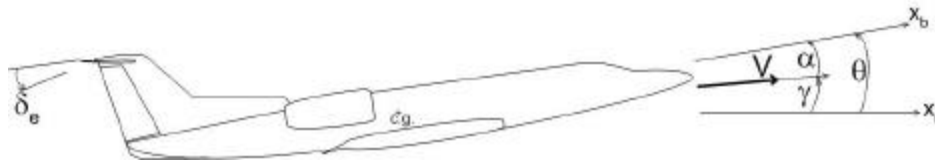


Figure 5. Aircraft Climb Definition

A straight and steady climb, trim condition 2, is obtained when $\phi_v = H = 0^\circ$ and γ is specified greater than zero. From equations (26) and (27) θ is a function of α , β and γ , but β is assumed to be zero. From equations (28), (29), (30) and (31) ϕ_v is zero since β is zero and ψ is also zero. The Euler angles then simplified to

$$\sin \theta = \sin \gamma \cos \alpha + \cos \gamma \sin \alpha$$

$$\cos \theta = \cos \gamma \cos \alpha - \sin \gamma \sin \alpha$$

$$\phi = 0^\circ \tag{33}$$

$$\cos \psi = 1$$

$$\sin \psi = 0$$

$$\psi = 0^\circ$$

Trim Condition 3.

Trim condition 3, a straight and steady descent, is $\phi_v = H = 0^\circ$ and $\gamma < 0^\circ$. The equations are identical to trim condition 2, (Equations 33), but the quadrant check is necessary to find the correct θ angle.

Trim Condition 4.

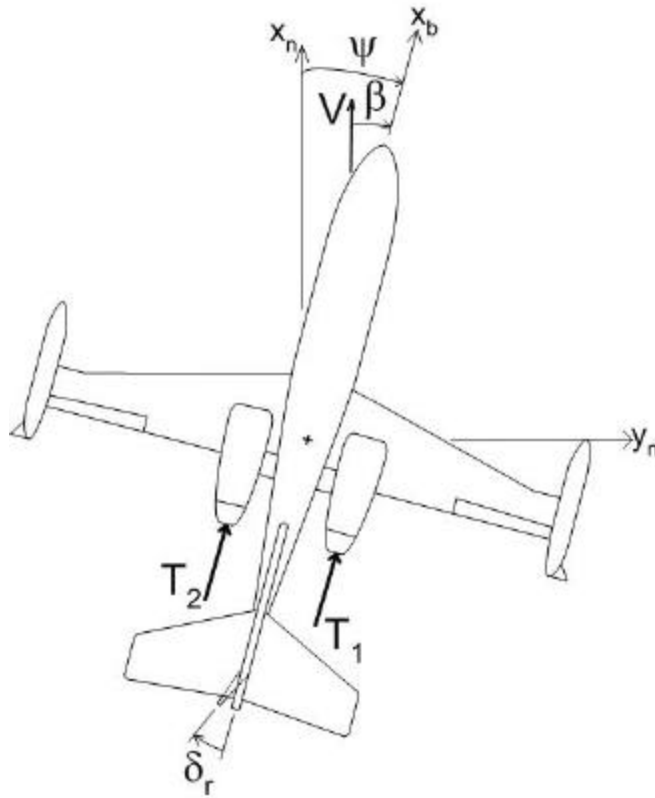


Figure 6. Aircraft Crabbing Flight Definition

A non-zero sideslip angle, crabbing flight, is described in trim condition 4.

Trimmed crabbing flight is defined by $\gamma = H = 0^\circ$ and $\beta \neq 0^\circ$. The angle ϕ_v is determined from the outer loop equations for the specified β . The Euler angles are found from equations (26) – (31) and are given by

$$\sin \theta = \cos \phi_v \sin \alpha - \sin \phi_v \cos \alpha \sin \beta$$

$$\cos \theta = \sqrt{c_{11}^2 + c_{21}^2} = \sqrt{(\cos \hat{a} \cos \hat{a})^2 + (\cos \hat{f}_v \cos \hat{a} \sin \hat{a} + \sin \hat{f}_v \sin \hat{a})^2}$$

$$\sin \phi = \frac{c_{32}}{\cos \epsilon} = \frac{\sin f_v \cos \hat{a}}{\cos \epsilon}$$

$$\cos \phi = \frac{c_{33}}{\cos \epsilon} = \frac{\sin f_v \sin \acute{a} \sin \hat{a} + \cos f_v \cos \acute{a}}{\cos \epsilon} \quad (34)$$

$$\sin \psi = \frac{c_{21}}{\cos \epsilon} = \frac{\cos f_v \cos \acute{a} \sin \hat{a} + \sin f_v \sin \acute{a}}{\cos \epsilon}$$

$$\cos \psi = \frac{c_{11}}{\cos \epsilon} = \frac{\cos \acute{a} \cos \hat{a}}{\cos \epsilon}$$

Trim Condition 5.

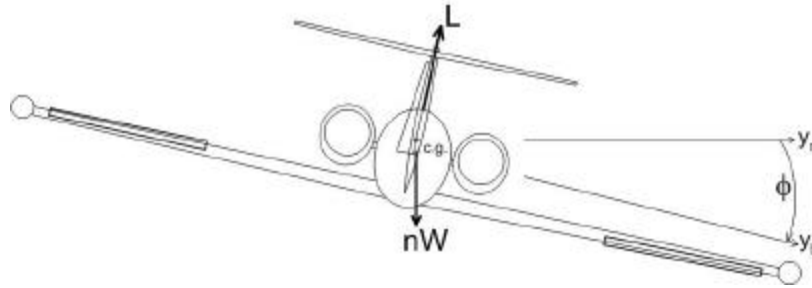


Figure 7. Aircraft Steady Turn Definition

Trim condition 5, a steady, level turn, is defined as $\gamma = 0^\circ$ and $H(t) = \mathbf{v}_\theta t$. Either β or ϕ_v is specified for the required turn, and the unspecified angle is determined by the outer-loop equations. The general equations for a turn are found first, and then simplifying assumptions are made. The Euler angles are

$$\sin \theta = \cos \phi_v \sin \alpha - \sin \phi_v \cos \alpha \sin \beta$$

$$\cos \theta = \sqrt{c_{11\psi}^2 + c_{21\psi}^2}$$

$$\sin \phi = \frac{c_{32}}{\cos \epsilon} = \frac{\sin \mathbf{f}_v \cos \hat{\alpha}}{\cos \epsilon}$$

$$\cos \phi = \frac{c_{33}}{\cos \epsilon} = \frac{\sin \mathbf{f}_v \sin \acute{\alpha} \sin \hat{\alpha} + \cos \mathbf{f}_v \cos \acute{\alpha}}{\cos \epsilon} \quad (35)$$

$$\sin \psi(t) = \frac{c_{21\psi}}{\cos \epsilon}$$

$$\cos \psi(t) = \frac{c_{11\psi}}{\cos \epsilon}$$

where the rotation matrix elements are given by

$$c_{11\psi} = \cos(\mathbf{v}_\psi t) \cos \acute{\alpha} \cos \hat{\alpha} - \cos \mathbf{f}_v \sin(\mathbf{v}_\psi t) \cos \acute{\alpha} \sin \hat{\alpha} - \sin \mathbf{f}_v \sin(\mathbf{v}_\psi t) \sin \acute{\alpha}$$

$$c_{21\psi} = \sin(\mathbf{v}_\psi t) \cos \acute{\alpha} \cos \hat{\alpha} + \cos \mathbf{f}_v \cos(\mathbf{v}_\psi t) \cos \acute{\alpha} \sin \hat{\alpha} + \sin \mathbf{f}_v \cos(\mathbf{v}_\psi t) \sin \acute{\alpha}$$

If the aircraft is assumed to have no sideslip in the turn ($\beta = 0^\circ$), the equations simplify to the following

$$\sin \theta = \cos \phi_v \sin \alpha$$

$$\cos \theta = \sqrt{\cos^2 \acute{\alpha} + \sin^2 \mathbf{f}_v \sin^2 \acute{\alpha}}$$

$$\sin \phi = \frac{\sin \mathbf{f}_v}{\cos \epsilon}$$

$$\cos \phi = \frac{\cos \mathbf{f}_v \cos \acute{\alpha}}{\cos \epsilon} \quad (35a)$$

$$\sin \psi(t) = \frac{\sin(\mathbf{v}_\psi t) \cos \acute{\alpha} + \sin \mathbf{f}_v \cos(\mathbf{v}_\psi t) \sin \acute{\alpha}}{\cos \epsilon}$$

$$\cos \psi(t) = \frac{\cos(\mathbf{v}_\psi t) \cos \acute{\alpha} - \sin \mathbf{f}_v \sin(\mathbf{v}_\psi t) \sin \acute{\alpha}}{\cos \epsilon}$$

If the aircraft is assumed to have no bank angle relative to the velocity in the turn ($\phi_v = 0^\circ$), the equations simplify to the following for the Euler angles

$$\begin{aligned}\theta &= \alpha \\ \phi &= 0^\circ \\ \psi(t) &= \mathbf{v}_\psi t + \hat{a}\end{aligned}\tag{35b}$$

Trim Condition 6.

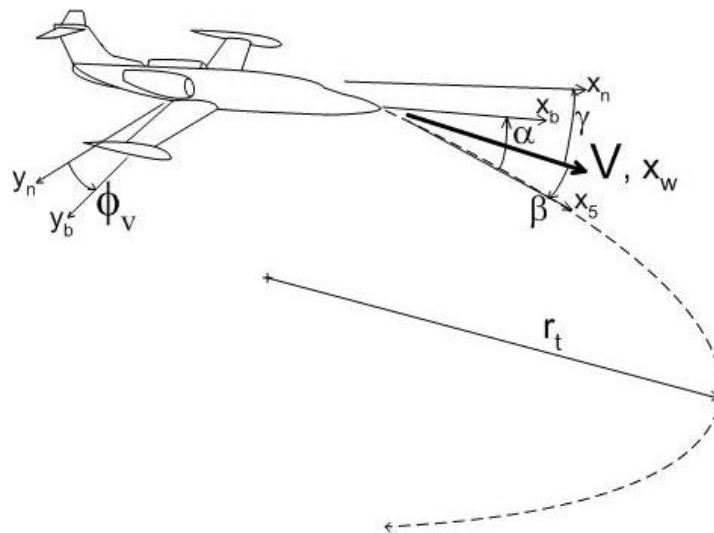


Figure 8. Aircraft Climbing Turn Definition

Trim condition 6, a steady climbing turn, is defined as $\gamma > 0^\circ$ and $H(t) = \mathbf{v}_\theta t$. Either β or ϕ_v is specified for the required turn, and the unspecified angle is determined by the outer-loop equations. The general equations for a turn are found first, and then simplifying assumptions are made. The Euler angles are

$$\sin \theta = \sin \tilde{\alpha} \cos \acute{\alpha} \cos \hat{\alpha} - \sin \mathbf{f}_v \cos \tilde{\alpha} \cos \acute{\alpha} \sin \hat{\alpha} + \cos \mathbf{f}_v \cos \tilde{\alpha} \sin \acute{\alpha}$$

$$\cos \theta = \sqrt{c_{11}^2 + c_{21}^2} \quad (\text{where } H(t) = \mathbf{v}_\theta t)$$

$$\sin \phi = \frac{c_{32}}{\cos \grave{\epsilon}} \quad (\text{where } H(t) = \mathbf{v}_\theta t)$$

$$\cos \phi = \frac{c_{33}}{\cos \grave{\epsilon}} \quad (\text{where } H(t) = \mathbf{v}_\theta t) \quad (36)$$

$$\sin \psi(t) = \frac{c_{21}}{\cos \grave{\epsilon}} \quad (\text{where } H(t) = \mathbf{v}_\theta t)$$

$$\cos \psi(t) = \frac{c_{11}}{\cos \grave{\epsilon}} \quad (\text{where } H(t) = \mathbf{v}_\theta t)$$

If the aircraft is assumed to have no sideslip in the turn ($\beta = 0^\circ$), the equations simplify to the following

$$\sin \theta = \sin \tilde{\alpha} \cos \acute{\alpha} + \cos \mathbf{f}_v \cos \tilde{\alpha} \sin \acute{\alpha}$$

$$\sin \phi = \frac{\sin \mathbf{f}_v \cos \tilde{\alpha}}{\cos \grave{\epsilon}} \quad (36a)$$

$$\sin \psi(t) = \frac{\cos \tilde{\alpha} \sin(\mathbf{v}_\psi t) \cos \acute{\alpha} - [\cos \mathbf{f}_v \sin \tilde{\alpha} \sin(\mathbf{v}_\theta t) - \sin \mathbf{f}_v \cos(\mathbf{v}_\psi t)] \sin \acute{\alpha}}{\cos \grave{\epsilon}}$$

If the aircraft is assumed to have no bank angle relative to the velocity in the turn ($\phi_v = 0^\circ$), the equations simplify to the following

$$\sin \theta = \sin \tilde{\alpha} \cos \hat{\alpha} \cos \hat{\alpha} + \cos \tilde{\alpha} \sin \hat{\alpha}$$

$$\sin \phi = \frac{\sin \hat{\alpha} \sin \tilde{\alpha}}{\cos \hat{\epsilon}} \quad (36b)$$

$$\sin \psi(t) =$$

$$\frac{\cos \tilde{\alpha} \sin(\mathbf{v}_\psi t) \cos \hat{\alpha} \cos \hat{\alpha} + \cos \mathbf{f}_v \cos(\mathbf{v}_\theta t) \cos \hat{\alpha} \cos \hat{\alpha} - \cos \mathbf{f}_v \sin \tilde{\alpha} \sin(\mathbf{v}_\theta t) \sin \hat{\alpha}}{\cos \hat{\epsilon}}$$

Trim Condition 7.

Trim condition 7, a steady descending turn, is defined as $\gamma < 0^\circ$ and $H(t) = \mathbf{v}_\theta t$.

The equations are identical to trim condition 6, (Equations 36), but a quadrant check is necessary to find the correct θ , ϕ and $\psi(t)$ angles.

Trim Condition 8.

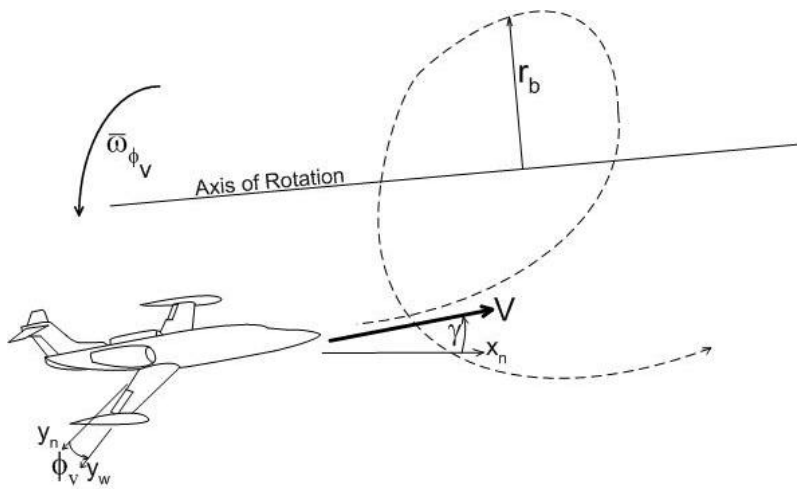


Figure 9. Aircraft Barrel Roll Definition

Trim condition 8, a steady barrel roll, is defined as $\beta = H = 0^\circ$ and $\phi_v(t) = \mathbf{v}_{f_v} t$.

The angle, γ , must also be specified. The Euler angles are

$$\sin \theta(t) = \sin \tilde{\alpha} \cos \acute{\alpha} \cos \hat{\alpha} + \cos(\mathbf{v}_{f_v} t) \cos \tilde{\alpha} \sin \acute{\alpha}$$

$$\cos \theta(t) = \sqrt{c_{11}^2 + c_{21}^2} = \sqrt{(\cos \tilde{\alpha} \cos \acute{\alpha})^2 - 2 \cos \tilde{\alpha} \cos \acute{\alpha} \cos(\mathbf{v}_{f_v} t) \sin \tilde{\alpha} + [\cos(\mathbf{v}_{f_v} t) \sin \tilde{\alpha} \sin \acute{\alpha}]^2 + [\sin(\mathbf{v}_{f_v} t) \sin \acute{\alpha}]^2}$$

$$\sin \phi(t) = \frac{c_{32}}{\cos \grave{\epsilon}} = \frac{\sin(\mathbf{v}_{f_v} t) \cos \tilde{\alpha}}{\cos \grave{\epsilon}}$$

$$\cos \phi(t) = \frac{c_{33}}{\cos \grave{\epsilon}} = \frac{\sin \tilde{\alpha} \sin \acute{\alpha} + \cos(\mathbf{v}_{f_v} t) \cos \tilde{\alpha} \cos \acute{\alpha}}{\cos \grave{\epsilon}} \quad (37)$$

$$\sin \psi(t) = \frac{c_{21}}{\cos \grave{\epsilon}} = \frac{\sin(\mathbf{v}_{f_v} t) \sin \acute{\alpha}}{\cos \grave{\epsilon}}$$

$$\cos \psi(t) = \frac{c_{11}}{\cos \grave{\epsilon}} = \frac{\cos \tilde{\alpha} \cos \acute{\alpha} - \cos(\mathbf{v}_{f_v} t) \sin \tilde{\alpha} \sin \acute{\alpha}}{\cos \grave{\epsilon}}$$

The three equations were solved together to form an expression for aircraft height (Equation 38). Sample calculations are shown in Appendix A. The equations combine to form

$$h = \frac{1 + \frac{1}{\sqrt{n^2 - 1}} \tan \mathbf{e}}{1 - \sqrt{n^2 - 1} \tan \mathbf{e}} \frac{V^2}{g} \quad (38)$$

Therefore, the required aircraft height above the target is only a function of airspeed, load factor, and weapon depression angle. If the weapon depression angle is reduced to zero, the required aircraft height equation reduces to $h = V^2/g$. To increase the height above the ground, the weapon depression angle must be increased. If ε is assumed to be a non-zero positive number, the maximum height is found by differentiating equation (38) and setting it equal to zero. Simplifying the equation results in $n_{h\max} = \sqrt{2}$. Substituting the load factor for maximum height produces equations (39) for the maximum height above the target, maximum bank angle and radius.

$$h_{\max} = \frac{1 + \tan \mathbf{e}}{1 - \tan \mathbf{e}} \frac{V^2}{g}$$

$$\phi_{v\max} = 45^\circ \quad (39)$$

$$r_{t\max} = \frac{V^2}{g}$$

The h_{\max} equation (39) is undefined at $\epsilon = 45^\circ$, therefore the maximum height above the target occurs as ϵ approaches 45° with a bank angle of 45° or essentially pointing straight down.

Trim Condition 10.

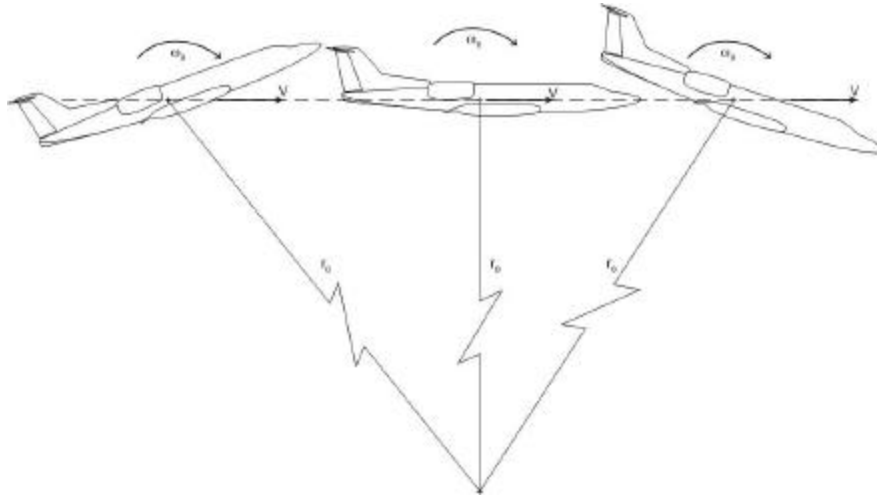


Figure 11. Aircraft Pitch-over Definition

Trim condition 10, a level flight pitch over, is a subset of trim condition 1 ($\dot{\alpha} = \dot{\beta} = \dot{\gamma} = 0^\circ$). This maneuver is envisioned for use at pointing a fixed line-of-sight weapon from the bottom of the aircraft at a stationary target. The pitch change rate, ω_θ , is a function of aircraft velocity and r_θ . Therefore $r_\theta = V/\omega_\theta$ to point at a stationary target below the aircraft.

Aircraft Rotation Rate Determination

With the Euler angles in the navigation frame, the aircraft angular change rates resolved in the body axes are then determined. Steady level flight ($\dot{\alpha} = \dot{\beta} = \dot{\gamma} = 0^\circ$), is a

subset of a steady turn ($\dot{\psi} = \dot{\alpha} = 0^\circ; \dot{\phi} \neq 0^\circ$). The inner-loop equations are solved for a steady turn. From the Euler equation (1: Chapter 2).

$$\begin{bmatrix} \dot{\phi} \\ \dot{\alpha} \\ \dot{\psi} \end{bmatrix} = \begin{bmatrix} 1 & \sin f \tan \epsilon & \cos f \tan \epsilon \\ 0 & \cos f & -\sin f \\ 0 & \sin f \sec \epsilon & \cos f \sec \epsilon \end{bmatrix} \cdot \begin{bmatrix} P \\ Q \\ R \end{bmatrix} = \begin{bmatrix} 0 \\ 0 \\ \dot{\phi} \end{bmatrix}$$

the aircraft angular rates are obtained

$$\begin{bmatrix} P \\ Q \\ R \end{bmatrix} = \begin{bmatrix} 1 & \sin f \tan \epsilon & \cos f \tan \epsilon \\ 0 & \cos f & -\sin f \\ 0 & \sin f \sec \epsilon & \cos f \sec \epsilon \end{bmatrix}^{-1} \cdot \begin{bmatrix} 0 \\ 0 \\ \dot{\phi} \end{bmatrix}$$

$$\begin{bmatrix} P \\ Q \\ R \end{bmatrix} = \begin{bmatrix} -\dot{\phi} \sin \epsilon \\ \dot{\phi} \sin f \cos \epsilon \\ \dot{\phi} \cos f \cos \epsilon \end{bmatrix} \quad (40)$$

For the aircraft in a steady level pitch over, the equations become

$$\begin{bmatrix} \dot{\phi} \\ \dot{\alpha} \\ \dot{\psi} \end{bmatrix} = \begin{bmatrix} 1 & \sin f \tan \epsilon & \cos f \tan \epsilon \\ 0 & \cos f & -\sin f \\ 0 & \sin f \sec \epsilon & \cos f \sec \epsilon \end{bmatrix} \cdot \begin{bmatrix} P \\ Q \\ R \end{bmatrix} = \begin{bmatrix} 0 \\ \mathbf{w}_q \\ 0 \end{bmatrix}$$

the aircraft angular rates are obtained

$$\begin{bmatrix} P \\ Q \\ R \end{bmatrix} = \begin{bmatrix} 1 & \sin f \tan \epsilon & \cos f \tan \epsilon \\ 0 & \cos f & -\sin f \\ 0 & \sin f \sec \epsilon & \cos f \sec \epsilon \end{bmatrix}^{-1} \cdot \begin{bmatrix} 0 \\ \mathbf{w}_q \\ 0 \end{bmatrix}$$

$$\begin{bmatrix} P \\ Q \\ R \end{bmatrix} = \begin{bmatrix} 0 \\ \mathbf{w}_q \cos f \\ -\mathbf{w}_q \sin f \end{bmatrix} \quad (41)$$

For the aircraft in a steady roll, the equations become

$$\begin{bmatrix} \dot{\phi} \\ \dot{\psi} \\ \dot{\chi} \end{bmatrix} = \begin{bmatrix} 1 & \sin \mathbf{f} \tan \epsilon & \cos \mathbf{f} \tan \epsilon \\ 0 & \cos \mathbf{f} & -\sin \mathbf{f} \\ 0 & \sin \mathbf{f} \sec \epsilon & \cos \mathbf{f} \sec \epsilon \end{bmatrix} \cdot \begin{bmatrix} \mathbf{P} \\ \mathbf{Q} \\ \mathbf{R} \end{bmatrix} = \begin{bmatrix} \mathbf{w}_{f_v} \\ 0 \\ 0 \end{bmatrix}$$

the aircraft angular rates are obtained

$$\begin{bmatrix} \mathbf{P} \\ \mathbf{Q} \\ \mathbf{R} \end{bmatrix} = \begin{bmatrix} 1 & \sin \mathbf{f} \tan \epsilon & \cos \mathbf{f} \tan \epsilon \\ 0 & \cos \mathbf{f} & -\sin \mathbf{f} \\ 0 & \sin \mathbf{f} \sec \epsilon & \cos \mathbf{f} \sec \epsilon \end{bmatrix}^{-1} \cdot \begin{bmatrix} \mathbf{w}_{f_v} \\ 0 \\ 0 \end{bmatrix}$$

$$\begin{bmatrix} \mathbf{P} \\ \mathbf{Q} \\ \mathbf{R} \end{bmatrix} = \begin{bmatrix} \mathbf{w}_{f_v} \\ 0 \\ 0 \end{bmatrix}$$

(42)

Control Surface Deflection Determination

The six-degree-of-freedom equations of motion are used to find the aircraft control surface deflections from the equations previously determined. Figure 12 shows the definition of moments and forces.

Moment Model Definition.

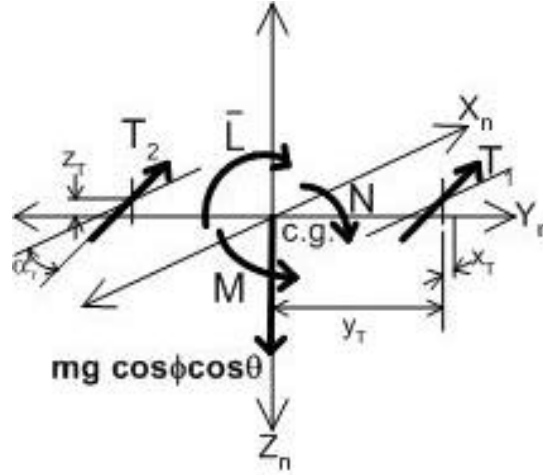


Figure 12. Three Dimensional Aircraft Moments and Forces

The thrust term, T , from the outer loop model was divided into two terms, T_1 and T_2 . T_1 is the thrust from the right side engine, while T_2 is the thrust from the left side engine. The three moment of inertia equations of motion are (1: Chapter 2)

$$\dot{P} = (c_1 R + c_2 P)Q + c_3 \bar{L} + c_4 N \quad (43)$$

$$\dot{Q} = c_5 PR - c_6 (P^2 - R^2) + c_7 M \quad (44)$$

$$\dot{R} = (c_8 P - c_2 R)Q + c_4 \bar{L} + c_9 N \quad (45)$$

with the following definitions

$$c_1 = \frac{(I_{yy} - I_{zz})I_{zz} - I_{xz}^2}{I_{xx}I_{zz} - I_{xz}^2} = C_{1_{qr}}$$

$$c_2 = \frac{(I_{xx} - I_{yy} + I_{zz})I_{xz}}{I_{xx}I_{zz} - I_{xz}^2} = C_{1_{pr}} = C_{n_{qr}}$$

$$c_3 = \frac{I_{zz}}{I_{xx}I_{zz} - I_{xz}^2}$$

$$c_4 = \frac{I_{xz}}{I_{xx}I_{zz} - I_{xz}^2}$$

$$c_5 = \frac{I_{zz} - I_{xx}}{I_{yy}} = C_{m_{pr}}$$

$$c_6 = \frac{I_{xz}}{I_{yy}} = C_{m_{p^2r^2}}$$

$$c_7 = \frac{1}{I_{yy}}$$

$$c_8 = \frac{(I_{xx} - I_{yy})I_{xz} + I_{xz}^2}{I_{xx}I_{zz} - I_{xz}^2}$$

$$c_9 = \frac{I_{xx}}{I_{xx}I_{zz} - I_{xz}^2}$$

$$\bar{L} = \bar{L}_p + \bar{L}_R + \bar{L}_{\dot{\alpha}} + \bar{L}_{\dot{\alpha}_a} + \bar{L}_{\dot{\alpha}_r} + \bar{L}_T$$

$$M = M_o + M_{\dot{\alpha}} + M_{\dot{\alpha}_c} + M_Q + M_{\dot{\alpha}_e} - M_T$$

$$N = N_p + N_R + N_{\dot{\alpha}} + N_{\dot{\alpha}_a} + N_{\dot{\alpha}_r} + N_T$$

$$T = T_1 + T_2$$

Roll Moment Definition.

The roll moment, \bar{L} , is defined as all moments about the x_n -axis. \bar{L} is composed of the following terms

$$\bar{L}_p = C_{l_p} P \cdot \bar{q} b \text{ (Roll moment due to aircraft roll rate)}$$

$$\bar{L}_R = C_{l_r} R \cdot \bar{q} b \text{ (Roll moment due to aircraft roll yaw)}$$

$$\bar{L}_\beta = C_{l_\beta} \hat{\alpha} \cdot \bar{q} b \text{ (Roll moment due to aircraft sideslip angle)}$$

$$\bar{L}_{\dot{\alpha}_a} = C_{l_{\dot{\alpha}_a}} \dot{\alpha}_a \cdot \bar{q} b \text{ (Roll moment due to aircraft aileron deflection)}$$

$$\bar{L}_{\dot{\alpha}_r} = C_{l_{\dot{\alpha}_r}} \dot{\alpha}_r \cdot \bar{q} b \text{ (Roll moment due to aircraft rudder deflection)}$$

$$\bar{L}_T = y_T \sin \hat{\alpha}_T (T_2 - T_1) \text{ (Roll moment due to asymmetrical thrust)}$$

Pitch Moment Definition.

The pitch moment, M , is defined as all moments about the y_n -axis. M is composed of the following terms

$$M_o = C_{m_o} \bar{q} \bar{c} \text{ (Equilibrium pitch moment)}$$

$$M_\alpha = C_{m_\alpha} \hat{\alpha} \cdot \bar{q} \bar{c} \text{ (Pitch moment due to aircraft angle of attack)}$$

$$M_{\dot{\alpha}} = C_{m_{\dot{\alpha}}} \dot{\alpha} \cdot \bar{q} \bar{c} \text{ (Pitch moment due to the change in aircraft angle of attack)}$$

$$M_Q = C_{m_q} Q \cdot \bar{q} \bar{c} \text{ (Pitch moment due to aircraft pitch rate)}$$

$$M_{\dot{\alpha}_e} = C_{m_{\dot{\alpha}_e}} \dot{\alpha}_e \cdot \bar{q} \bar{c} \text{ (Pitch moment due to aircraft elevator deflection)}$$

$$M_T = (z_T \cos \hat{\alpha}_T + x_T \sin \hat{\alpha}_T)(T_1 + T_2) \text{ (Pitch moment due to thrust)}$$

Yaw Moment Definition.

The yaw moment, N , is defined as all moments about the z_n -axis. N is composed of the following terms

$$N_P = C_{n_p} P \cdot \bar{q} b \text{ (Yaw moment due to aircraft roll rate)}$$

$$N_R = C_{n_r} R \cdot \bar{q} b \text{ (Yaw moment due to aircraft roll yaw)}$$

$$N_{\beta} = C_{n_{\beta}} \hat{\alpha} \cdot \bar{q} b \text{ (Yaw moment due to aircraft sideslip angle)}$$

$$N_{\ddot{\alpha}_a} = C_{n_{\ddot{\alpha}_a}} \ddot{\alpha}_a \cdot \bar{q} b \text{ (Yaw moment due to aircraft aileron deflection)}$$

$$N_{\ddot{\alpha}_r} = C_{n_{\ddot{\alpha}_r}} \ddot{\alpha}_r \cdot \bar{q} b \text{ (Yaw moment due to aircraft rudder deflection)}$$

$$N_T = y_T \cos \hat{\alpha}_T (T_2 - T_1) \text{ (Yaw moment due to asymmetrical thrust)}$$

Control Surface Deflection Equations.

With moment equations of motion, aircraft trim conditions are determined. In the most general trim condition, all three angular accelerations (\dot{P} , \dot{Q} , and \dot{R}) were set to zero. With the appropriate variable substitutions, the equations of motion (43)-(45) are

$$\dot{P} = 0 =$$

$$C_{l_{pq}} PQ + C_{l_{qr}} QR + c_3 \bar{q} b (C_{l_p} P + C_{l_r} R + C_{l_{\hat{\alpha}}} \hat{\alpha} + C_{l_{\ddot{\alpha}_a}} \ddot{\alpha}_a + C_{l_{\ddot{\alpha}_r}} \ddot{\alpha}_r) + c_3 y_T \sin \hat{\alpha}_T (T_2 - T_1) + c_4 \bar{q} b (C_{n_p} P + C_{n_r} R + C_{n_{\hat{\alpha}}} \hat{\alpha} + C_{n_{\ddot{\alpha}_a}} \ddot{\alpha}_a + C_{n_{\ddot{\alpha}_r}} \ddot{\alpha}_r) + c_4 y_T \cos \hat{\alpha}_T (T_2 - T_1) \quad (46)$$

$$\dot{Q} = 0 =$$

$$C_{m_{pr}} PR + C_{m_{p^2r^2}} (R^2 - P^2) + c_7 \bar{q} c (C_{m_o} + C_{m_{\hat{\alpha}}} \hat{\alpha} + C_{m_q} Q + C_{m_{\ddot{\alpha}_e}} \ddot{\alpha}_e) + - c_7 (z_T \cos \hat{\alpha}_T + x_T \sin \hat{\alpha}_T) (T_1 + T_2) \quad (47)$$

$$\dot{R} = 0 =$$

$$C_{n_{pq}} PQ - C_{n_{qr}} QR + c_9 \bar{q} b (C_{n_p} P + C_{n_r} R + C_{n_{\hat{\alpha}}} \hat{\alpha} + C_{n_{\ddot{\alpha}_a}} \ddot{\alpha}_a + C_{n_{\ddot{\alpha}_r}} \ddot{\alpha}_r) + c_9 y_T \cos \hat{\alpha}_T (T_2 - T_1) + c_4 \bar{q} b (C_{l_p} P + C_{l_r} R + C_{l_{\hat{\alpha}}} \hat{\alpha} + C_{l_{\ddot{\alpha}_a}} \ddot{\alpha}_a + C_{l_{\ddot{\alpha}_r}} \ddot{\alpha}_r) + c_4 y_T \sin \hat{\alpha}_T (T_2 - T_1)$$

(48)

Solving equations (46) and (48) for δ_a and δ_r results in the following matrix

$$\begin{bmatrix} c_3 C_{l_{\ddot{a}_a}} + c_4 C_{n_{\ddot{a}_a}} & c_3 C_{l_{\ddot{a}_r}} + c_4 C_{n_{\ddot{a}_r}} \\ c_9 C_{n_{\ddot{a}_a}} + c_4 C_{l_{\ddot{a}_a}} & c_9 C_{n_{\ddot{a}_r}} + c_4 C_{l_{\ddot{a}_r}} \end{bmatrix} \begin{bmatrix} \ddot{a}_a \\ \ddot{a}_r \end{bmatrix} = \frac{-1}{\overline{qb}} \begin{bmatrix} c_p \\ c_r \end{bmatrix}$$

where

$$\begin{aligned} c_p &= C_{l_{pq}} PQ + C_{l_{qr}} QR + c_3 y_T \sin \acute{a}_T (T_2 - T_1) + c_4 y_T \cos \acute{a}_T (T_2 - T_1) + \\ &+ \overline{qb} [c_3 (C_{l_p} P + C_{l_r} R + C_{l_a} \hat{a}) + c_4 (C_{n_p} P + C_{n_r} R + C_{n_a} \hat{a})] \\ c_r &= C_{n_{pq}} PQ - C_{n_{qr}} QR + c_9 y_T \cos \acute{a}_T (T_2 - T_1) + c_4 y_T \sin \acute{a}_T (T_2 - T_1) + \\ &+ \overline{qb} [c_9 (C_{n_p} P + C_{n_r} R + C_{n_a} \hat{a}) + c_4 (C_{l_p} P + C_{l_r} R + C_{l_a} \hat{a})] \end{aligned}$$

which simplifies to

$$\begin{bmatrix} \ddot{a}_a \\ \ddot{a}_r \end{bmatrix} = \frac{\begin{bmatrix} c_r (c_3 C_{l_{\ddot{a}_r}} + c_4 C_{n_{\ddot{a}_r}}) - c_p (c_9 C_{n_{\ddot{a}_r}} + c_4 C_{l_{\ddot{a}_r}}) \\ c_p (c_9 C_{n_{\ddot{a}_a}} + c_4 C_{l_{\ddot{a}_a}}) - c_r (c_3 C_{l_{\ddot{a}_a}} + c_4 C_{n_{\ddot{a}_a}}) \end{bmatrix}}{\overline{qb} [(c_3 C_{l_{\ddot{a}_a}} + c_4 C_{n_{\ddot{a}_a}})(c_9 C_{n_{\ddot{a}_r}} + c_4 C_{l_{\ddot{a}_r}}) - (c_3 C_{l_{\ddot{a}_r}} + c_4 C_{n_{\ddot{a}_r}})(c_9 C_{n_{\ddot{a}_a}} + c_4 C_{l_{\ddot{a}_a}})]} \quad (49)$$

Solving equation (47) for δ_e

$\delta_e =$

$$\frac{c_7 (z_T \cos \acute{a}_T + x_T \sin \acute{a}_T) (T_1 + T_2) - C_{m_{pr}} PR - C_{m_{p^2,2}} (R^2 - P^2) - \frac{C_{m_o} + C_{m_a} \acute{a} + C_{m_{\delta}} \delta + C_{m_q} Q}{C_{m_{\delta}}}}{C_{m_{\delta}} c_7 \overline{qc}} \quad (50)$$

If it is assumed that the thrust is the same from both engines ($T_1=T_2$), Equation (50) simplifies to the lateral-direction equations

$$\begin{bmatrix} \ddot{a}_a \\ \ddot{a}_r \end{bmatrix} = \frac{\begin{bmatrix} c_{r_{oT}} (c_3 C_{l_{\ddot{a}_r}} + c_4 C_{n_{\ddot{a}_r}}) - c_{p_{oT}} (c_9 C_{n_{\ddot{a}_r}} + c_4 C_{l_{\ddot{a}_r}}) \\ c_{p_{oT}} (c_9 C_{n_{\ddot{a}_a}} + c_4 C_{l_{\ddot{a}_a}}) - c_{r_{oT}} (c_3 C_{l_{\ddot{a}_a}} + c_4 C_{n_{\ddot{a}_a}}) \end{bmatrix}}{\bar{q}b[(c_3 C_{l_{\ddot{a}_a}} + c_4 C_{n_{\ddot{a}_a}})(c_9 C_{n_{\ddot{a}_r}} + c_4 C_{l_{\ddot{a}_r}}) - (c_3 C_{l_{\ddot{a}_r}} + c_4 C_{n_{\ddot{a}_r}})(c_9 C_{n_{\ddot{a}_a}} + c_4 C_{l_{\ddot{a}_a}})]} \quad (51)$$

where

$$\begin{aligned} c_{p_{oT}} &= C_{l_{pq}} PQ + C_{l_{qr}} QR + \bar{q}b[c_3(C_{l_p} P + C_{l_r} R + C_{l_a} \hat{a}) + c_4(C_{n_p} P + C_{n_r} R + C_{n_a} \hat{a})] \\ c_{r_{oT}} &= C_{n_{pq}} PQ - C_{n_{qr}} QR + \bar{q}b[c_9(C_{n_p} P + C_{n_r} R + C_{n_a} \hat{a}) + c_4(C_{l_p} P + C_{l_r} R + C_{l_a} \hat{a})] \end{aligned}$$

The longitudinal equation (50) is not simplified by this assumption, since both engines thrust produce the same longitudinal moment.

Summary

In this chapter, inner-loop equations were developed to solve the control surface deflections, from a given set of control variables and state variables. For a desired trajectory and orientation the state variables were determined and the outer-loop equations were used to solve the required control variables. The equations developed in this chapter used the values from the outer-loop and the desired angular acceleration values in an inner-loop system to determine the required control surface deflections.

Therefore, by choosing the variables h_o , \tilde{a} , $\frac{V}{V_o}$, $(\mathbf{f}_v \text{ or } \hat{a})$, H , \mathbf{v}_e , \mathbf{v}_θ , \mathbf{v}_f and T_1 to describe the flight path, the required aircraft settings are found. Now that the equations were developed, specific flight paths and orientations are examined and control surface deflections calculated in the next chapter.

IV. Aircraft Flight Trajectories

Overview

In Chapter 2, the point mass model was developed to provide a basis for the control laws for the trajectory of the aircraft. The outer-loop equations were found from the nonlinear equations of motion and applied to the actual Learjet-25 parameters. In Chapter 3, the outer-loop equation outputs were used with the transformation matrices and the remainder of the equations of motion to find the control surface deflections required to achieve the desired flight trajectory and orientation. In Chapter 4, the equations developed in the previous two chapters are used to simulate selected flight trajectories. By choosing the correct input states, the required control surface deflections for the desired flight path are found. Selected aircraft flight trajectories are examined using the control laws developed in the last two chapters. By choosing the correct input states, the desired flight path and orientation for the Learjet-25 is determined. The impacts of variations in the stability derivatives are investigated in Chapter 5 to determine which parameters require the most accuracy. Finally, in Chapter 6 the theoretical values tested using the Learjet-25 in flight tests are compared to the theoretical calculations.

The control laws are developed to provide an automatic control system for the aircraft. The goal was to provide simple inputs, to produce the necessary performance from the aircraft. A Matlab® routine was developed, using the aircraft control laws, to

solve the equations from the state variable inputs. The Matlab® commands are shown in the Appendix B.

Trim Condition Investigation

In this chapter, input state variable scenarios are examined to determine the predicted aircraft behavior. The results are compared to the equations from Chapter 3. Each of the trim conditions is solved for the required control surface deflections. The most basic case examined is trimmed steady, level flight on a straight trajectory, trim condition 1. Next, trim conditions 2 and 3, climbs and descents, are explored by varying the aircraft flight path angle. Aircraft crabbing (trim condition 4), flight with non-zero sideslip, is investigated by varying β and the resulting ϕ_v . Then the different definitions of a steady-level turn are examined by solving the variations of trim condition 5. Next, trim conditions 6 and 7, trimmed climbing and descending turns, are examined. The barrel roll, trim condition 8, is examined by setting the change in roll angle equal to a constant. Next, the special case of the AC-130 gunship flight maneuver (trim condition 9) is studied. The flight trajectory is defined by a steady, level turn with the gun barrel pointing out the side of the aircraft pointing at a stationary target. Trim condition 10, a constant rate pitch over, is the last trimmed flight maneuver evaluated. Each trim condition maneuver are now detailed.

Trim Condition 1 Investigation.

The first flight condition examined was the most basic trimmed condition: level flight with no turning. All the input states, \hat{a} , \hat{f}_v , \tilde{a} , \hat{f}_v^* , \hat{e} , and \hat{H} , are set equal to zero. First the validity of the equations over the operational envelope was investigated. After finding the trimmed steady, level flight condition, the remaining flight input parameters

were varied to show the affect on the control surface deflection values. The altitude was varied between 9,000 and 20,000 feet (ft), to determine the effect on the trimmed flight condition. By changing the altitude, the standard atmosphere density and temperature changes, which affects the amount of elevator deflection (δ_e) and thrust (T) required from the engines. Next, the influence of aircraft weight on T and δ_e was investigated by varying the aircraft gross weight. The airspeed effects were then examined by varying the aircraft velocity from the equilibrium value. Finally, asymmetrical thrust was analyzed by varying the amount of thrust from the right engine at the trimmed steady level-flight condition. Asymmetrical thrust could be used as a control input to create yawing moments about the center of gravity.

A center test point flight condition was chosen to standardize the flight parameters. A standard aerospace atmosphere and constant gravitational acceleration were chosen to perform all the calculations since simplified models exist and are typically used to allow comparisons between test conditions. The aircraft derivatives were assumed valid from 9,000 to 20,000 ft, the standard test altitude was chosen as 15,000 ft. Standard atmosphere equations were used to calculate the corresponding density and temperature for the selected altitude. Also, the derivatives were assumed applicable for aircraft velocities between 237 knots indicated airspeed (KIAS) and 326 KIAS. Therefore 267 KIAS (approximately 450 feet per second) was chosen as the standard test velocity. The center test point operating weight for the Learjet-25 was chosen to be 13,500 pounds (lbs).

The control law equations were solved at the center test point conditions. The rudder, δ_r , and aileron deflections, δ_a , are zero, since the aircraft does not produce lateral-

directional moments in steady level flight. The required elevator deflection, δ_e , was -0.02 radians (rad) or -1.17 degrees (deg), for level flight at the center test point condition. It was found that the aircraft nose must point up slightly to maintain level flight, so the angle of attack, α , and the pitch angle, θ , were both 0.0782 rad (4.48°). The angles α and θ are the same since all other aircraft angles are zero. These values match the equations (32) found in Chapter 3. For steady level flight at the standard test condition, the aircraft required 1,053 lbs of thrust. The angular velocities ($\dot{\alpha}$, $\dot{\beta}$, $\dot{\gamma}$, $\dot{\delta}$, $\dot{\epsilon}$, $\dot{\eta}$, $\dot{\theta}$, $\dot{\phi}$, $\dot{\psi}$, P, Q, and R) and accelerations ($\ddot{\alpha}$, $\ddot{\beta}$, $\ddot{\gamma}$, $\ddot{\delta}$, $\ddot{\epsilon}$, $\ddot{\eta}$, $\ddot{\theta}$, $\ddot{\phi}$, $\ddot{\psi}$, \ddot{P} , \ddot{Q} , and \ddot{R}), and aircraft angles ($\hat{\alpha}$, $\hat{\beta}$, $\hat{\gamma}$, $\hat{\delta}$, $\hat{\epsilon}$, $\hat{\eta}$, $\hat{\theta}$, $\hat{\phi}$, $\hat{\psi}$, \hat{P} , \hat{Q} , and \hat{R}) were all zero. This flight condition is used as the baseline for comparison for the remainder of the flight scenarios examined. The first flight parameter explored is the altitude effect.

Altitude Effect Investigation.

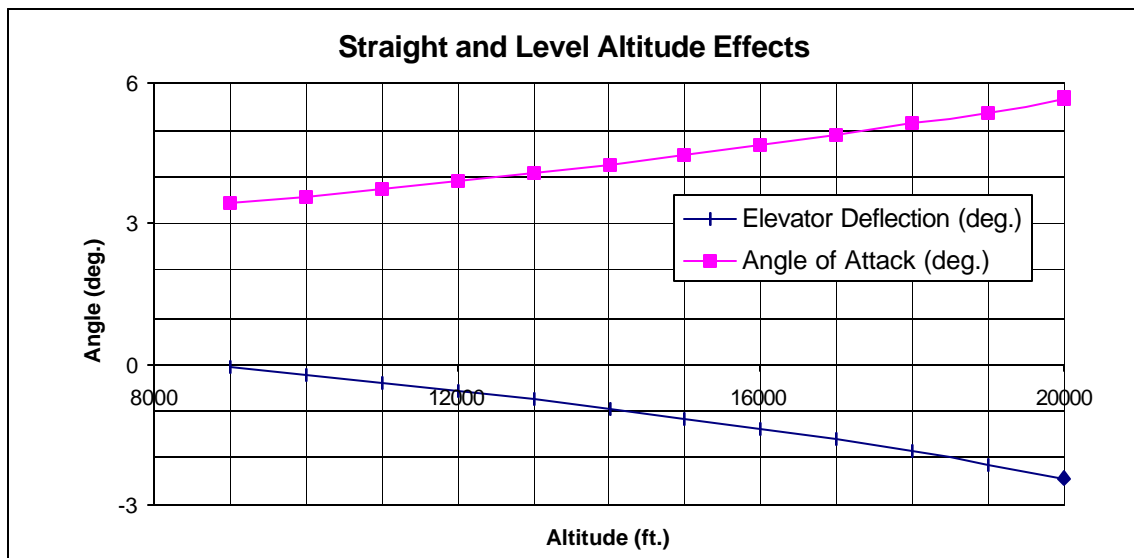


Figure 13. Elevator Control Surface Deflection (δ_e) and Angle of Attack (α) versus Altitude (h)

The control law equations were solved for various altitudes over the applicable envelope. Changing the altitude affects the required thrust of the aircraft. The higher the altitude, the lower the temperature and air density, which lowers the required thrust. Therefore, the only parameters that changed were α , θ , T , and the required δ_e . θ was equal to α at all points. Figure 13 shows the relationship between altitude and the required δ_e and the aircraft angle of attack, α . The required elevator deflection varied up to 2.38° over the range of valid altitudes. A nearly linear relationship was observed, with -0.22° of δ_e required for every 1,000 ft increase in altitude. A similar relationship was observed for α , with a 0.21° increase in α , for every 1,000 ft increase in altitude. The required thrust was also varied over the altitude envelope.

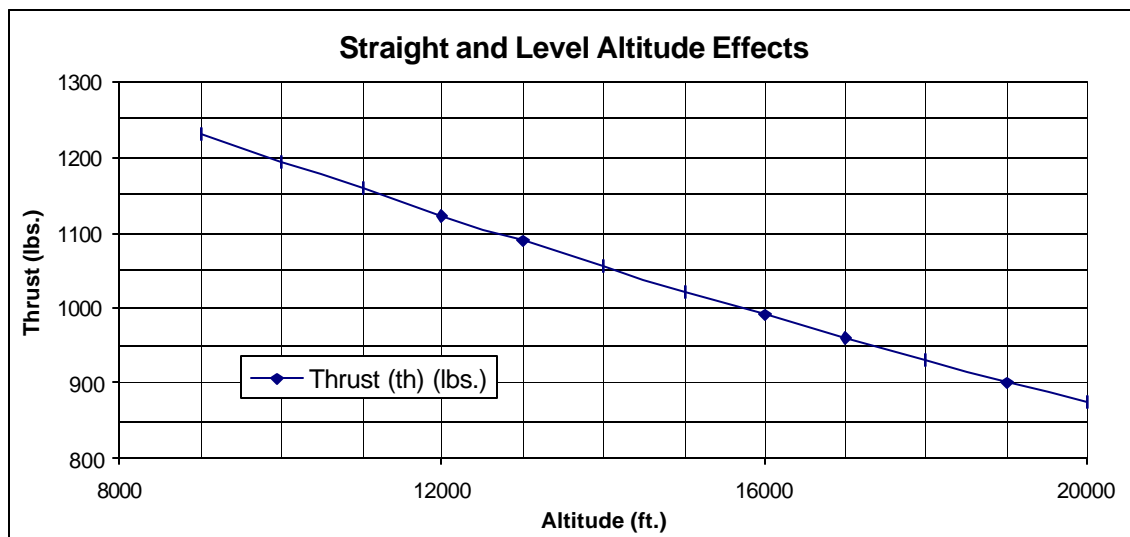


Figure 14. Thrust (T) verses Altitude (h)

The linear relationship between altitude and required thrust is shown in Figure 14. Changing altitude had a moderate effect on the thrust, with a 350 lbs difference between the top and the bottom of the altitude envelope. For each 1,000 ft increase in altitude, 32.4 lbs less of thrust was required to maintain trimmed flight. This result was expected since the lower density at a higher altitude reduces the drag, which reduces the required thrust.

Weight Effect Investigation.

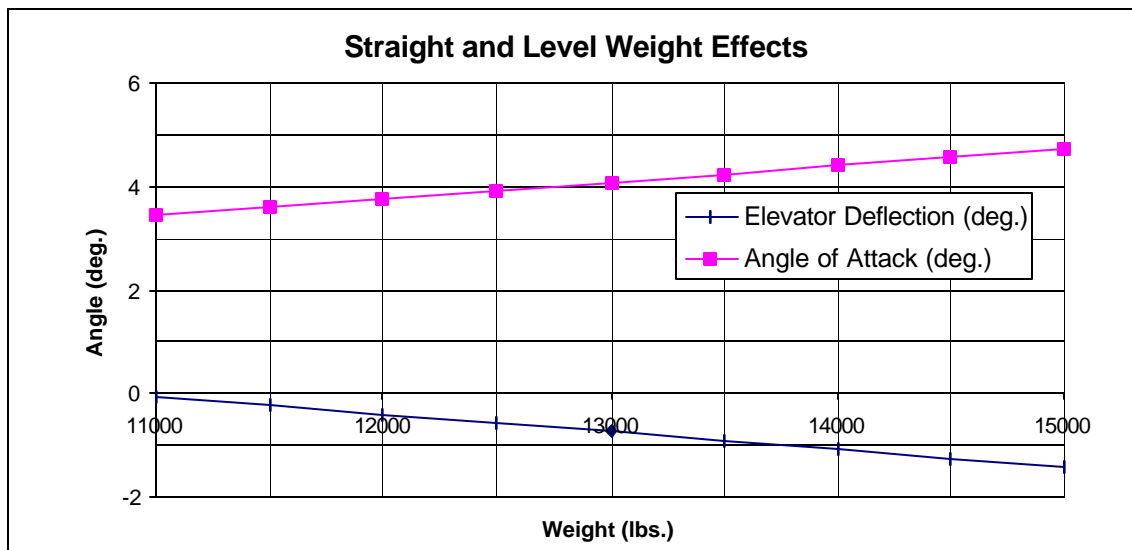


Figure 15. Elevator Control Surface Deflection (δ_e) and Angle of Attack (α) versus Aircraft Weight (W)

After examining the effect of altitude on the trim condition, the aircraft gross weight was varied around the center weight of 13,500 lbs to find the impact on the control settings. The aircraft weight range was chosen between 12,000 and 15,000 lbs. The results are shown in Figure 15. Changing the aircraft weight changed the amount of

lift required, which was directly related to α . The elevator angle was varied by changing α . Therefore, the heavier the aircraft, the more negative δ_e and positive α required for trimmed level flight. The slope of the weight line was greater than for the altitude study: a 1,000 lbs increase in weight requires a 0.34° decrease in the elevator deflection angle. A similar relationship was found in the α , a 1,000 lbs increase in weight requires a 0.32° increase in angle of attack.

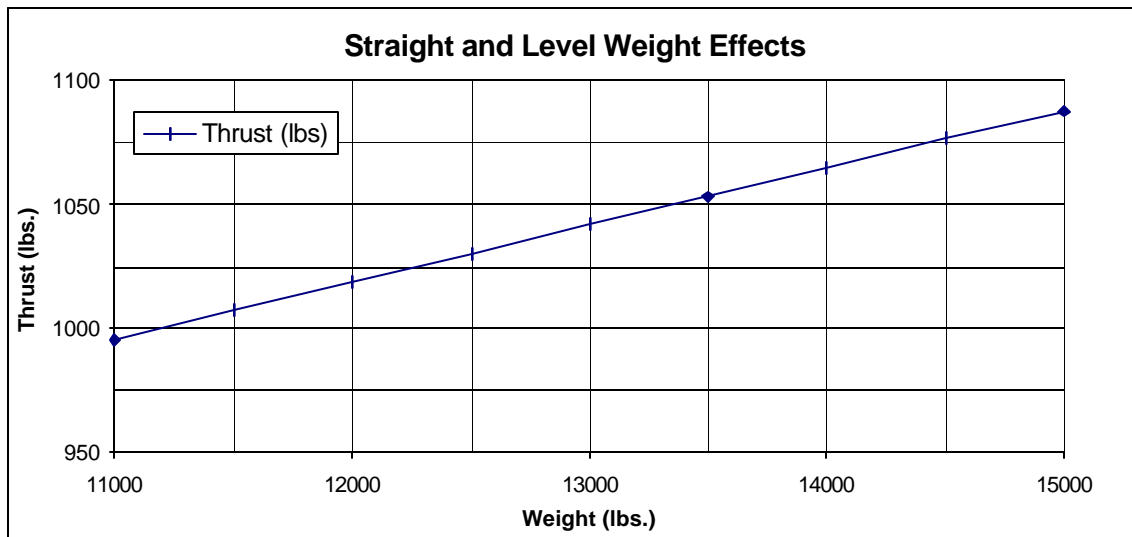


Figure 16. Thrust (T) versus Aircraft Weight (W)

Again a linear relationship was noted for thrust over the weight flight envelope (see Figure 16). Weight changes have a limited impact on the required thrust of the Learjet-25. A 1,000 lbs increase in weight results in only a 23.1 lbs increase in thrust. The variation was caused by the increased weight, which increased the required α to

produce more lift, which increased drag. Now that the effect of changing the aircraft weight is known, changes in velocity are presented.

Velocity Effect Investigation.

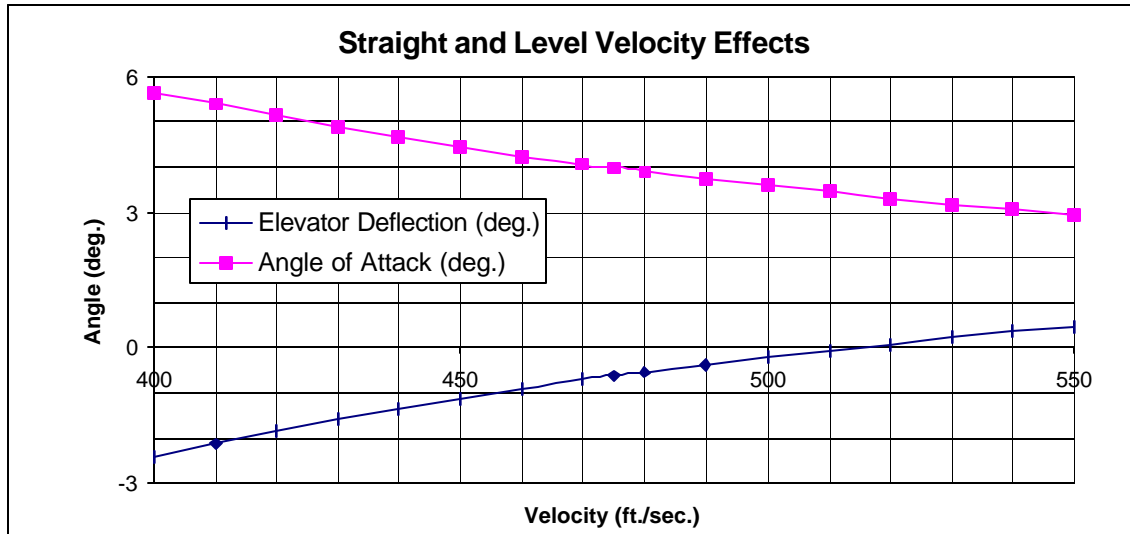


Figure 17. Elevator Control Surface Deflection (δ_e) and Angle of Attack (α) versus Aircraft Velocity (V)

The next steady level flight parameter examined was the affect of a change in velocity from the equilibrium velocity of 450 feet per second (ft/s). The test points were chosen over the assumed valid range for the aircraft derivatives, from 237 KIAS (400 ft/s) to 326 KIAS (550 ft/s). To achieve the velocity change, while maintaining steady flight, the trimmed thrust setting was changed to vary velocity. This resulted in a change in α , and the required δ_e . The rest of the control variables were not affected. The results are shown in Figure 17. Second-order relationships with velocity were seen for both δ_e

and α . As the velocity was changed from 400 ft/s to the upper limit of 550 ft/s, the required δ_e was increased 2.89° and α was decreased 2.73° . Therefore, increasing the airspeed required a smaller negative δ_e to maintain trimmed level flight, with a corresponding decrease in α .

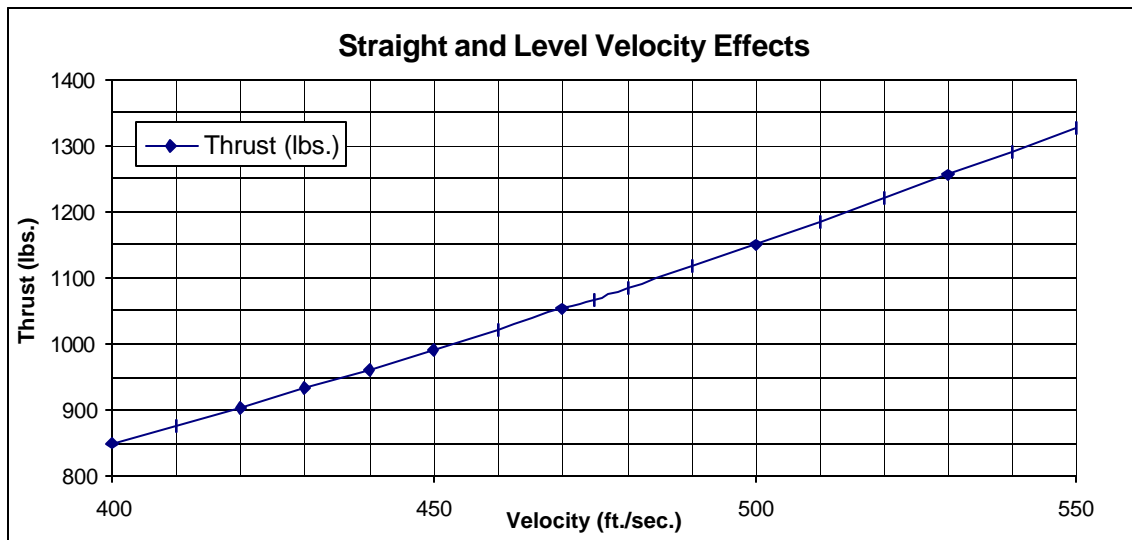


Figure 18. Thrust (T) verses Aircraft Velocity (V)

Changing the velocity from the steady state value had a moderate impact on the required aircraft thrust, as shown in Figure 18. The parameters have a linear relationship with a slope of 3.2 lbs of thrust per ft/s. When increasing the airspeed from the lower limit of 400 ft/s to the upper limit of 550 ft/s, 478 lbs more thrust was required. The result was expected, since higher velocity results in more drag requiring more thrust. The first three parameters affected the longitudinal stability of the aircraft; next a lateral-direction parameter will be presented.

Asymmetrical Thrust Effect Investigation.

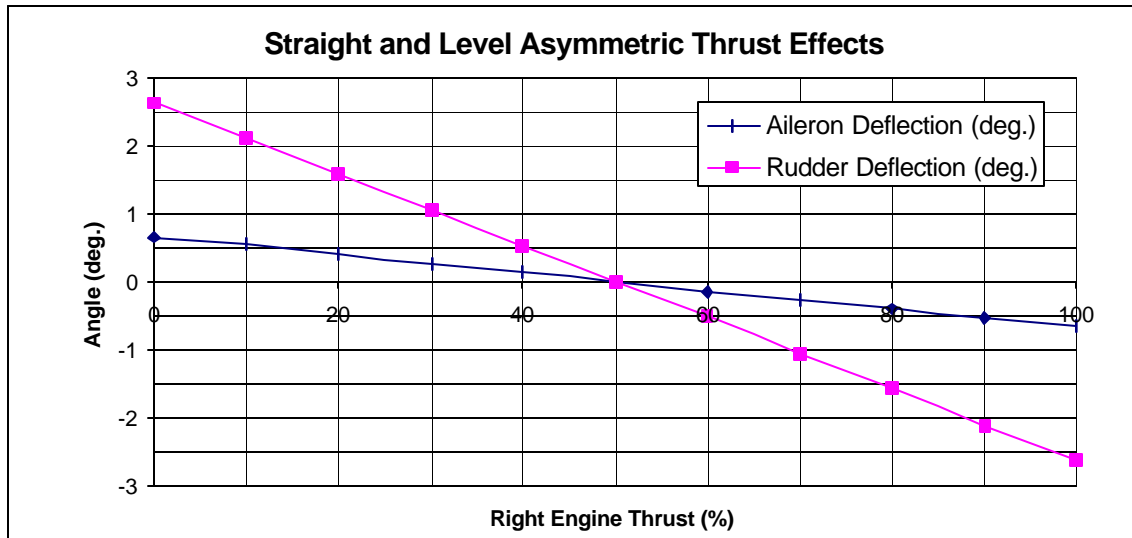


Figure 19. Aileron Surface Deflection (δ_a) and Rudder Surface Deflection (δ_r) versus Percent of Right Engine Thrust

The Learjet has two engines, on each side of the center of gravity. If the thrust from each engine is not the same, roll and yaw moments will be created about the center of gravity. Asymmetrical thrust was examined by calculating the percentage of thrust out of the right engine. An input of 100%, represents all the thrust was from the right engine, with 0% from the left engine. For most calculations in this study it was assumed that 50% of the trust was from each engine. The pitch control variables (δ_e and α) were not changed with a thrust asymmetry since the longitudinal forces and moments remained constant. To maintain steady level flight, with asymmetrical thrust, the aileron (δ_a) and rudder (δ_r) were deflected. Figure 19 reproduces the relationship between asymmetrical thrust and the required lateral control surface deflections. Linear relationships were

observed for both control surfaces. For a one percent increase in thrust from the right engine over the left engine, a 0.01° decrease in δ_a and a 0.05° decrease in δ_r were required. Thus, if 60% of the total thrust was from the right engine (a 10% increase), δ_a must be decreased 0.13° and δ_r decreased 0.53° from the symmetrical test condition. Now that steady level flight has been examined, some other simple trimmed flight maneuvers will be studied.

Trim Conditions 2 and 3 Investigation.

The next aircraft maneuvers examined were straight and steady trimmed climbs and descents. The aircraft was assumed to remain in the same orientation, so the angular rotations and accelerations, $P, Q, R, \dot{P}, \dot{Q}, \dot{R}, \dot{\alpha}, \dot{\beta}, \dot{\gamma}$, and \dot{H} , were all still zero. Initially the maneuver was limited to the longitudinal plane, so that \hat{a}, \hat{f}_v , and H were also zero. A steady change in altitude was achieved by setting the flight path angle, γ , equal to a non-zero value and solving the control law equations for trimmed flight.

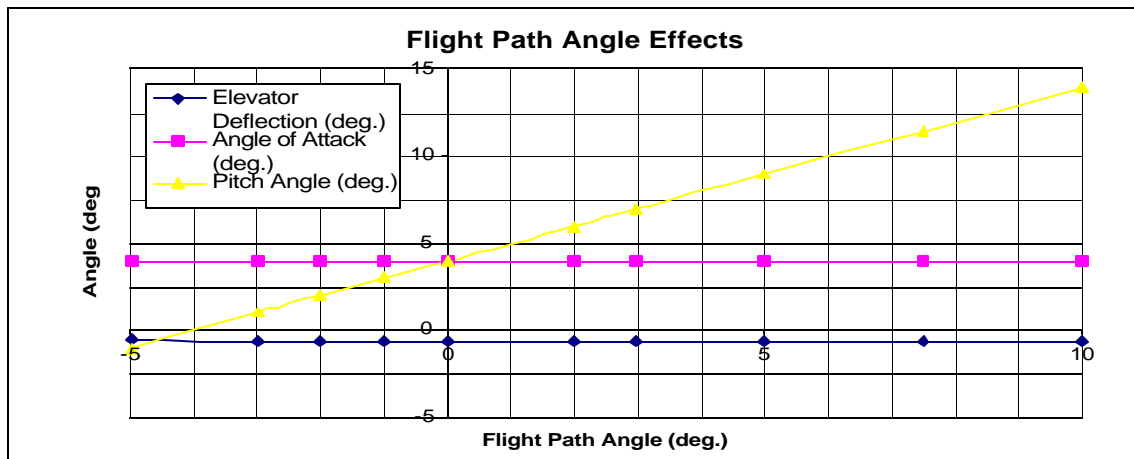


Figure 20. Elevator Surface Deflection (δ_e), Angle of Attack (α) and Pitch Angle (θ) versus Flight Path Angle (γ)

From steady straight and level flight, the aircraft maneuver examined was a change in altitude by a trimmed climb or descent. The input parameter, γ , was varied while the rest of the input parameters were unchanged. The climb angle was varied until the upper and lower limits of the available thrust were found. The required angle of attack and pitch angle were also calculated. The maneuver was limited to the longitudinal plane; therefore δ_a and δ_r remained zero. The graph of θ , δ_e and α are shown in Figure 20. Angle of attack and elevator deflection remain nearly constant for all γ . The pitch angle was linearly related to γ with a 1.0° change in γ resulting in the same change in θ .

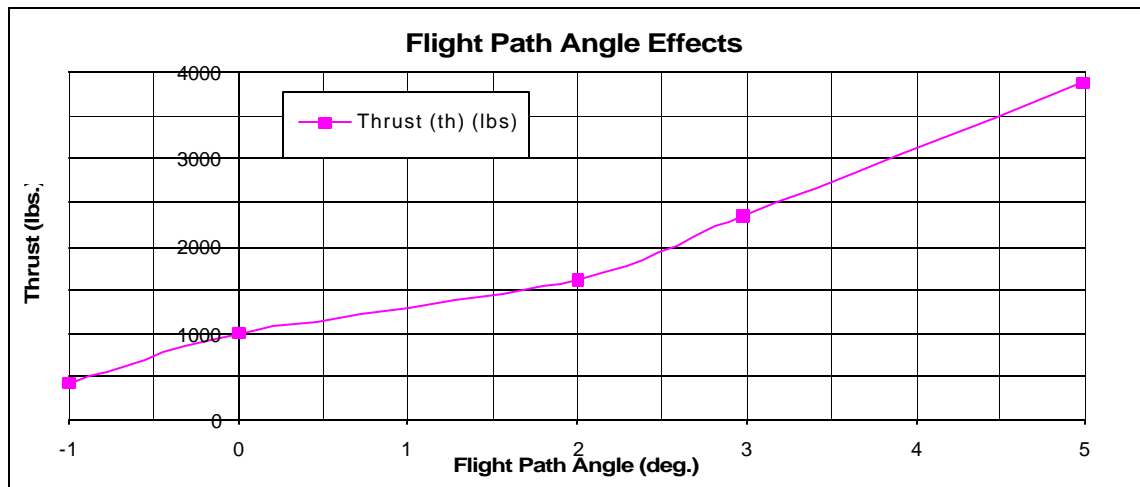


Figure 21. Thrust (T) versus Flight Path Angle (γ)

The rate of climb is directly related to the amount of required thrust. Flight path angle and thrust are shown in Figure 21. Gamma and thrust are a non-linear function of sine and cosine, which flatten out near $\gamma=0^\circ$, and increase as γ increases. Small changes

in flight path angle produce a large change in required thrust, especially the further from level flight. The rate of climb, and associated flight path angle, require more thrust as γ increases. Also for a trimmed descent, little to no thrust is required. The lower limit of γ corresponds to zero thrust required to remain trimmed. Next a lateral-directional trim condition was investigated, during crabbing flight.

Trim Condition 4 Investigation.

Level crabbing flight with a non-zero sideslip angle was examined in trim condition 4. The aircraft was assumed to be in level flight, with a constant heading. The forces and moments were balanced, therefore P , Q , R , \dot{P} , \dot{Q} , \dot{R} , \dot{P}_v , \dot{Q}_v , and \dot{R}_v were all zero. The angles g and H were also set equal to zero. The value of β began at zero and was increased in magnitude in both the positive and negative directions until a limit was reached. Since β was specified, ϕ_v was determined from the outer-loop equations to balance the forces and moments. The Learjet-25 had a $\pm 10^\circ$ β limit, which was the limiting factor in the sideslip investigation. The longitudinal parameters T , α , θ , and δ_e were essentially constant for the entire range of β examined.

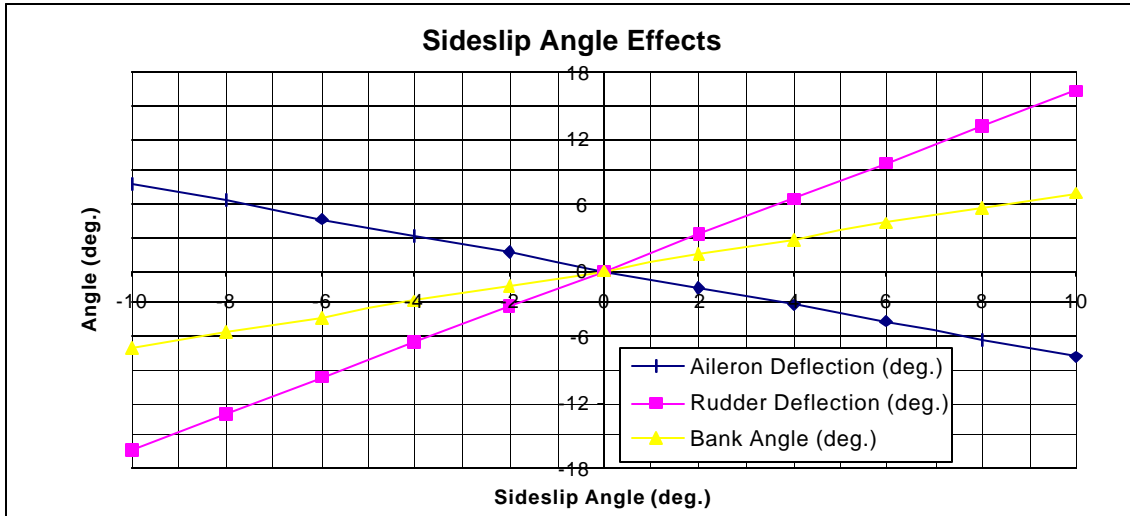


Figure 22. Aileron Surface Deflection (δ_a), Rudder Surface Deflection (δ_r) and Bank Angle (ϕ) versus Sideslip Angle (β)

In straight and level flight, β was varied to the limits, while the rest of the input variables were held constant. The lateral-directional parameters were calculated and plotted in Figure 22. Aileron deflection was inversely proportional to the sideslip angle, with a 0.79° decrease in δ_a for every 1.0° increase in β . Conversely, δ_r increased as β increased, with a 1.63° increase in δ_r for each 1.0° increase in sideslip angle. Finally, bank angle was linearly related to β . A 0.70° increase in ϕ corresponded to a 1.0° increase in β . Next, another lateral-directional trim condition, a steady, level turn, was investigated.

Trim Condition 5 Investigation.

Level turns were investigated by varying bank angle and sideslip angle. The aircraft was assumed to be in level flight with a constantly changing heading, $H = \mathbf{v}_\theta t$, a function of time. The ϕ_v and β were determined by specifying one variable and

calculating the other by the outer-loop equations. The control surface deflections are constant with respect to time. In Figure 23, ϕ_v was specified. For trim condition $\underline{5}$, γ was also set equal to zero. The parameters T , α , θ and δ_e did not change significantly when ϕ_v was varied. The limiting factor was the maximum δ_r . The bank angle was varied both directions until the rudder limit was exceeded.

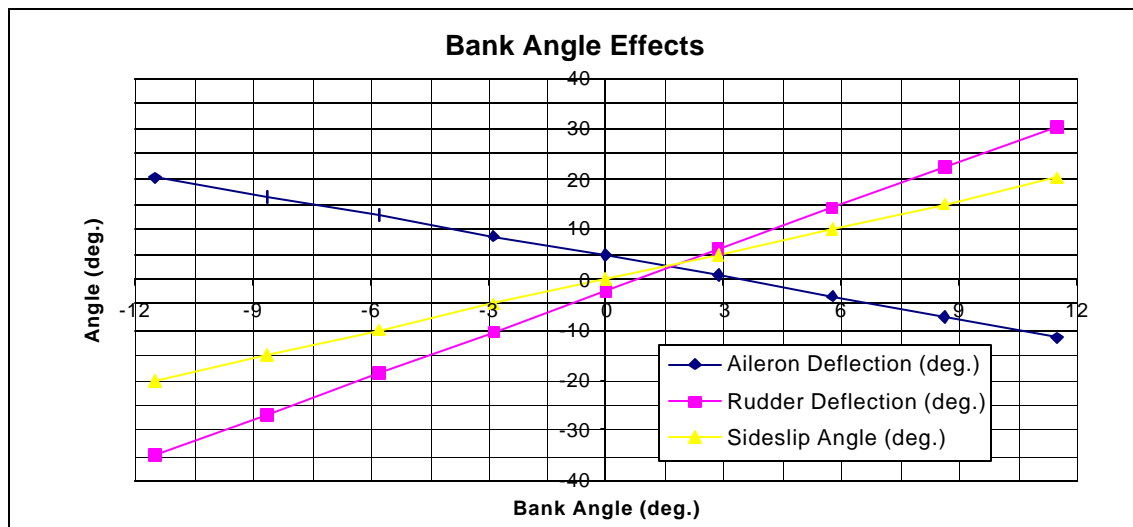


Figure 23. Level Flight Aileron Surface Deflection (δ_a), Rudder Surface Deflection (δ_r) and Sideslip Angle (β) vs. Bank Angle (ϕ_v)

From Figure 23, there was a linear relationship between ϕ_v and δ_a , δ_r , and β . Aileron deflection was inversely proportional to ϕ_v , with a 1.0° increase in bank angle decreasing δ_a by 1.38° . On the other hand, when ϕ_v was increased 1.0° , δ_r increased 2.85° . Finally, the slope of the β per ϕ_v line was $1.75^\circ/^\circ$. Next the more general cases of steady turns were investigated, when the flight path angle was not zero.

Trim Condition 6 Investigation.

For trim condition 6, a turn rate and climb angle were chosen to explore the effect of bank angle on a climbing turn. As in trim condition 5, the heading angle was described by $H = \mathbf{v}_\phi t$. Additionally, γ was defined as a positive angle. As before, ϕ_v was varied until an aircraft parameter limit was reached, and β was calculated from the outer-loop equations. The rudder deflection was still the limiting factor for this case. The pitch angle changed slightly over the ϕ_v range examined, so θ was also plotted.

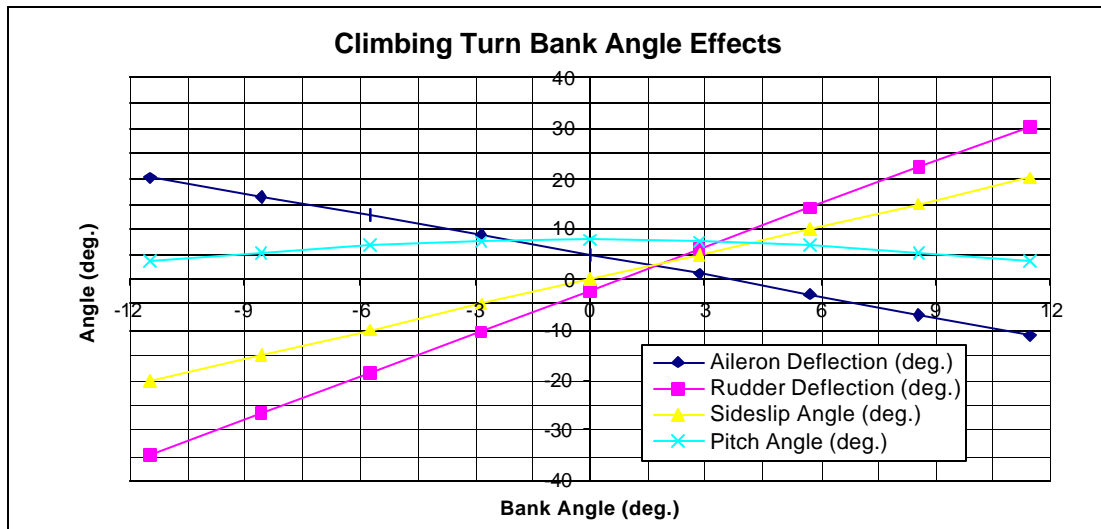


Figure 24. Climbing Flight Aileron Surface Deflection (δ_a), Rudder Surface Deflection (δ_r) and Sideslip Angle (β) vs. Bank Angle (ϕ_v)

The aircraft parameters for trim condition 6 were nearly identical to trim condition 5. The data were plotted in Figure 24. The slope of δ_a/ϕ_v and β/ϕ_v did not change. The slope of δ_r/ϕ_v decreased from $2.85^\circ/^\circ$ to $2.84^\circ/^\circ$ for this case. The pitch angle decreased slightly as the magnitude of ϕ_v increased. The θ began at 7.84° and

decayed to 3.58° at $\phi_v = \pm 11.46^\circ$. Next a descending turn was investigated by restricting γ to negative values. Thrust results were nearly identical to the flight path angle investigation, as expected.

Trim Condition 7 Investigation.

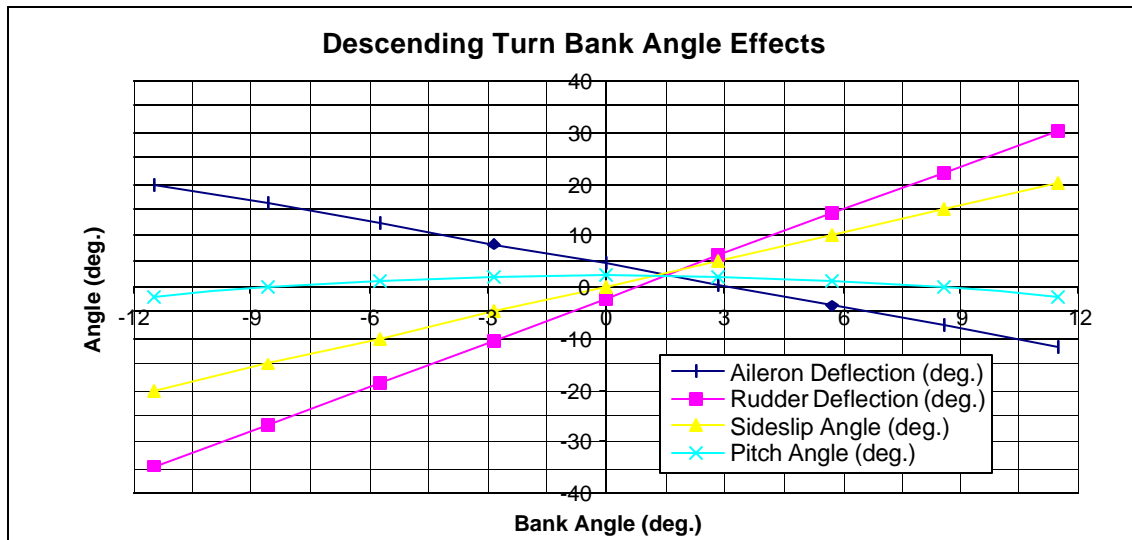


Figure 25. Descending Flight Aileron Surface Deflection (δ_a), Rudder Surface Deflection (δ_r) and Sideslip Angle (β) vs. Bank Angle (ϕ_v)

The next aircraft maneuver investigated was trimmed descending turns. The assumptions and limitations for trim condition 7 are identical to trim condition 6 with one exception: γ was negative. The results are shown in Figure 25. The slopes of all three linear relationships were unchanged from trim condition 6. The primary difference between this case and the previous trim condition was the effect of γ on θ . Lowering the

γ , shifted the θ curve down and flattened the curve, making θ less of a function of γ . The next trim condition examined was the rolling effects during a barrel roll.

Trim Condition $\underline{\delta}$ Investigation.

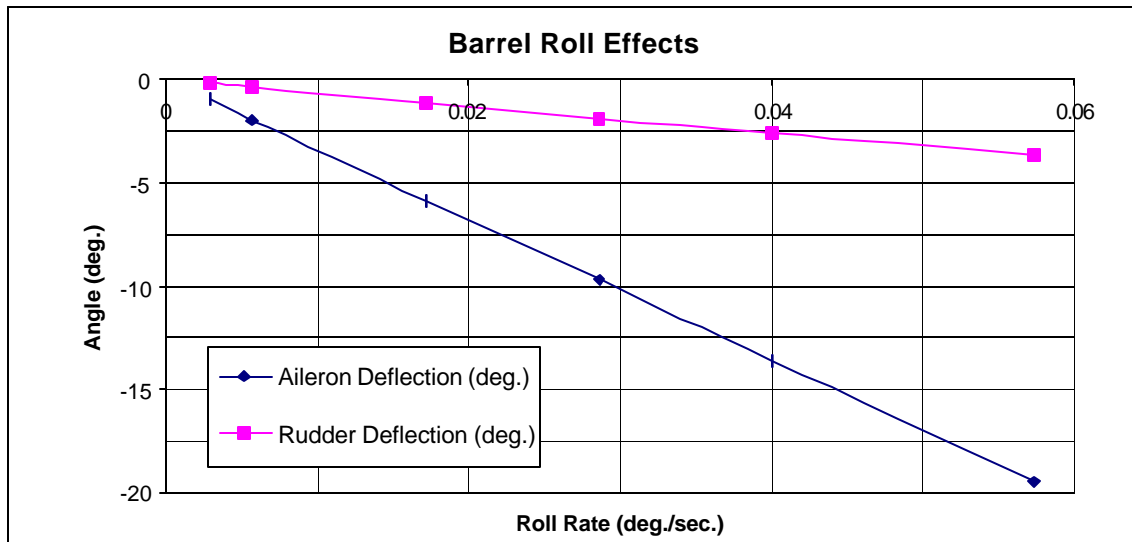


Figure 26. Barrel Roll Aileron Surface Deflection (δ_a) and Rudder Surface Deflection (δ_r) vs. Bank Angle (ϕ_v)

A barrel roll, with constant roll rate about an axis above the x_b -axis, was modeled in trim condition $\underline{\delta}$. The barrel roll was defined as $\beta = H = 0^\circ$ and $\phi_v(t) = \mathbf{v}_{f_v} t$. The flight path angle was also set to a positive number. By restricting β to zero, the radius from the axis of rotation, r_b , was zero. Therefore trim condition $\underline{\delta}$ was the roll rate of the aircraft. To increase r_b , β must be increased to a positive number. The larger β , the larger r_b . Non-zero β was not investigated. The parameters α , θ , T , and δ_e remained constant. The lateral-directional control surface deflections were linear functions of \mathbf{v}_{f_v} .

(see Figure 26). The roll rate-limiting factor was the amount of δ_a available. The influence of roll rate on δ_r was small; a 0.01 deg/s increase in $\dot{\phi}_v$ created a 0.64° decrease in δ_r . Meanwhile, a 0.01 deg/s increase in $\dot{\phi}_v$ produced a 3.39° decrease in δ_a . The Learjet-25 cannot complete a roll. This investigation only examined the trimmed condition to start the roll from wings level. While a complete roll may be mathematically possible, the maneuver was not physically possible with this aircraft model. In the next trim condition, an operationally representative AC-130 gunship orbit was studied.

Trim Condition 9 Investigation.

The first mission representative aircraft maneuver examined was the orbit of the AC-130 gunship. The orbit trajectory was described by a trimmed level steady turn (trim condition 5). The parameters δ_a , δ_r , and β are all functions of ϕ_v . Figure 23 also applies to trim condition 9. For the AC-130 orbit, the aircraft height above the target, orbit radius and bank angle were varied as functions of load factor and weapon depression angle. The velocity was held constant at 450 ft/s. Figure 27 shows the effect on height above the target, and Figure 28 shows the relationship of r_t and ϕ_v to n .

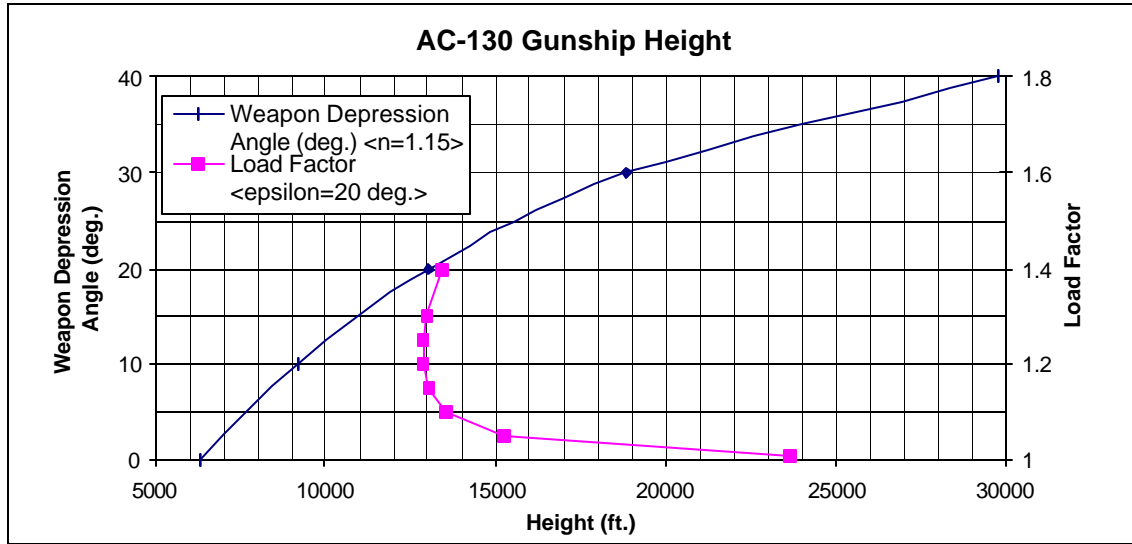


Figure 27. AC-130 Gunship Weapon Depression Angle (ϵ) and Load Factor (n) versus Height (h)

The height of the gunship orbit above the target is a function of weapon depression angle and load factor (see Figure 27). For the weapon depression angle curve, the load factor was fixed at 1.15, which resulted in an orbit radius of 11,083 ft and a bank angle of 30° . As the weapon depression angle asymptotically approached 45° the height above the target approached infinity. For the specified flight condition, the minimum height above the target was 6,294 ft. For the load factor curve, the weapon depression angle was set at 20° , and n was varied from 1.0 to 1.4 (the maximum bank angle). The height approached a minimum at 12,850 ft and increased slightly as n approached 1.4. As the load factor approached 1.0, the height above the target approached infinity. Utilizing the load factor curve, the weapon depression angle curve would move slightly right as load factor increased and dramatically right as n approached 1.0 since $n=1.15$ was near the minimum of the load factor curve.

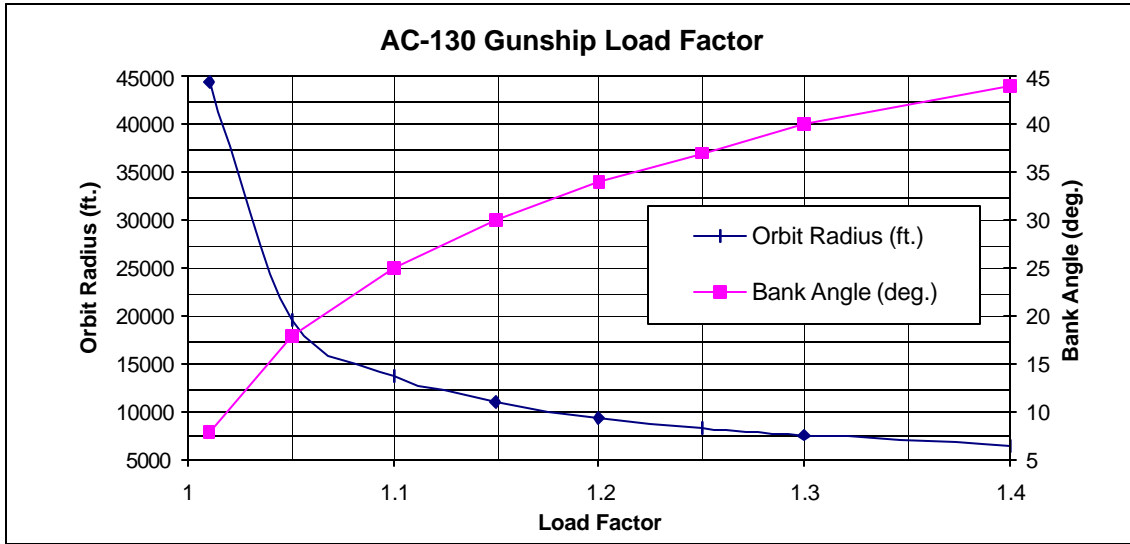


Figure 28. AC-130 Gunship Orbit Bank Angle (ϕ_v) and Radius (r_t) verses Height (h)

The effect of load factor on orbit radius and bank angle is shown in Figure 28.

The orbit radius curve asymptotically approached 5,000 ft as load factor approached the upper limit. Also, as n approached 1.0, the orbit radius approached infinity (as expected since $n=1.0$ is level flight). The bank angle curve approached 0.0° as n approached 1.0. Likewise, at the upper limit as n approached 1.4, ϕ_v approached 45° . Both curves are independent of ϵ and apply to all trim condition 2 flight conditions.

Trim Condition 10 Investigation.

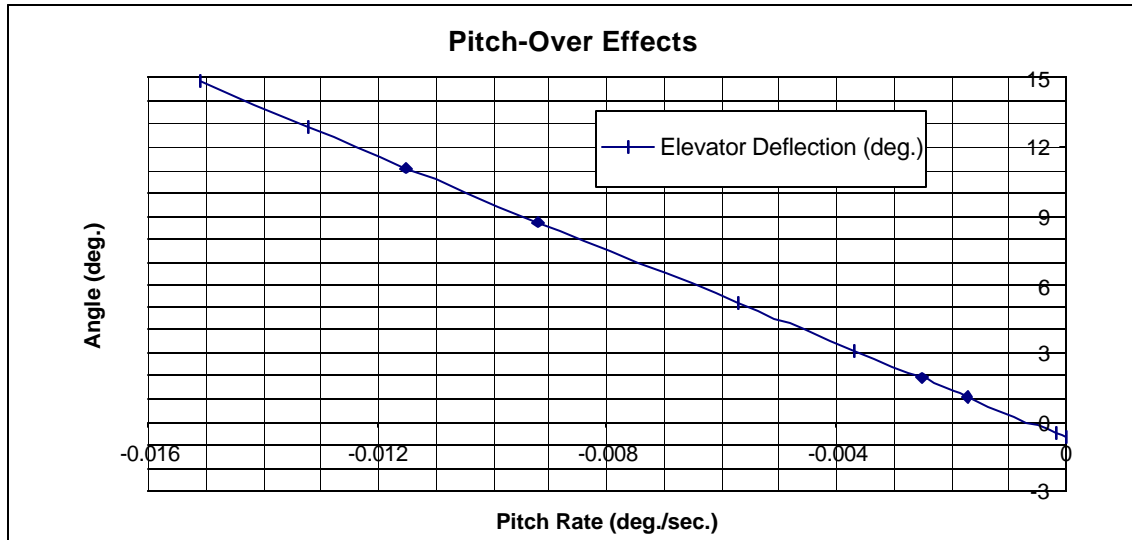


Figure 29. Pitch-Over Elevator Surface Deflection (δ_e) versus Pitch Rate (Q)

The final aircraft maneuver investigated was the trimmed pitch-over. The purpose of trim condition 10 was to create a maneuver where a device mounted to the bottom of the aircraft was pointed at a fixed target below the aircraft. By defining the correct V and \mathbf{v}_ξ , a radius, r_θ , was defined for the trajectory arc. The pitch rate dictates the amount of time the device points at the target. A slower pitch rate produced a longer time on target. The maneuver was defined as level with $\gamma=0^\circ$. Level flight with $\gamma=0^\circ$, produced a constantly changing α . For a slow pitch rate, level flight would not keep the device pointed at a stationary target. The pitch angle varied continuously throughout the maneuver. The maneuver was also limited to the longitudinal plane; therefore all lateral-directional parameters were negligible. The primary parameter of interest for trim

condition 10 was δ_e . The data were plotted in Figure 29. The pitch rate was varied from 0.0 deg/s to the elevator deflection limit 15 deg/s. The elevator control surface deflection was a linear function of the pitch rate. A 0.01 deg/s increase in pitch rate resulted in a 10.27° decrease in the required δ_e .

Summary

Individual trim conditions were investigated in Chapter 4. For straight and level flight, nearly linear relationships were found for δ_e and thrust for both altitude and weight changes. For velocity changes, a linear relationship was found between velocity and the thrust setting. Velocity changes produced a second order relationship with δ_e though. The asymmetric thrust investigation found linear functions for both δ_a and δ_r . Climbs and descents were found to have a direct impact on thrust setting, while a negligible impact on δ_e . δ_a and δ_r were linearly changed by changes in the sideslip angle. For steady turns, a linear relationship was observed between δ_a and δ_r with changes in bank angle. The same relationship was observed between δ_a and δ_r with bank angle as the flight path angle was varied. For a barrel roll, linear relationships were found for both δ_a and δ_r as roll rate was varied. The effects of load factor and weapon depression angle on height above the target were determined for a simulated AC-130 gunship orbit. Also the impacts of bank angle and orbit radius on load factor were plotted. Finally a linear relationship was observed between δ_e and pitch rate for the pitch-over maneuver.

V. Stability Derivative Sensitivity Analysis

Overview

In Chapter 2, the point mass model was developed to provide a basis for the control laws for the trajectory of the aircraft. The outer-loop equations were found from the nonlinear equations of motion and applied to the actual Learjet-25 parameters. In Chapter 3, the outer-loop equation outputs were used with the transformation matrices and the remainder of the equations of motion to find the control surface deflections required to achieve the desired flight trajectory and orientation. In Chapter 4, the equations developed in the previous two chapters were used to simulate selected flight trajectories. By choosing the correct input states, the required control surface deflections for the desired flight path were found. The impacts of variations in the stability derivatives are investigated in Chapter 5 to determine which parameters require the most accuracy. Each stability derivative is varied $\pm 40\%$ to determine the change in predicted control surface deflection value. Control surface deflection changes greater than 1.0° from the original value are deemed significant. The sensitivity analysis was used to identify the most critical parameters and possible sources of error. Finally, in Chapter 6 the theoretical values tested using the Learjet-25 in flight tests are compared to the theoretical calculations.

Sensitivity Analysis

The stability derivatives were divided into two groups: longitudinal stability derivatives and lateral-directional stability derivatives. The longitudinal stability

derivatives were: C_{D_0} , C_{D_a} , C_{D_q} , C_{L_0} , C_{L_a} , C_{L_q} , $C_{L_{\dot{\alpha}}}$, C_{m_0} , C_{m_a} , C_{m_q} , and $C_{m_{\dot{\alpha}}}$.

The longitudinal stability derivatives were investigated in two trimmed flight conditions

(straight and level flight and climbing flight). The lateral-directional stability derivatives

were: $C_{y_{\dot{\alpha}}}$, C_{y_p} , C_{y_r} , $C_{y_{\dot{\alpha}\alpha}}$, $C_{y_{\dot{\alpha}r}}$, $C_{l_{\dot{\alpha}}}$, C_{l_p} , C_{l_r} , $C_{l_{\dot{\alpha}\alpha}}$, $C_{l_{\dot{\alpha}r}}$, $C_{n_{\dot{\alpha}}}$, C_{n_p} , C_{n_r} , $C_{n_{\dot{\alpha}\alpha}}$, and

$C_{n_{\dot{\alpha}r}}$. The lateral-directional stability derivatives were investigated in two trimmed flight

conditions (crabbing flight and steady-turn flight). Straight and level flight did not

produce any forces in the lateral-directional axes, and no change in the control surface

deflections.

Longitudinal Stability Derivative Sensitivity.

The longitudinal stability derivatives sensitivities were found for two cases. Each

stability derivative was varied $\pm 40\%$ from the original value to estimate the effect of

errors in the stability derivatives on the predicted control surface deflections. Stability

derivatives calculated from wind tunnel data may have up to a 40% error (9: Class 2)

from the actual aircraft value. By finding the most critical stability derivatives, the

required level of accuracy in the estimation of the stability derivatives was determined.

Straight and Level Flight.

The first longitudinal trim condition investigated was straight and level flight.

The Matlab® routine developed in Chapter 4 (see Appendix B) was used to determine the

sensitivity of each output to derivative change. Changes in control surface deflection

greater than $\pm 1.0^\circ$ when the original value was varied $\pm 40\%$ were noted.

The following stability derivatives: C_{D_0} , C_{D_a} , C_{D_q} , C_{L_0} , C_{L_q} , $C_{L_{\dot{\alpha}}}$, C_{m_0} , C_{m_q} ,

and $C_{m_{\dot{\alpha}}}$ had negligible effects on control surface deflection values when varied $\pm 40\%$.

Increasing C_{L_a} did not produce a change in δ_e larger than 1.0° , but decreasing C_{L_a} 23.8% from the original value resulted in a 1.0° decrease in δ_e . Varying C_{m_a} by $\pm 31\%$ resulted in a change of 1.0° from the original value of δ_e . Overall, in straight and level flight errors in the longitudinal stability derivatives did not produce a significant change in the control surface deflection values.

Climbing Flight.

Next, the longitudinal stability derivative sensitivities were investigated in trimmed climbing flight. The same stability derivatives were evaluated with the same criteria as straight and level longitudinal flight. Changes in all the longitudinal stability derivatives except C_{m_a} had a negligible effect on the required control surface deflections. As in straight and level flight, a $\pm 31\%$ error in C_{m_a} produced a 1.0° change in δ_e .

Overall, the errors in the longitudinal stability derivatives did not produce large errors in the control surface deflection values. The accuracy of the longitudinal values was also well known (reference 10). Therefore the longitudinal predictions were very accurate and should match the flight test results. In Chapter 6 the accuracy of the longitudinal predictions compare very well to the measured flight test data.

Lateral-Directional Stability Derivative Sensitivity.

The lateral-directional stability derivatives sensitivities were found for two cases, crabbing and steady turn flight. Each stability derivative was varied $\pm 40\%$ from the original value to estimate the effect of errors in the stability derivatives on the predicted control surface deflections.

Crabbing Flight.

The first lateral-directional trim condition investigated was flight in a crabbing condition with a constant sideslip angle. Each lateral-directional stability derivative was again varied $\pm 40\%$ from the original values. Changes of $\pm 40\%$ in the following stability derivatives changed the control surface deflections less than one degree: $C_{y_{\dot{a}}}$, C_{y_p} , C_{y_r} , $C_{y_{\dot{\alpha}}}$, $C_{y_{\dot{\alpha}r}}$, C_{l_p} , C_{l_r} , C_{n_p} , C_{n_r} , and $C_{n_{\dot{\alpha}}}$.

Small dihedral stability derivative, $C_{l_{\dot{a}}}$, errors produced large changes in the predicted control surface deflection values. A change of 17.1% of $C_{l_{\dot{a}}}$ in either direction from the original value created a 1.0° change in δ_a , while a variation in $C_{l_{\dot{a}}}$ did not change δ_r . Changes in the aileron control power derivative, $C_{l_{\dot{\alpha}}}$, produced an insignificant change in δ_r , but a 18.7% decrease from the original value of $C_{l_{\dot{\alpha}}}$ or a 30% increase in $C_{l_{\dot{\alpha}}}$ changed δ_a 1.0° from the original value. Similarly, varying the roll coupling stability derivative, $C_{l_{\dot{\alpha}r}}$, had a negligible effect on the δ_r predictions. However, changing $C_{l_{\dot{\alpha}r}} \pm 28.6\%$ resulted in a 1.0° change in δ_a . Small errors in the weathercock stability derivative, $C_{n_{\dot{a}}}$, had large ramifications on the predicted lateral-directional control surface deflections. A $\pm 9.3\%$ change in $C_{n_{\dot{a}}}$ resulted in a 1.0° change in δ_r . Also, a $\pm 28.6\%$ change in $C_{n_{\dot{a}}}$ produced the same error in δ_a . Finally, errors in the rudder control power derivative, $C_{n_{\dot{\alpha}r}}$, produced significant errors in the lateral-directional control surface deflection values. While an increase in $C_{n_{\dot{\alpha}r}}$ did not effect δ_a , a 22.1%

decrease in $C_{n_{\dot{a}}}$ from the original value changed δ_a by 1.0° . Rudder surface deflection was even more sensitive to changes in $C_{n_{\dot{a}}}$. A 10.4% increase and an 8.6% decrease in $C_{n_{\dot{a}}}$ from the original value produced a 1.0° change in δ_r .

Overall the lateral-directional stability derivatives were more sensitive to errors in crabbing flight than the longitudinal stability derivatives in any flight condition. Errors in lateral-directional stability derivative values (reference 10), also contributed to the errors in the lateral-directional axes predictions. Therefore the open-loop equations will not predict required control surface deflection for crabbing flight as accurately.

Steady Turn Flight.

The other lateral-directional trim condition investigated was flight in a steady turn with a constant bank angle. Each lateral-directional stability derivative was again varied $\pm 40\%$ from the original values. Changes of $\pm 40\%$ in the following stability derivatives had a negligible effect on the control surface deflection values: C_{y_p} , C_{y_r} , $C_{y_{\dot{a}}}$, $C_{y_{\dot{r}}}$, C_{l_p} , C_{l_r} , C_{n_p} , and C_{n_r} .

As in the crabbing flight case, the same stability derivatives were most sensitive to errors in a steady turn. A decrease of 11.0% in the original value of $C_{y_{\dot{a}}}$ resulted in an increase in δ_a of 1.0° . Likewise, only a 4.8% decrease or a 5.6% increase in $C_{y_{\dot{a}}}$ produced an unacceptable error in δ_r . While errors in $C_{l_{\dot{a}}}$ did not effect δ_r , an error of $\pm 6.9\%$ resulted in a 1.0° change in δ_a . The predicted δ_r was not influenced by errors in either $C_{l_{\dot{a}}}$ or $C_{l_{\dot{r}}}$. Aileron deflection was significantly impacted by errors in the roll coefficient control surface derivatives though. An 11.1% decrease or a 14.6% increase in

$C_{l_{ia}}$ resulted in a significant change in δ_a . Also, a $\pm 15.6\%$ change in $C_{l_{ir}}$ produced a similar error in δ_a . Small weathercock stability derivative, C_{n_a} , errors produced large errors in the control surface deflection predictions. A $\pm 5.0\%$ variation in C_{n_a} changed δ_r by a degree, and if the error increased to $\pm 15.4\%$, δ_a exceeded the error limit. Finally, only a $\pm 4.6\%$ error in $C_{n_{ir}}$ resulted in a change of 1.0° in δ_r . As the error in $C_{n_{ir}}$ was decreased to -13.2% or increased to 18.6% of the original value of $C_{n_{ir}}$, the same error was seen in δ_a .

As seen in the crabbing flight case, in a steady turn errors in the stability derivatives produced unacceptably large errors in the lateral-directional control surface deflection predictions. The higher uncertainty in the lateral-directional derivative values also compounded higher inaccuracy in the predictions when compared to the longitudinal cases. The higher errors predicted for the lateral-directional cases was observed in flight test (see Chapter 6).

Summary

The stability derivatives were prioritized from the most to the least sensitive to change in control surface deflection values. The results are listed in Table 2 below. The percentage change that produced a 1.0° error in control surface deflection dictates the level of accuracy required. The stability derivatives were estimated in the flight test program to improve the prediction accuracy (reference 10). The derivatives in Table 2 were the focus of the aeromodelling tests to attempt to achieve the required level of accuracy. In flight test, all longitudinal stability derivatives were within acceptable

tolerances. The accuracy of the new C_{1_b} and $C_{l_{ia}}$ estimates did not reach the accuracy required for the lateral-directional stability derivatives. Therefore, the lateral-directional control surface deflection predictions cannot be guaranteed to be within $\pm 1.0^\circ$ of the actual value. This discrepancy was observed in flight test (see Chapter 6).

The prioritized sensitivities of the stability derivatives follow. A “+” percentage is an increase from the original value, while a “-“ is a percent decrease.

Table 2. Stability Derivative Sensitivity Analysis

<u>STABILITY DERIVATIVE</u>	<u>d_e</u>	<u>d_a</u>	<u>d_r</u>	<u>CONDITION</u>
Rudder Control Power ($C_{n_{\dot{r}}}$)	>±40%	-13.2% / +18.6%	±4.6%	Banked Flight
Side-force Coefficient due to Sideslip ($C_{y_{\dot{a}}}$)	>±40%	-11.0%	-4.8% / +5.6%	Banked Flight
Weathercock Stability ($C_{n_{\dot{a}}}$)	>±40%	±15.4%	±5.0%	Banked Flight
Dihedral Stability ($C_{l_{\dot{a}}}$)	>±40%	±6.9%	>±40%	Banked Flight
Rudder Control Power ($C_{n_{\dot{r}}}$)	>±40%	-22.1%	-8.6% / +10.4%	Crabbing Flight
Weathercock Stability ($C_{n_{\dot{a}}}$)	>±40%	±28.6%	±9.3%	Crabbing Flight
Aileron Control Power ($C_{l_{\dot{a}\dot{a}}}$)	>±40%	-11.1% / +14.6%	>±40%	Banked Flight
Roll Moment Coefficient due to Rudder Deflection ($C_{l_{\dot{r}}}$)	>±40%	±15.6%	>±40%	Banked Flight
Dihedral Stability ($C_{l_{\dot{a}}}$)	>±40%	±17.1%	>±40%	Crabbing Flight
Aileron Control Power ($C_{l_{\dot{a}\dot{a}}}$)	>±40%	-18.7% / +30.0%	>±40%	Crabbing Flight
Lift-Curve Slope ($C_{L_{\dot{a}}}$)	-23.8%	>±40%	>±40%	Straight and Level Flight
Roll Moment Coefficient due to Rudder Deflection ($C_{l_{\dot{r}}}$)	>±40%	±28.6%	>±40%	Crabbing Flight
Pitch Coefficient due to Angle of Attack ($C_{m_{\dot{\alpha}}}$)	±31.0%	>±40%	>±40%	Straight and Level / Climbing Flight

VI. Flight Test Results

Overview

In Chapter 2, the point mass model was developed to provide a basis for the control laws for the trajectory of the aircraft. The outer-loop equations were found from the nonlinear equations of motion and applied to the actual Learjet-25 parameters. In Chapter 3, the outer-loop equation outputs were used with the transformation matrices and the remainder of the equations of motion to find the control surface deflections required to achieve the desired flight trajectory and orientation. In Chapter 4, the equations developed in the previous two chapters were used to simulate selected flight trajectories. By choosing the correct input states, the required control surface deflections for the desired flight path were found. The impacts of variations in the stability derivatives were investigated in Chapter 5 to determine which parameters require the most accuracy. Finally, in Chapter 6 the theoretical values tested using the Learjet-25 in flight tests are compared to the theoretical calculations. The aeromodel for the Learjet-25 was estimated from flight test to improve the stability derivatives. Selected trajectories from the previous chapter were also selected for verification in flight test. The results of the flight test were compared to the predicted results to determine the accuracy of the model.

Aeromodel Data

Veridian originally provided the aerodynamic model for the Learjet-25. The original values were used in the Matlab® to calculate the estimated control surface

deflections. The uncertainties in the provided stability derivatives could produce errors larger than 1.0° in the predictions. Therefore, in the flight test program the aeromodel parameters were estimated to produce improved values for the stability derivatives (reference 10).

After stable data were collected at each trim flight test point, control surface deflection doublets were entered into the aircraft. Programmed test input was automatically input for each of \ddot{a}_e , \ddot{a}_a and \ddot{a}_r and the aircraft response recorded. Using the response at each test point, the stability derivatives were estimated using Parameter Estimation software provided by TPS. Average stability derivative values were found for both Regime 1 and Regime 2. The effect of altitude, Mach number and cg location were also investigated for each stability derivative (reference 10). In general, the changes in stability derivatives were negligible within each regime. The improved stability derivatives were then re-inserted into the Matlab® routine and the control surface deflections re-calculated. The improved stability derivative values were used throughout the study and are listed in Table 2. The improved stability derivative predictions were compared to the flight test data in the remainder of this chapter.

Flight Test Data

Selected trim flight conditions examined in Chapter 4, were verified in flight on the Learjet-25 and compared to the theoretical predictions. Trim conditions 1, 2, 3, 4, 5, and 10 were investigated in the flight test program. Most of the longitudinal results (trim conditions 1, 2, and 3) matched the theory very closely, while lateral-directional flight conditions (trim conditions 1, 4, and 5) had more errors and did not match the predictions as well. Each condition investigated during the flight test program is now examined.

The flight test envelope was divided into three flight regimes to study the differences between low, middle and high-speed results. The three regimes were chosen to investigate the effects of atmospheric compressibility and the non-linear regions of the flight envelope. The middle regime, Regime 1, was defined as 190 KIAS to 250 KIAS (approximately 400 to 550 ft/s). Low speed, Regime 2, was defined as the stall speed (dependent on aircraft weight, but around 120 KIAS) to 190 KIAS. The high-speed regime, Regime 3, was from 250 KIAS to the maximum aircraft airspeed (310 KIAS or about 650 ft/s). Flight test in high-speed regime was not completed due to time constraints in the test program.

The Learjet-25 had a variable stabilator (moving horizontal tail) that changed the flying characteristics of the airplane as the stabilator position was changed. Stabilator position was a function of airspeed to maintain trimmed flight. Within each regime, the stabilator position was held constant, but each regime had a different trimmed stabilator position. Therefore, the trimmed aircraft variables and stability derivatives changed between regimes. Exact comparisons between regimes are not valid.

Straight and Level Flight Test.

The majority of the flight test program was used to examine trim condition 1, and all the associated flight effects in straight and level flight. Four flight conditions were examined within trim condition 1: altitude effect, velocity effect, weight effect and asymmetrical thrust effect. Each flight condition will now be detailed.

Altitude Effects.

First the effect of altitude change was investigated by selecting straight and level test points between 9,000 and 20,000 feet mean sea level (MSL). The effect of weight and velocity were isolated to the greatest extent possible by flying each test point with the same aircraft configuration at each altitude in the test band. The results are shown in Figure 30 through Figure 33.

The altitude effect on the flight test parameters was compared to the predictions. The results were very scattered with little correlation. Therefore the data were further separated into three aircraft velocity bands within each flight regime. The flight test results in Regime 1 generally matched the predicted values, while the Regime 2 flight test data were biased from the predicted curves.

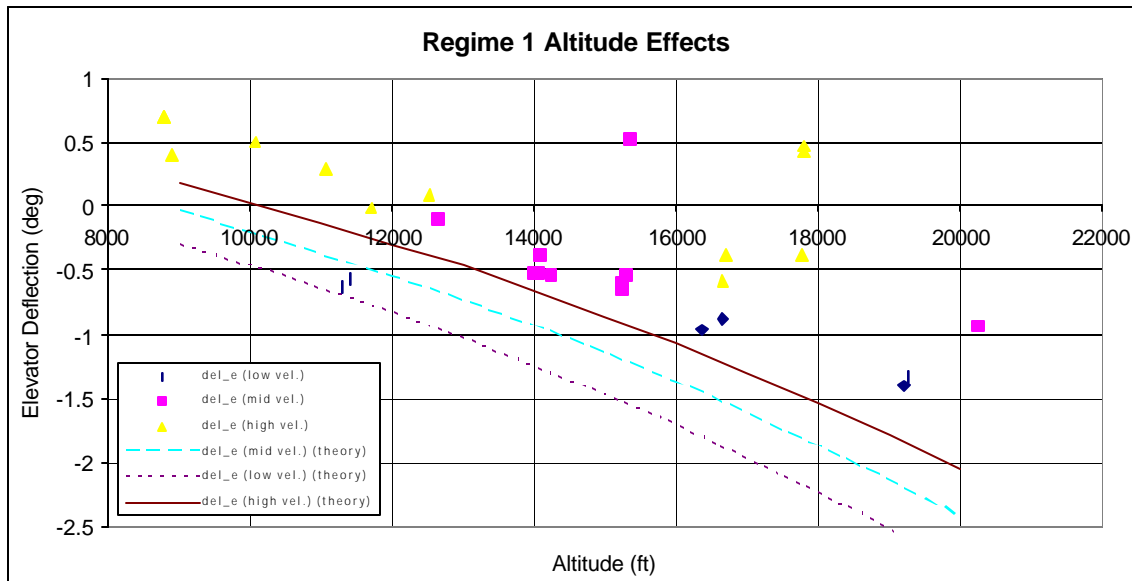


Figure 30. Regime 1 Elevator Deflection (δ_e) vs. Altitude (h) Effect

Figure 30 shows the \ddot{a}_e test data in Regime 1 with an overlay of the predicted \ddot{a}_e for three true airspeed values. The low speed region ($V = 460$ ft/s) described a much more shallow curve than theory predicted. The middle speed region ($V = 475$ ft/s) matched the prediction with a $+0.2^\circ$ bias for all altitudes. The high speed ($V = 490$ ft/s) test points matched the predicted curve, with about the same $+0.2^\circ$ bias, but was more scattered than the mid-speed data. Overall the flight test data matched the predicted data with a small amount of variation.

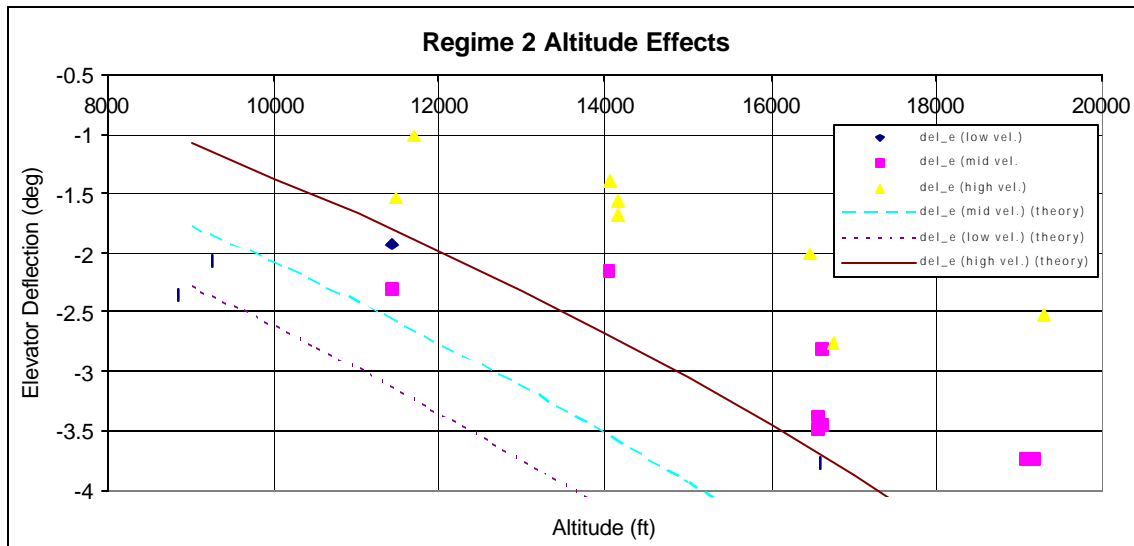


Figure 31. Regime 2 Elevator Deflection (δ_e) vs. Altitude (h) Effect

In Regime 2 the flight test data differed from the predicted curve by almost $+1.0^\circ$ on average for all three velocity bands (see Figure 31). The flight test data were also more scattered than in Regime 1. Overall the data in Regime 2 shows the same general trend as the predicted curves, but the correlation was not strong. The altitude effect on \ddot{a}_e was very small, and was masked by other factors, especially small changes in airspeed.

The \ddot{a}_a and \ddot{a}_r were predicted to be zero in trimmed flight. Small values of \ddot{a}_a and \ddot{a}_r were measured in flight. These deviations result from the impossibility to be perfectly trimmed with no lateral-directional inputs during actual flight test. There were no significant values of \ddot{a}_a and \ddot{a}_r in any of the longitudinal axes investigations data points.

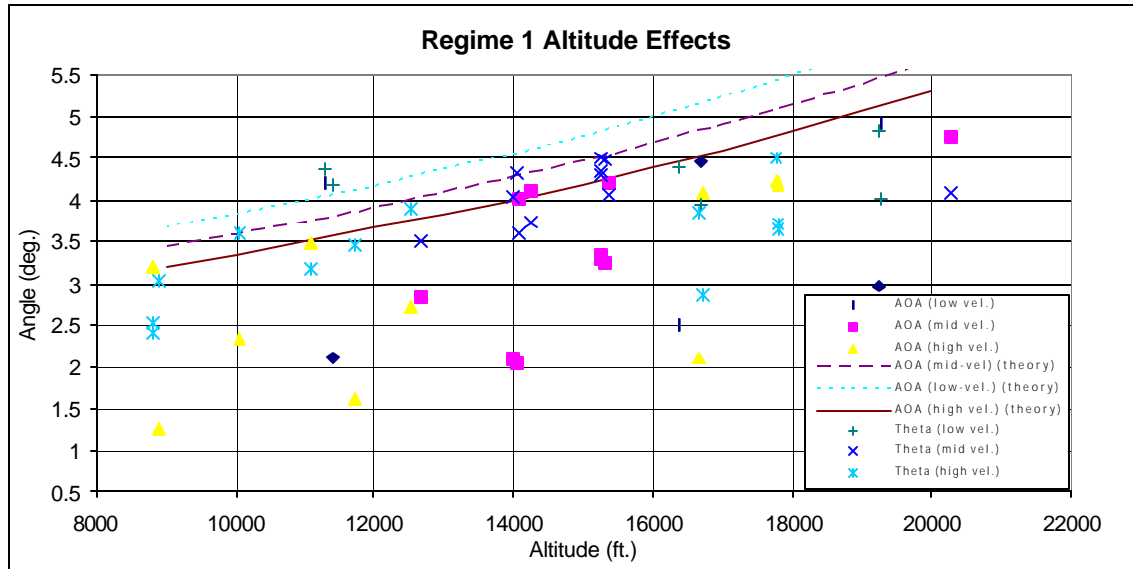


Figure 32. Regime 1 Angle of Attack (α) and Pitch Angle (θ) vs. Altitude (h)

Effect

The altitude effect on α and θ was also not very strong. Figure 32 show the plot of flight test data in Regime 1 for α and θ respectively, with the predictions shown for the same three true airspeed bands. The data in all three bands were characterized by a lot of scatter in the flight test data. All data were within 2° of the predicted curves. The θ values were closer to the predicted curves and did not have as much scatter as α .

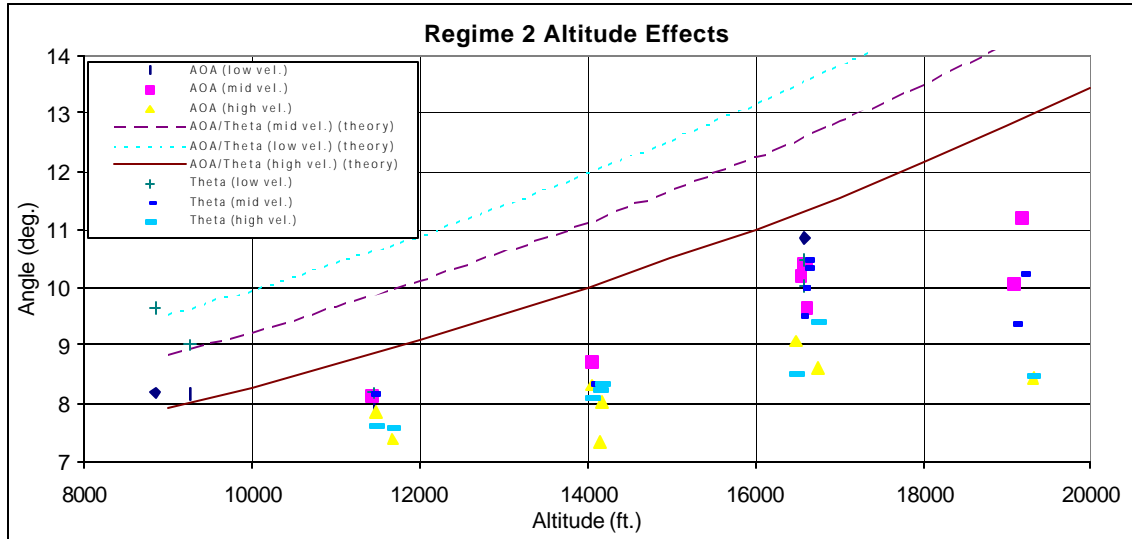


Figure 33. Regime 2 Angle of Attack (α) and Pitch Angle (θ) vs. Altitude (h) Effect

In Regime 2, the data were again scattered, increasing in error as the altitude increased (see Figures 33). The flight test data were also biased -2° to -3° from the predicted value curves. Also the α values were more scattered than the θ values at each altitude.

Overall, the altitude effect on the elevator surface deflections was very small. The data points were scattered by other flight parameter effects and the predicted trends were difficult to match to the model predictions. The effect of altitude variations does not have a significant impact on the resultant errors.

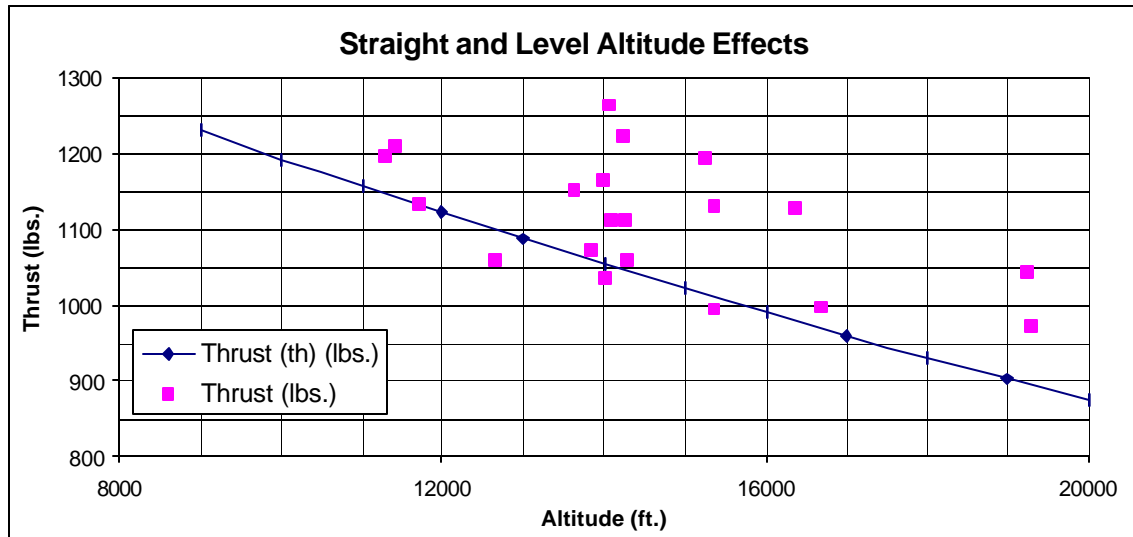


Figure 34. Thrust (T) vs. Altitude (h) Effect

In general, more thrust was measured compared to the predicted curve (see Figure 34). The flight test data follows the same general trend as the predicted curve. The majority of the flight test data are within 100 lbs of the predicted curve. The bias in the data is likely due to the simplified thrust model used to calculate the flight test thrust. The thrust was calculated from the engine pressure ratio and the known area of the nozzle. A more robust aircraft thrust measurement should improve the results. Also the open-loop equations assume the thrust is two point forces acting at the estimated center of the nozzle exit plane. This simplification also likely increases the error in the thrust prediction.

Weight Effects.

Next the effect of changing the aircraft weight and cg was compared to the predictions. Since cg was a linear function of the Learjet-25 weight for all test points, the

control surface deflections were plotted as a function of weight. Figure 35 shows the combined results for Regime 1 and Regime 2.

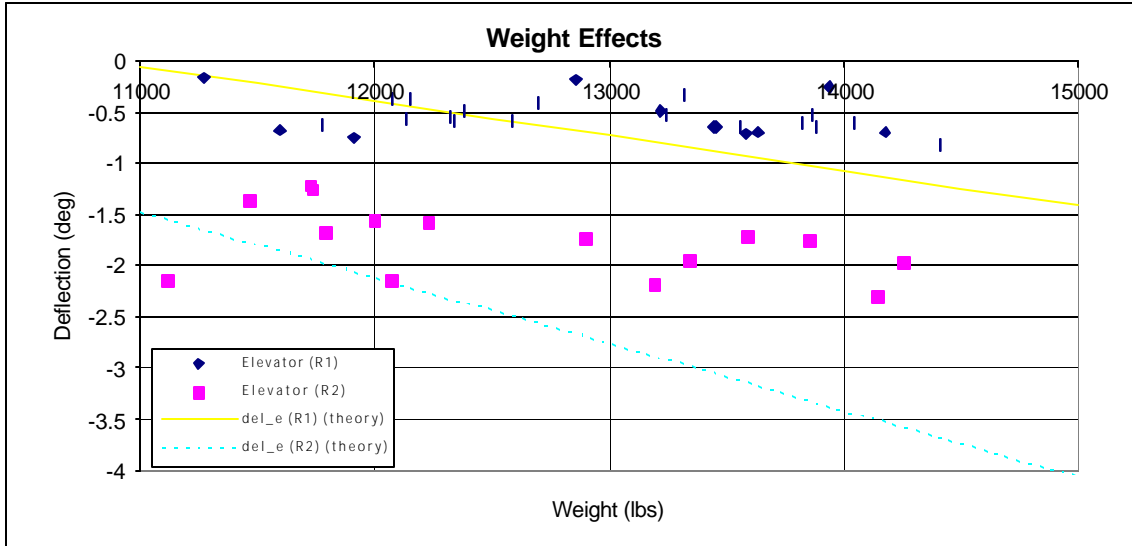


Figure 35. Elevator Deflection (δ_e) vs. Weight (W) Effect

For Regime 1 the flight test results were almost all within $\pm 0.5^\circ$ of the theoretical prediction. However, the flight test results did not show a significant relationship between \ddot{a}_e and variations in weight; actual \ddot{a}_e was essentially constant. According to theory, a 3,000-pound increase in weight would produce a 1.0° decrease in \ddot{a}_e in Regime 1, but this was not observed during flight test.

In Regime 2 the data were more scattered and also did not match the predicted trend. The Regime 2 flight test results were on average about 1.0° higher than the predicted value. Again the flight test \ddot{a}_e were nearly constant for all weights in the test envelope. Theoretically, a 1,500-pound increase in weight would produce a 1.0° decrease

in \ddot{a}_e in Regime 2. Overall, the impact of aircraft weight did not have a measurable effect on the \ddot{a}_e value from flight test data. Theoretically the impact was expected to be small, but not as small as the actual test data indicated. The significant difference between Regime 1 and Regime 2 \ddot{a}_e were the result of a change in trimmed stabilator position.

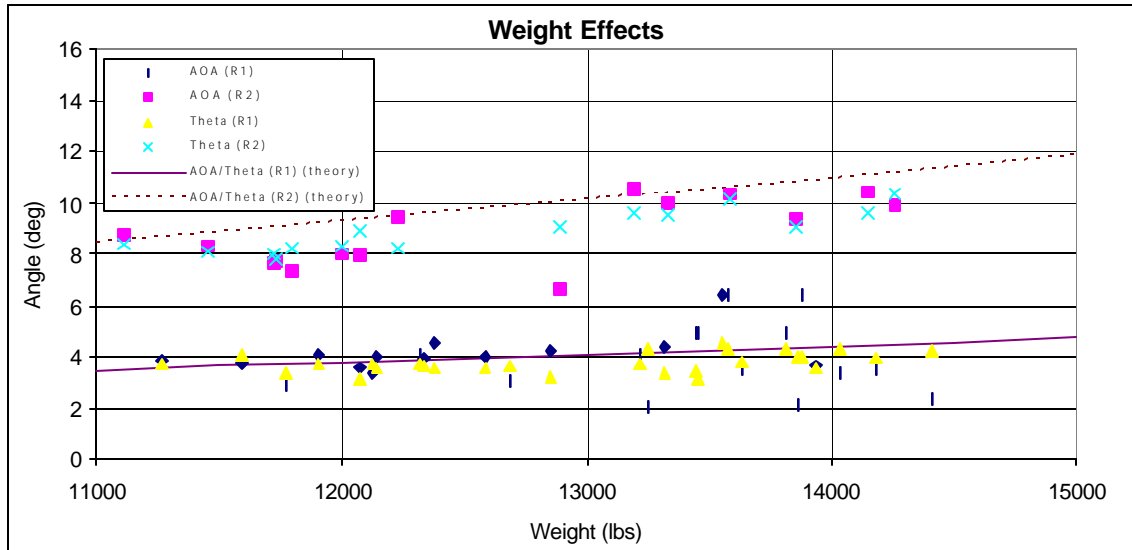


Figure 36. Angle of Attack (α) and Pitch Angle (θ) vs. Weight (W) Effect

The plot of α and θ verses weight is shown in Figure 36. Both Regime 1 and Regime 2 are shown on the plot. For Regime 1, the flight test data are scattered within 2° of the predicted curve, with all the θ data points within 1° of the expected values. The α values were directly affected by the airspeed at which the test point was flown. A 10 ft/s change in true airspeed resulted in an average 0.5° to 1.5° change in α . The α and θ values were more constant than the predicted curve. The accuracy of the in-flight α and θ measurements contributed to the scatter in the data. The α measurement varied $\pm 1.0^\circ$

to 2° , and the θ measurement varied up to $\pm 1.0^\circ$. Therefore, the weight effect on these flight parameters was not as large as expected. The accuracy of the α measurement may also have been less than for θ . In the aeromodeling investigation a lag was found in the α and β measurements (reference 10).

In Regime 1 the flight test data were consistently 1° to 2° lower than the predicted values. The flight test data showed the same scatter in Regime 2 as in Regime 1, with θ nearly linear around the average value and α scattered more about the average value. The larger discrepancy for α and θ in Regime 2 may be due to the fact that the equations were developed for Regime 1, and small aerodynamic non-linearities and the changed position of the stabilator could cause an error in the predictions.

The method weight was measured is another source of error in the weight flight test data. The aircraft weight was displayed in the cockpit, but was not directly input into the data bus messages recorded for the flight. Veridian developed a routine that set the aircraft weight at the start of the flight and decremented the weight at a set rate according to time in flight. It was assumed that the fuel burn rate was constant, which may not have been an accurate assumption. Periodically the weight was updated from the cockpit display to improve the recorded weight value. The first few flights the decrement rate was varied to try to match the aircraft display in the cockpit. The weight measurement error would increase the scatter in the flight test data.

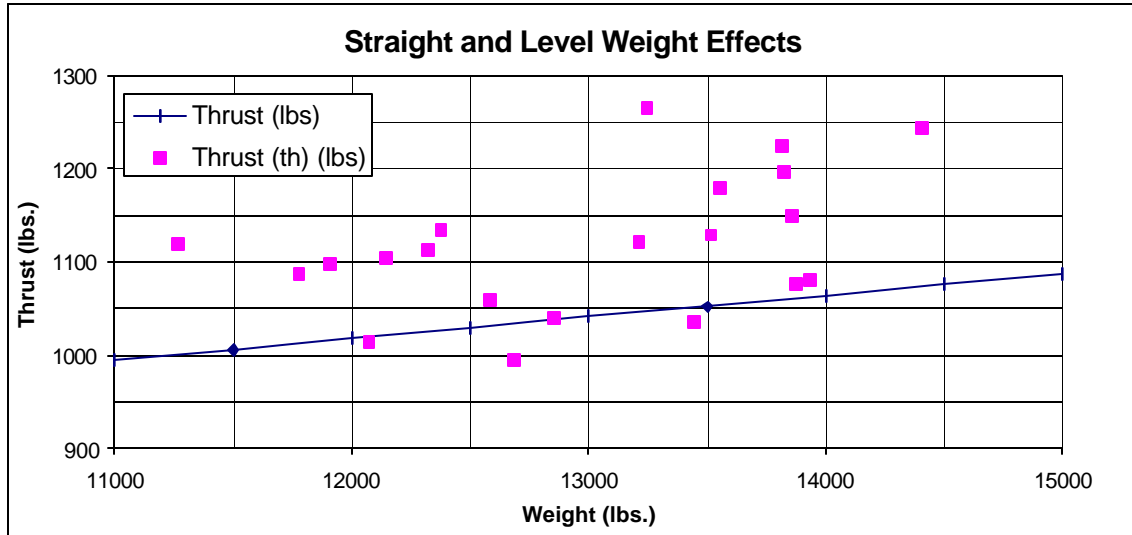


Figure 37. Thrust (T) vs. Weight (W) Effect

The weight verses thrust plot (see Figure 37) has even more scatter than the previous thrust plot (Figures 34). The increased scatter was likely due to the method weight was measured (discussed above), and the same errors used to calculate thrust. The data has the same upward trend as weight increased, and the predicted values are lower than the measured data as previously observed. Next the effect of varying the velocity was investigated.

Velocity Effects.

The effect of changing the aircraft velocity in flight test is compared to the theoretical prediction. The results for both Regime 1 and Regime 2 are plotted in Figure 38. The flight test data followed the same trend predicted by the outer-loop equations, with a small bias. The data bias was more pronounced in Regime 2.

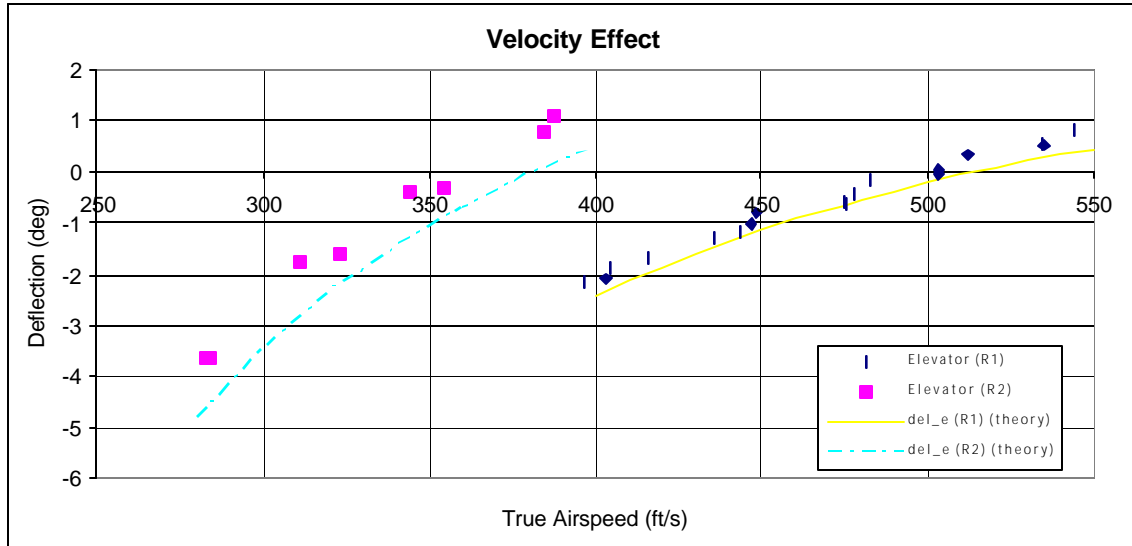


Figure 38. Elevator Deflection (δ_e) vs. Velocity (V) Effect

In Regime 1, the flight test \ddot{a}_e was consistently higher than the theoretical prediction by approximately 0.25° . All flight test data were within 0.0° to 0.5° of the model prediction. The effect of velocity was not affected by small changes in the aircraft weight and test point altitude. Therefore, the effect of velocity on \ddot{a}_e had the greatest impact on the straight and level flight results. In Regime 2 the flight test \ddot{a}_e was consistently 0.75° higher than the predicted curve. The flight test data were tightly grouped around the average trend-line and showed the strong effect that a change in velocity created in the \ddot{a}_e value. The larger difference between predicted and flight test data in Regime 2 was similar to the results as discussed above for the altitude effect.

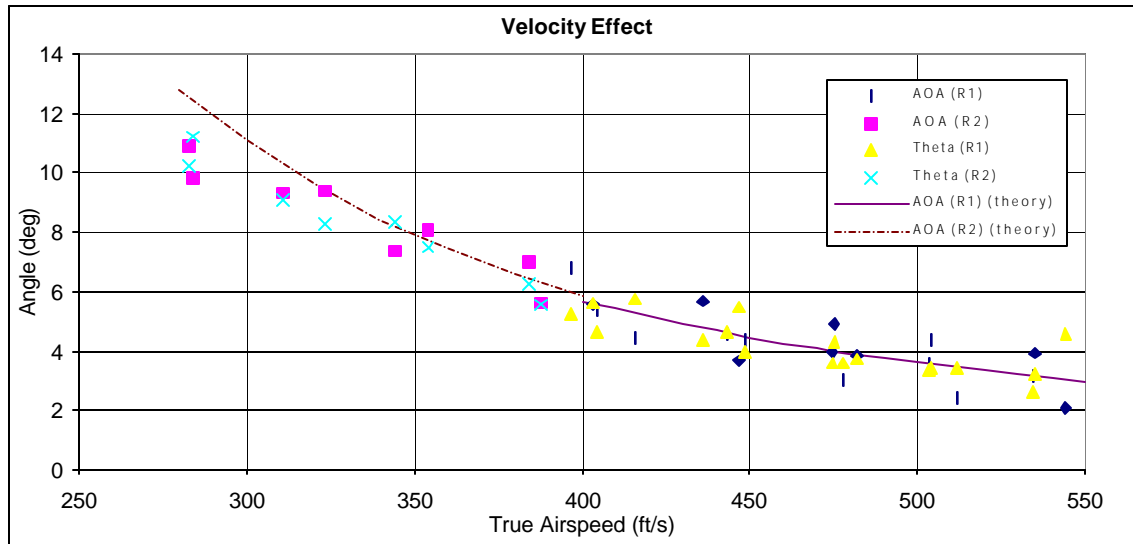


Figure 39. Angle of Attack (α) and Pitch Angle (θ) vs. Velocity (V) Effect

The α and θ results for both regimes are plotted in Figure 39. The flight test results matched the theoretical predictions within $\pm 1.0^\circ$, except at the slowest airspeeds in Regime 2. The data were in a nearly continuous curve across both regimes. There was a slight jump in the theoretical curve between Regime 1 and Regime 2 of less than 0.2° . Again there was more scatter in the α flight test results than in the θ values. The α and θ flight test data matched the model very closely. The velocity effect dominated and the data were scattered by the other factors.

Overall, there was a strong correlation between changes in true airspeed and \ddot{a}_e . The correlation was also seen in α and θ with velocity changes. Velocity measurement accuracy was one of the key indicators of \ddot{a}_e prediction accuracy.

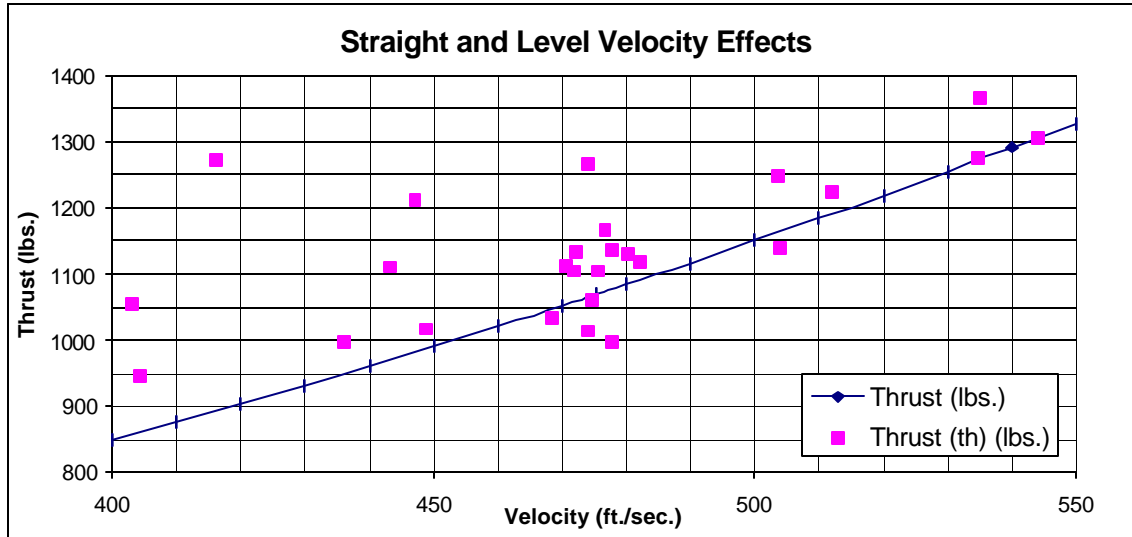


Figure 40. Thrust (T) vs. Velocity (V) Effect

The thrust measurements as a function of velocity are shown in Figure 40. The flight test data had the same general trend as the predicted curve, but again results were biased up about 100 lbs. The same problems experienced in the altitude investigation apply to the velocity effect on thrust.

Longitudinal Maneuvers, Straight and Level Flight Summary.

Overall, the effect of α produced a larger change in the measured \ddot{a}_e than the change in aircraft weight (and corresponding cg). The weight effect was masked by the changes in α from the predicted values. Airspeed also had a large effect on \ddot{a}_e measurements in flight. The scatter in the data, especially in Regime 2, could be explained by the variances in the α and V at each test point from the ideal condition used for the model calculation. When the identical flight condition parameters were used in the model the predicted values closely matched the flight test data.

The test point set-up had a major impact on variations between the flight test data and the theoretical predictions. The flight test velocity had the largest impact on changes in the \ddot{a}_e values. Small variations in test point velocity produced a large change in \ddot{a}_e values. The effect of weight variations was less significant, and the effect of changing altitude was very small. The test set-up variations in β and flight path angle from the specified test conditions were generally less than $\pm 1.0^\circ$ for all test points and did not significantly impact the results. The bank angle varied up to $\pm 8.0^\circ$ from the specified test conditions. Often there was a small roll rate ($\pm 0.5^\circ/\text{sec}$) that was not observed in flight, but impacted the flight test data. The ϕ measurement also had the largest oscillations about the steady-state value, up to a $\pm 1.0^\circ$. The combined errors in ϕ values had a significant impact on the lateral-directional results. Combining variations resulted in a composite change in the control surface deflection value, which accounts for some of the scatter seen in the flight test data. The thrust flight data has the same general trends as predicted by the model. There was a consistent upward bias in the flight test data from the expected curve though.

Asymmetrical Thrust Effects.

The final trim condition 1 flight condition examined was asymmetric thrust. Thrust from one of the two engines was progressively reduced and thrust on the other engine was progressively increased while keeping the wings level and the airspeed within the required tolerance. Data were collected at each asymmetric thrust setting. The data were plotted as the percentage of total thrust from the right engine.

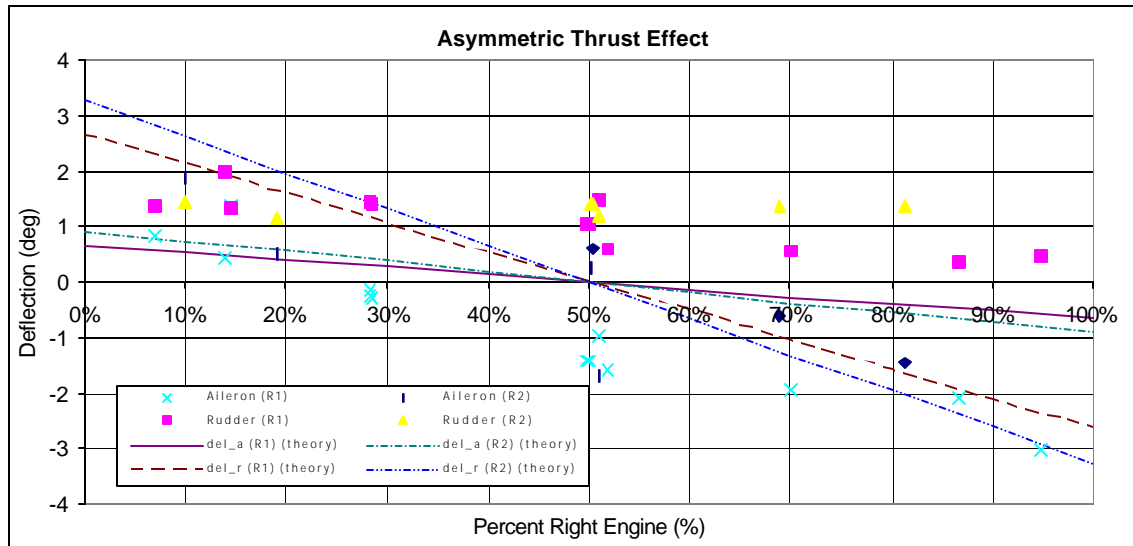


Figure 41. Aileron (δ_a) and Rudder (δ_r) Surface Deflection vs. Asymmetric Thrust (T) Effect

Limited data were collected, especially in Regime 2. The data were very scattered, and did not match the predicted values very closely for lateral-directional control surface deflection values. Figure 41 shows the \ddot{a}_r and \ddot{a}_a values from flight test compared to the predicted theoretical values for both regimes. The theory predicted a larger asymmetric thrust influence on \ddot{a}_r (slope -0.5° per 10% change in asymmetric thrust, versus less than 0.1° per 10% for the averaged values of the flight test data in Regime 1). The \ddot{a}_r results were about the same in Regime 2. The \ddot{a}_a results showed the opposite trend result. The theory predicted about a -0.1° change per 10% change in asymmetric thrust, while the averaged flight test data had a slope of about -0.5° per 10% change in asymmetric thrust. The data had a lot of noise and stable points were difficult to achieve in asymmetrical conditions. The ϕ measurements also had a lot of noise and

were accurate to within only a degree or two of the averaged value at most test points. These errors may account for the inaccuracies between the flight test results and the theoretical predictions.

The \ddot{a}_e values were compared to the theoretical predictions. Theoretically the \ddot{a}_e was constant for all asymmetric thrust test points. In Regime 1, all \ddot{a}_e values were within $\pm 0.3^\circ$ of the theoretical value. If the four data points with large changes in ϕ were discarded, the average flight test data \ddot{a}_e was -0.03° from the theoretical \ddot{a}_e and all flight test points were within $\pm 1.0^\circ$ of the predicted value. In Regime 2 the flight data \ddot{a}_e value was biased -1.0° with very little scatter in the data.

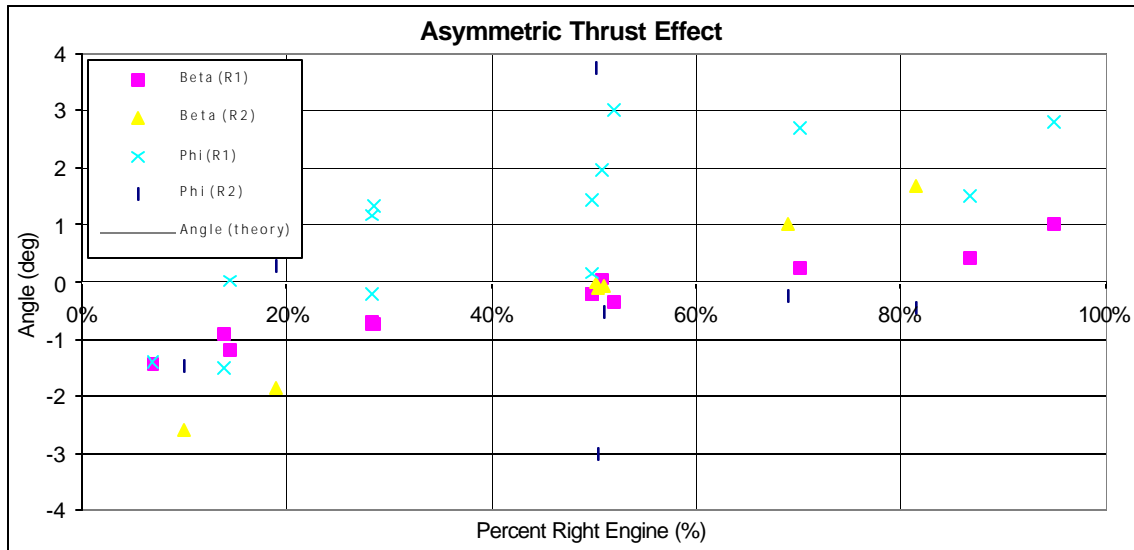


Figure 42. Sideslip (β) and Bank Angle (ϕ) vs. Asymmetric Thrust (T) Effect

The lateral-directional control surface deflection errors also were increased because the test points were not in perfect trim condition in most cases. Figure 42 shows

the plot of $\hat{\alpha}$ and ϕ , respectively, for each test point. The theoretical values for the ϕ were expected to be 0.0° because the maneuver was designed for wings level flight. Flight test points were not perfectly trimmed to wings level, straight flight, so this plot is a measure of the error due to non-ideal flight test conditions. The errors in ϕ were all less than $\pm 4.0^\circ$. The offsets from trim would also contribute to the errors in lateral-directional control surface deflections. The ϕ errors were largest for the points around 50% asymmetric T, which correspond to the largest errors on the control surface deflection plots (Figure 42). Also the ϕ errors tended to be more negative as asymmetric thrust approached 0%, and more positive as asymmetric thrust approached 100%. This was also observed in the $\ddot{\alpha}_a$ and $\ddot{\alpha}_r$ values at the extreme asymmetrical thrust conditions.

Lateral-Directional Maneuvers, Straight and Level Flight Summary.

The lateral-directional stability derivatives had a much larger uncertainty than the longitudinal stability derivatives. This lateral-directional stability derivative uncertainty contributed to variations in model control surface deflections as indicated by the sensitivity analysis. The most critical stability derivatives ($C_{n_{d_r}}$, C_{y_b} , C_{n_b} , and C_{l_b}) created a large error for a small variation. Finally, a bias was observed in both the $\ddot{\alpha}_a$ and $\ddot{\alpha}_r$ values. For instance, in Flight 10 a constant $+1.6^\circ$ bias in $\ddot{\alpha}_r$ was observed in all straight and level test cases. The $\ddot{\alpha}_a$ also had a small bias of about 0.3° for Flight 10. The $\ddot{\alpha}_a$ and $\ddot{\alpha}_r$ were manually trimmed, and the small error could not be detected from the cockpit. The trim error contributed directly to an error in the control surface deflection results.

Overall the asymmetric thrust flight test data did not match the theoretical predictions. The correct trend was seen in the data, but the flight test results had large differences from the expected values. The difficulty in establishing trimmed flight in an asymmetrical flight condition and the inaccuracy in the bank angle measurement aggravated the errors. Next trim conditions 2 and 3 were investigated jointly in the flight test program.

Climbing and Descending Flight Test.

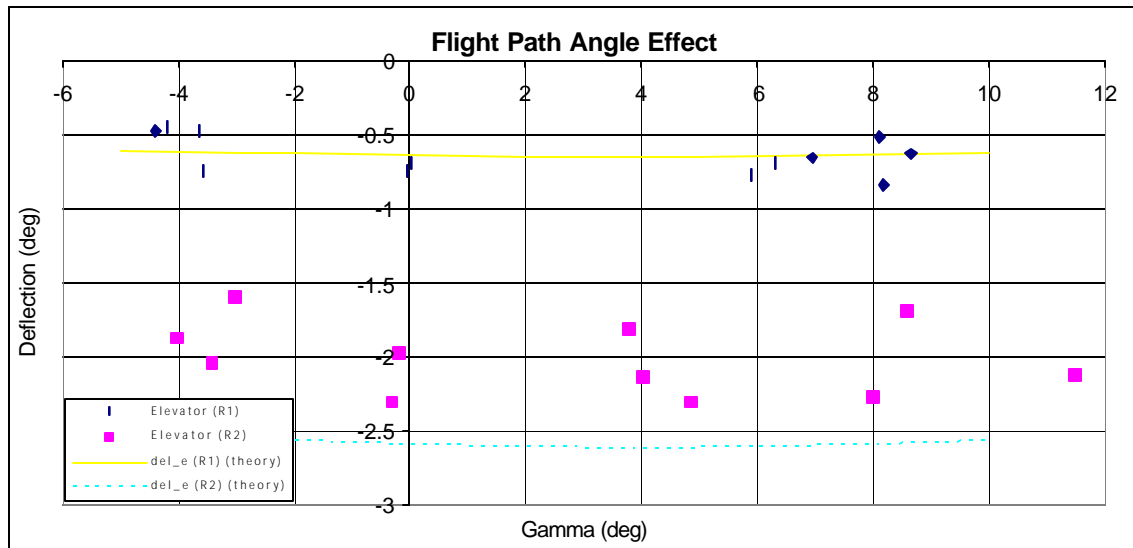


Figure 43. Elevator Deflection (δ_e) vs. Flight Path Angle (γ) Effect

The effect of flight path angle changes was investigated for both climbing (trim condition 2) and descending (trim condition 3) flight. The γ effect on \ddot{a}_e is shown in Figure 43 for both regimes. The γ effect on \ddot{a}_e was predicted to be very small, and the flight test data matched the predictions. In Regime 1, all the flight test data were within

$\pm 0.25^\circ$ of the theoretical curve. In Regime 2 the flight test \ddot{a}_e was biased $+0.7^\circ$ from the predicted value. The flight test data were also more scattered about the average value in Regime 2 than in Regime 1. Overall, the predicted γ correlation to \ddot{a}_e matched flight test results, but the impact of γ on \ddot{a}_e was very small.

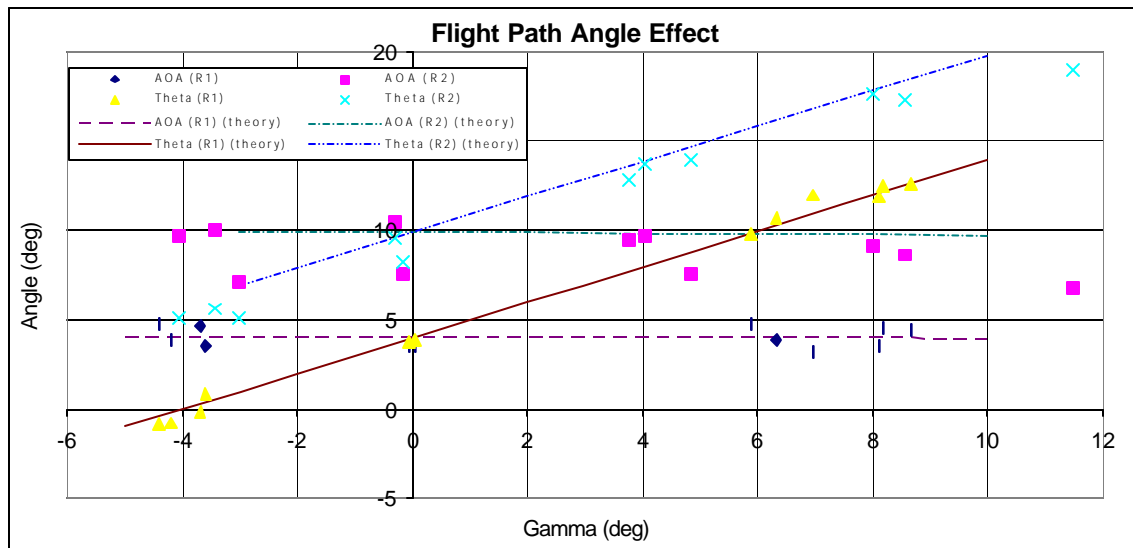


Figure 44. Angle of Attack (α) and Pitch Angle (θ) vs. Flight Path Angle (γ) Effect

Figure 44 shows the comparison of flight test γ effect on α and θ respectively to the theoretically predicted relationship. In Regime 1, all flight test data for both α and θ were within $\pm 1.0^\circ$ of the model prediction for all γ values. In Regime 2 the flight test data were within $\pm 2.0^\circ$ of the predicted value, with a slight bias of about -1.0° . As seen for other longitudinal investigations, the scatter in the α data points was larger than the scatter in the θ values. Overall, the flight test data correlated with the predicted values for all γ . The impact of γ was not significant, but was predicted properly by theory.

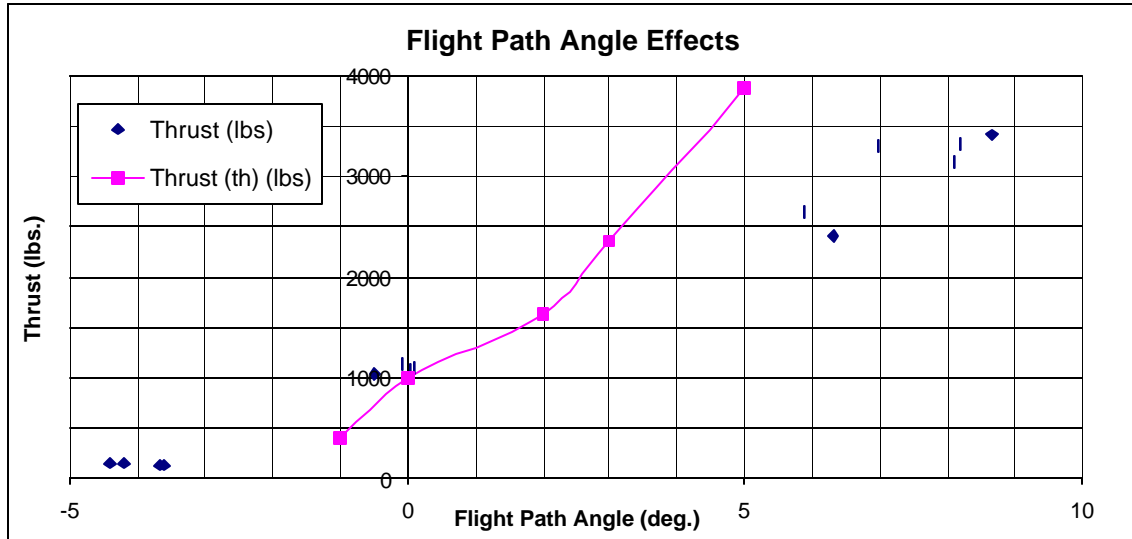


Figure 45. Thrust (T) vs. Flight Path Angle (γ) Effect

The flight path angle had a significant impact on the thrust required to maintain trimmed flight. Figure 45 shows the thrust data collected as flight path angle was varied. The flight test roughly had the same trend as the predicted curve, but as data was taken further from the center test condition, the difference between the measured and predicted data grew large. The flight test data followed a nearly linear trend, while a trigonometric function was predicted from the model. The increased error at the extremes of the thrust envelope was likely due to errors in the calculated thrust from flight test and the model.

Crabbing Flight Test.

Next a lateral-directional trim condition was investigated, the effect of a non-zero sideslip angle in level flight. With β specified, the ϕ required to maintain $\gamma = H = 0^\circ$ was determined. The test was limited to $\pm 10^\circ$, due to aircraft safety concerns.

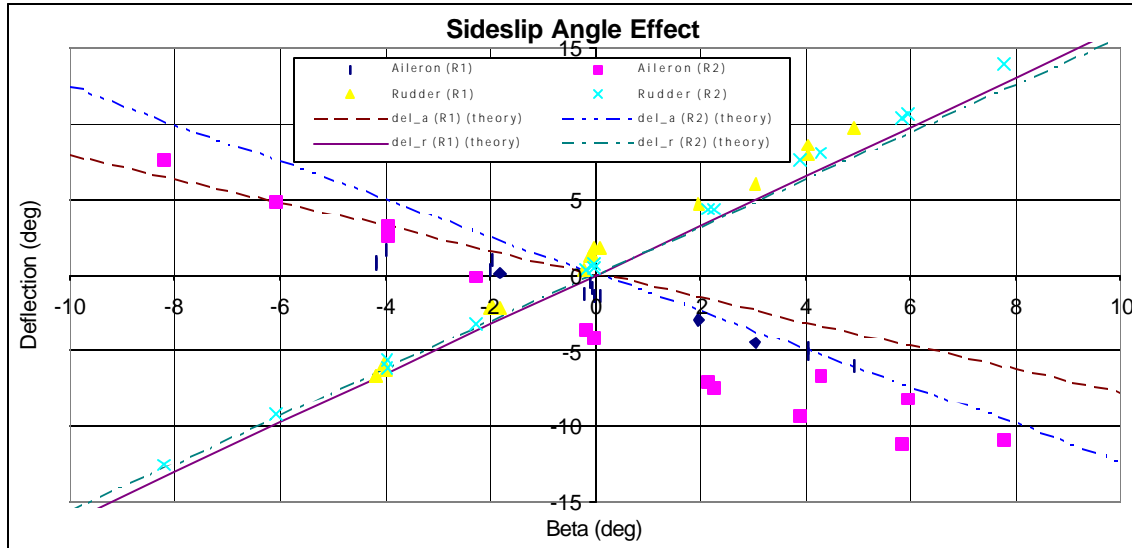


Figure 46. Aileron (δ_a) and Rudder (δ_r) Surface Deflections vs. Sideslip Angle (β) Effect

Regime 1 and Regime 2, \ddot{a}_a and \ddot{a}_r were compared to the \ddot{a}_a and \ddot{a}_r predicted by the model. The \ddot{a}_r and \ddot{a}_a are shown in Figure 46. The flight test data for \ddot{a}_a and \ddot{a}_r were linear, as was predicted by the model. In addition, the slopes of the flight test data had similar slopes to that predicted by the model. When the slopes did vary from the model predictions, the slope of the flight test data was higher, but only by approximately 0.1° of \ddot{a} per degree of β . It was also noted that at $\beta = 0^\circ$, \ddot{a}_a was negative and \ddot{a}_r was positive. The deflection at $\beta = 0^\circ$ had much more effect on moving the data away from the prediction than the slopes of the data. The rudder showed zero deflection at approximately $\beta = -2^\circ$, and the ailerons showed no deflection at approximately $\hat{\alpha} = -0.5^\circ$. It is unknown if this was an instrumentation issue, a slightly bent aircraft, non-zeroed trim, or a combination of each factor.

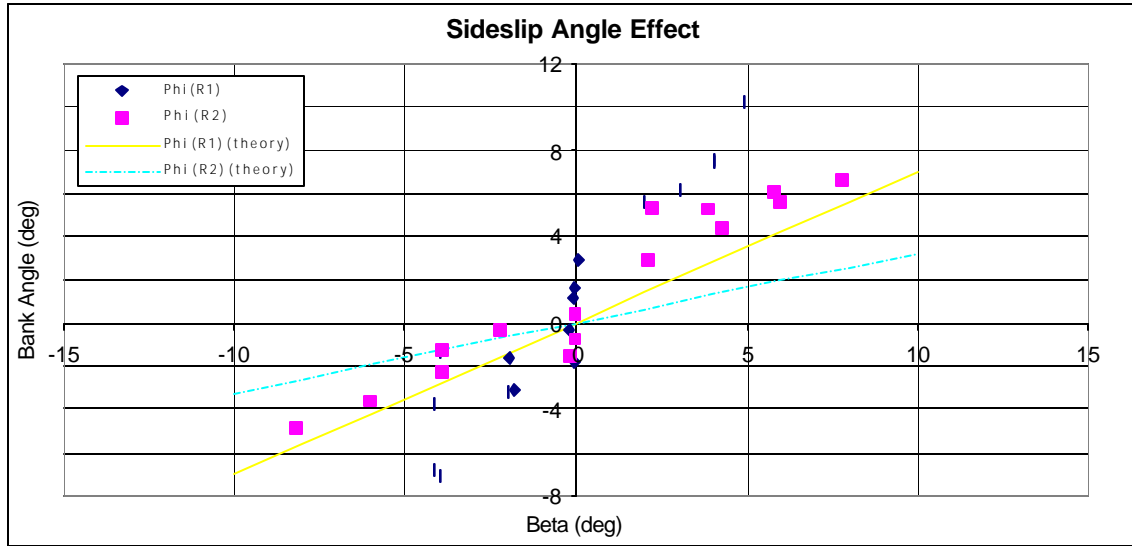


Figure 47. Bank Angle (ϕ) vs. Sideslip Angle (β) Effect

The ϕ flight test data were also graphed for the steady-heading sideslips, as seen in Figure 47. For Regime 1 and Regime 2, the slope from the flight test data was approximately 2.5 times greater than the predicted slope.

Overall, the data quality from flight test was good and showed a linear relationship between control surface deflection and β , and ϕ to β . The slopes of the control surface deflection to $\hat{\alpha}$ closely matched model prediction, while the slope of ϕ to $\hat{\alpha}$ differed from the model by a factor of 2.5.

Level, Steady Turn Flight Test.

The flight test results for trim condition 5, did not match the predictions. The open-loop equations predict a certain path with either a specified bank angle or sideslip angle. When ϕ_v was specified, the predicted bank angle was over the aircraft limits, which required a much larger \ddot{a}_a and \ddot{a}_r than measured in flight test. The aircraft was

flown with nearly zero sideslip, but when $\beta=0^\circ$ was specified the open-loop equations predicted very large control surface deflection to command the turn, which limited the maximum ϕ_v . In flight, bank angle is used to command a turn, which requires little control surface deflection. The flights should be repeated attempting to recreate the exact flight conditions. The flight trajectory flown, did not match the mathematically predicted trajectory. Also turn rate had a major impact on the predicted control surface deflection values. The turn rate was not specified for the flight tests, and was not measured. The predicted turn rate should be compared to the actual flight test turn rate to make a valid comparison.

Pitch-Over Flight Test.

Trim condition 10 flight trajectory also did not match the predicted results. The predicted trajectory was for straight and level flight, with a pitch angle rotation about the y_b -axis created by deflecting \ddot{a}_e only in 1g flight. To achieve the same pitch rotation rate in flight test, the maneuver was entered in a climb with a pitch-over, and less than 1g flight. The lower the load factor, the higher the pitch rate. Post-flight, load factor and pitch rate were varied to attempt to re-create the flight trajectory. The equations did not predict the same trajectory flown, so the required \ddot{a}_e 's did not match.

Summary

The longitudinal flight test data provided a good validation of all the model predictions, except trim condition 10. In straight and level flight, velocity was the dominant input parameter for determining the required \ddot{a}_e . Weight had a small effect and altitude an even smaller impact. The flight path angle had a minimal impact on the \ddot{a}_e . Thrust setting had the greatest impact on the flight path angle. \ddot{a}_e was not significantly

changed by changes in γ . Trim condition 10 could not be reproduced as a trim condition using the open-loop model.

The lateral-directional flight test data provided limited validation of the model predictions. The \ddot{a}_a and \ddot{a}_r curves had the same general trends for both the asymmetrical thrust and sideslip investigations. The data was biased by errors in the lateral-directional stability derivatives and biases in the lateral-directional measurements on the aircraft. The lateral-directional data could not be guaranteed to be accurate to within 1.0° . The trim condition 5 flight trajectory could not be reproduced using the model predicted trajectory.

VII. Conclusions and Recommendations

Conclusions

Model Development.

Outer-loop equations were developed to produce control laws for an aircraft. Nested loop equations were developed for the model. In the outer-loop controller, the aircraft was modeled as a point mass. All aircraft forces were balanced to create equations to solve the control variables. For specified state variables and either bank angle or sideslip angle to define the flight trajectory the control variables were determined.

The inner-loop uses the control variables from the outer-loop to calculate the required control surface deflections. In the inner-loop, the six-degree of freedom model was used to balance the moments on the aircraft. With the control variables determined from the flight trajectory in the outer-loop, the inner-loop calculates the required δ_a , δ_e , and δ_r to achieve the desired aircraft orientation.

Trim Conditions.

Ten trim conditions were then defined to allow simplifying assumptions to the model equations. Trim condition 1, is straight and level flight. Trim condition 2 is defined as a straight and level climb. A straight and level descent describes trim condition 3. A non-zero sideslip angle in level flight is trim condition 4. Trim condition 5 is a steady, level turn. By adding a positive flight path angle, trim condition 6 describes a steady climbing turn. Similarly, trim condition 7 is a descending turn. Trim condition

8 is a barrel roll. Next, for trim condition 9, an AC-130 gunship orbit is developed. Finally, in trim condition 10, a steady pitch-over maneuver is described. Model equations were developed for each trim condition.

Model Implementation.

The equations were then implemented using a Learjet-25 aircraft aeromodel in a Matlab® routine. Each trim condition was plotted to determine the relationships between the relevant input variables and the outputs. The impact of each input variable on the output for the Learjet-25 was determined. The trim condition graphs were used to determine which input variables were focused on during the flight test investigation.

Predicted Results.

Velocity had the largest influence on trim condition 1 results with weight and altitude having small impacts on control variables and δ_e . For asymmetrical thrust, there were linear relationships for both δ_a and δ_r as the difference in thrust between engines was increased. For trim condition 2 and 3, thrust was the most important parameter. The flight path angle was limited by the thrust for both climbing and descending flight. In trim condition 4, a linear relationship was again found for both δ_a and δ_r as the sideslip angle was increased. For trim condition 5, the steady turn was defined as a constant turn rate with a load factor of 1.0 to allow a valid comparison. To simulate an actual turn, the load factor should be varied with bank angle, and β should be held to 0.0° . Again a linear relationship was observed for both δ_a and δ_r as the bank angle was increased. For trim conditions 6 and 7 δ_a and δ_r had relationships nearly identical to trim condition 5. The only difference between the two trim conditions was the required thrust was dependent

on the flight path angle similar to trim condition 2 and 3. For the barrel roll, a constant roll rate was chosen, and β was assumed to be zero. This flight condition describes an aileron roll. To offset from the roll axis, the sideslip angle must be increased. For trim condition 8, δ_a was the limiting factor. Trim condition 9 was a subset of trim condition 5. Formulas were found relating height above the target, weapon depression angle, and orbit radius. Finally a pitch-over maneuver was examined. The pitch rate was set, and load factor varied from 1.0 to 0.4 g's. The pitch-over was limited by the maximum elevator deflection.

Predicted Derivative Sensitivity.

The equation predictions are very sensitive to errors in the stability derivatives. The most sensitive stability derivatives are $C_{n_{ir}}$, C_{y_a} , C_{n_a} , and C_{l_a} . An error greater than seven percent in any of these stability derivatives creates a 1.0° difference in the predicted control surface value. To get the desired accuracy in the equation predictions, the stability derivatives must be known to great certainty. The stability derivatives originally provided by Veridian had as large as 40% errors from the values found in flight test. The longitudinal stability derivatives had been determined in previous studies and were much more accurate than the lateral-directional stability derivatives (reference 10). Unfortunately the lateral-directional stability derivatives required the most accuracy according to the sensitivity analysis. C_{l_b} and $C_{l_{ia}}$ were not determined to within the required accuracy. Therefore the lateral-directional predictions cannot be guaranteed to be within 1.0° of the flight test results.

Flight Test Results.

The equation predictions were partially verified by the flight test program. The longitudinal test results matched the predictions for trim conditions 1, 2 and 3. The lateral-directional test results had errors from the predictions for trim conditions 1 and 4, but were within acceptable limits. Trim conditions 5 and 10 test predictions did not match the predictions. The errors were probably due to not flying these maneuvers at 1g and errors in the stability derivatives. Also the last two trim conditions could not be exactly reproduced by the same flight trajectory using the control equations.

The thrust predictions had large errors and were not very accurate. The thrust predictions had two major sources of error. First, the aircraft measurement and model for thrust introduced an error. Thrust was calculated by measuring the engine pressure ratio and the pressure at the compressor face. The pressure at the nozzle was calculated and multiplied by the nozzle area to estimate the force. The thrust estimate was not very accurate. From flight test, the engines were balanced from all readings in the cockpit, but post-flight up to a 200 lbs difference between engines was noted at some test points. Also, test points flown at nearly identical test conditions on different flights had up to 100 lbs difference. The second source of error was that the thrust modeled as a point force acting at the estimated center of the nozzle. The model simplifications may have also introduced an error.

Error Sources.

The equations were able to accurately predict non-aggressive level flight maneuvers, which would be the majority of flight for a UAV. The complex maneuvers were not validated in the flight test program. The steady turns predicted by the equations

were also not reproduced in flight. Steady turns are a balance of turn rate, bank angle and sideslip angle. The equations predict a different combination of these three parameters than were flown. The predicted steady turn may be a valid solution to the turn, but it was not verified in flight test. The control surface deflections are smaller than predicted due to the use of bank angle to balance the forces. The pitch-over maneuver also was not validated in flight. Pointing the bottom of the aircraft at a stationary target on the ground was predicted by the equations, but may not be possible on an actual aircraft. Further tests and research is needed.

The model was accurate near the center test point condition, but the errors grew larger, the farther from the equilibrium test point. The errors have three primary sources.

Stability Derivative Variability.

First, the stability derivatives were a function of multiple variables. From flight test, as Mach number, altitude and dynamic pressure changed the stability derivative values changed. Temperature and air density also had a small impact on the predictions. To predict the required control surface deflection with great accuracy, the stability derivatives would need to be mapped for the entire flight envelope to the desired accuracy determined in the sensitivity analysis.

Instrumentation Errors.

Second, the aircraft measurement instrumentation needs to be improved. Small errors in the measured angle of attack, sideslip, bank angle and airspeed directly impacted the accuracy of the flight test results. It was also noted that altitude measurement changed when maneuvers other than straight and level flight were flown. The altitude error was probably due to no correction in the static pressure measurement when flow

over the static port was disrupted in other than straight and level flight. A Pitot static calibration should be performed. The accelerations and angular rotation measurements were also very noisy, which resulted in an averaged value with occasional large uncertainties. To achieve the accuracy needed for the model equations, very accurate measurements are required. Finally there was no direct method to record aircraft weight. The data was displayed in the cockpit, but the data recorded from the data bus was an estimate provided by Veridian.

Non-linear Effects.

Finally, at the edges of the flight envelope non-linear flight effects become evident. As stall is approached, the lift curve slope becomes non-linear. Also at higher Mach numbers, compressibility effects must be considered. At higher dynamic pressures the assumption of a rigid body may not be valid. Another concern not addressed is the movement of the center of gravity as fuel was burned. These effects are not included in the model and therefore would introduce an error. The model accuracy would decrease the further from the center test condition the maneuver was flown. Finally thrust was assumed to be invariant as altitude, velocity and temperature changed. This simplifying assumption likely introduced an increasing error as test data was collected away from the center test condition.

Recommendations

The open-loop equations provide a good prediction of the required control settings for some of the specified trim conditions. With additional work the model could be implemented on a UAV application. This section will address shortcomings identified during research and additional issues that need to be addressed.

Validate Turn Predictions.

The steady turn predictions need to be validated. Post-flight test, the effect of load factor was added to the equations to predict a loaded turn. The equations still predicted much higher control surface deflections than were seen in flight. Pilot's typically use more bank angle than control surface deflection to turn the aircraft. The equations predict a small bank angle and large control surface deflection trajectory. The predicted trajectory and control surface deflections should be flight tested to validate the predicted solution. The predicted trimmed turn may be a valid turn solution, just not the ones found in flight test.

Improve Thrust Model.

The thrust model must be improved. The model provided for flight test did not provide the accuracy to totally validate the model thrust predictions. Near the center test conditions the results were good, but at the upper end of the thrust envelope the flight test measurements differed significantly from the predicted results. The thrust model had many simplifying assumptions, which may need to be readdressed to accurately predict the proper engine settings.

Include Wind Effect in Model.

The uncertainties in the atmosphere need to be included in the model. Wind gusts and other variations in wind should be included to better model the actual flight conditions. A wind gust would add a force and moment to the system, which is currently not included in the force and moment summations. The wind variations would disrupt the assumption of zero net forces and moments, and the aircraft would no longer be in a trimmed flight condition.

Investigate Transitions between Trim Conditions.

The model assumes stable, trimmed flight conditions. No control input is provided to get to the trimmed condition. Typically large inputs are commanded to move the aircraft to a new flight condition. To transition from one trimmed condition to the next, additional control commands must be input. If the trim condition control commands are the only inputs into the aircraft, the aircraft may slowly approach the trim condition, but may never reach the desired trimmed condition. The transition between trimmed conditions was not addressed in the open-loop model. Control surface limits may also be exceeded during transitions between trim conditions.

Determine Stability Derivatives Accurately.

The stability derivatives require very accurate estimates to make valid predictions. Wind tunnel estimates of stability derivatives do not produce the required stability derivative accuracy. An extensive flight test program is required to provide an accurate aeromodel of the aircraft.

To implement the control loop equations on a UAV, very accurate flight condition measurements would be required. The test aircraft had some of the best measurement instrumentation economically available. The measurements were still near the acceptable accuracy limits and exceeded error limits in some cases. Extremely accurate angle, velocity and acceleration measurements would be needed to implement the open-loop control model on an aircraft.

Measure Weight Accurately.

The weight measurement was estimated since the flight data was not available on the data bus. The weight was only available as a display in the cockpit. A constant fuel

burn rate was assumed and aircraft weight was decremented as a function of flight time. The decrement rate was varied the first few flights to find the most accurate weight estimate. Also the weight was periodically reset to the cockpit display to increase accuracy. The weight value occasionally drifted from the actual value though. The weight of the aircraft should be accurately measured to provide the accuracy needed to validate the weight related model predictions.

Automate Matlab® Routine.

The Matlab® routine could be automated to accept flight condition inputs and output the required control settings. Shell programs could be developed to take inputs directly from the air data computer for air density, temperature, current velocity, and aircraft weight. The shell program could be designed to prompt for the velocity, flight path angle, and either bank angle or sideslip angle for the desired trajectory. Additionally rotational rates and angular accelerations could be input for the three axes. The output control surface deflections and engine setting could be sent directly to the aircraft bus controller. Also the angle of attack, sideslip, and bank angle could be compared to the aircraft measurements to monitor the aircraft trajectory.

APPENDIX A: SAMPLE CALCULATIONS

Introduction

This appendix includes sample calculations to support the equations developed in the inner- and outer-loop equations. The numbers in parenthesis correspond to the equation number in the main text of the document.

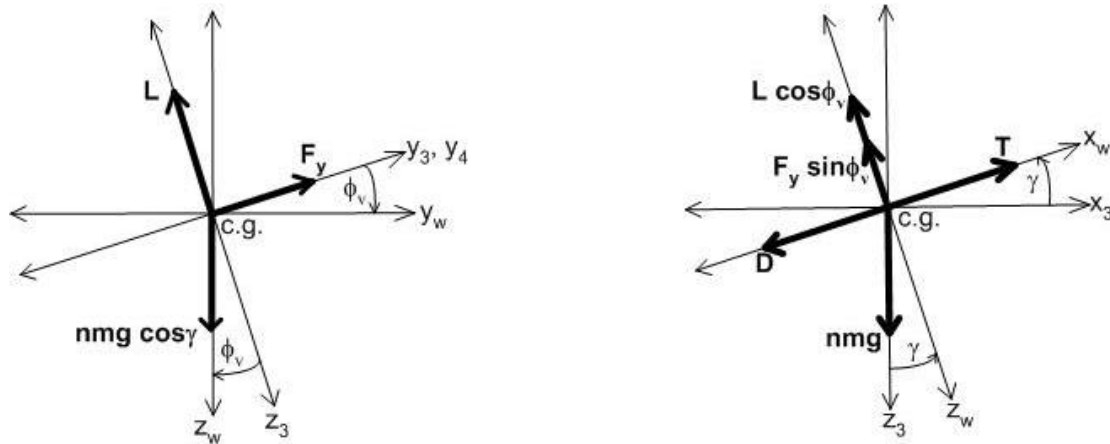


Figure 48. Force Definitions

Outer-Loop Calculations

The outer-loop equations were redefined in Chapter 2. The derivations for the equations follow. First the forces from Figure 48 were summed in all three axes

$$\sum F_{x_w} = T - D - n m g \sin \gamma = m a_x = m \ddot{x}$$

$$\Rightarrow \ddot{x} = \frac{T - D}{m} - ng \sin \tilde{\alpha} \quad (\text{Eqn. 5})$$

$$\sum F_{z_w} = -L \cos \phi_v - F_y \sin \phi_v + n m g \cos \gamma = m a_z = m (-V \ddot{x})$$

$$\Rightarrow \ddot{\alpha} = \frac{L \cos \mathbf{f}_v + F_y \sin \mathbf{f}_v}{mV} - \frac{ng}{V} \cos \tilde{\alpha} \quad (\text{Eqn. 6})$$

$$\Sigma F_{y_w} = F_y \cos \phi_v - L \sin \phi_v = m a_y = m (V \cos \gamma \dot{\mathbf{H}})$$

$$\Rightarrow \dot{\mathbf{H}} = \frac{-L \sin \mathbf{f}_v + F_y \cos \mathbf{f}_v}{mV \cos \tilde{\alpha}} \quad (\text{Eqn. 7})$$

The following forces were defined in Chapter 2

$$L = \bar{q} \frac{V^2}{V_o^2} C_{L\tilde{\alpha}} (\alpha + \tilde{\alpha}_{o_L}) \quad (\text{Eqn. 1})$$

$$D = \bar{q} \frac{V^2}{V_o^2} (C_{D\tilde{\alpha}} \alpha + C_{D_o}) \quad (\text{Eqn. 2})$$

$$F_y = \bar{q} \frac{V^2}{V_o^2} \frac{S_t}{S_w} C_{y\tilde{\alpha}} \beta \quad (\text{Eqn. 3})$$

$$T = mg\mu \quad (\text{Eqn. 4})$$

The defined forces were substituted into equations (5) through (7)

$$\dot{\mathbf{V}} = g\mathbf{m} - \frac{\bar{q}V^2}{mV_o^2} (C_{D_a} \mathbf{a} + C_{D_o}) - ng \sin \tilde{\alpha}$$

$$\ddot{\alpha} = \frac{\bar{q}V^2}{mV_o^2} \frac{\cos \mathbf{f}_v C_{L_a} (\mathbf{a} + \mathbf{a}_{o_L}) + \frac{S_t}{S_w} C_{y_b} \mathbf{b} \sin \mathbf{f}_v}{V} - \frac{ng}{V} \cos \tilde{\alpha}$$

$$\dot{\mathbf{H}} = \frac{\bar{q}V^2}{mV_o^2} \frac{\frac{S_t}{S_w} C_{y_b} \mathbf{b} \cos \mathbf{f}_v - \sin \mathbf{f}_v C_{L_a} (\mathbf{a} + \mathbf{a}_{o_L})}{V \cos \tilde{\alpha}}$$

Simplifying assumptions were then made for each trim condition.

Trim Conditions 1, 2, 3, and 4.

Trim condition: $\delta = \dot{\delta} = \ddot{\delta} = 0^\circ$ (β independent)

$$0 = \frac{\bar{q}V^2}{V_o^2} \left[\frac{S_t}{S_w} C_{y_b} \mathbf{b} \cos \mathbf{f}_v - \sin \mathbf{f}_v C_{L_a} (\mathbf{a} + \mathbf{a}_{o_L}) \right] \quad (\text{from } \mathbf{H} \text{ equation})$$

$$\frac{\sin \mathbf{f}_v}{\cos \mathbf{f}_v} = \tan \mathbf{f}_v = \frac{\frac{S_t}{S_w} C_{y_b} \mathbf{b}}{C_{L_a} (\mathbf{a} + \mathbf{a}_{o_L})}$$

$$\mathbf{b} = \frac{\tan \mathbf{f}_v C_{L_a} (\mathbf{a} + \mathbf{a}_{o_L})}{\frac{S_t}{S_w} C_{y_b}}$$

$$0 = \frac{\bar{q}V^2}{V_o^2} \left(\cos \mathbf{f}_v C_{L_a} (\mathbf{a} + \mathbf{a}_{o_L}) + \frac{S_t}{S_w} C_{y_b} \mathbf{b} \sin \mathbf{f}_v \right) - nmg \cos \tilde{\alpha} \quad (\text{from } \mathbf{g} \text{ equation})$$

$$\frac{nmg \cos \tilde{\alpha}}{\frac{\bar{q}V^2}{V_o^2}} = \cos \mathbf{f}_v C_{L_a} (\mathbf{a} + \mathbf{a}_{o_L}) + \frac{S_t}{S_w} C_{y_b} \mathbf{b} \sin \mathbf{f}_v \quad (\text{substituting for } \beta)$$

$$\frac{nmg \cos \tilde{\alpha}}{\frac{\bar{q}V^2}{V_o^2}} = \cos \mathbf{f}_v C_{L_a} (\mathbf{a} + \mathbf{a}_{o_L}) + \frac{S_t}{S_w} C_{y_b} \frac{\tan \mathbf{f}_v C_{L_a} (\mathbf{a} + \mathbf{a}_{o_L})}{\frac{S_t}{S_w} C_{y_b}} \sin \mathbf{f}_v$$

$$\frac{nmg \cos \tilde{\alpha}}{\frac{\bar{q}V^2}{V_o^2}} = C_{L_a} (\mathbf{a} + \mathbf{a}_{o_L}) \left(\cos \mathbf{f}_v + \frac{\sin^2 \mathbf{f}_v}{\cos \mathbf{f}_v} \right)$$

$$\frac{nmg \cos \tilde{\alpha}}{\frac{\bar{q}V^2}{V_o^2}} \cos \mathbf{f}_v = C_{L_a} (\mathbf{a} + \mathbf{a}_{o_L}) (\cos^2 \mathbf{f}_v + \sin^2 \mathbf{f}_v) = C_{L_a} (\mathbf{a} + \mathbf{a}_{o_L})$$

$$\mathbf{a} = \frac{1}{C_{L_a}} \left(\frac{V_o^2 nmg \cos \tilde{\alpha}}{\bar{q}V^2} \cos \mathbf{f}_v \right) - \mathbf{a}_{o_L}$$

$$0 = g\mathbf{m} - \frac{\bar{q}V^2}{mV_o^2}(C_{D_a}\mathbf{a} + C_{D_o}) - n\mathbf{g} \sin \tilde{\alpha} \quad (\text{from } \cancel{V} \text{ equation})$$

$$\mathbf{m} = \frac{\bar{q}V^2}{mgV_o^2}(C_{D_a}\mathbf{a} + C_{D_o}) + n \sin \tilde{\alpha} \quad (\text{substituting for } \alpha)$$

$$\mathbf{m} = \frac{\bar{q}V^2}{mgV_o^2} \left[\frac{C_{D_a}}{C_{L_a}} \left(\frac{V_o^2 n m g \cos \tilde{\alpha}}{\bar{q}V^2} \cos \mathbf{f}_v \right) - C_{D_a} \mathbf{a}_{oL} + C_{D_o} \right] + n \sin \tilde{\alpha}$$

$$\mathbf{m} = \frac{C_{D_a}}{C_{L_a}} (n \cos \tilde{\alpha} \cos \mathbf{f}_v) + \frac{\bar{q}V^2}{mgV_o^2} (C_{D_o} - C_{D_a} \mathbf{a}_{oL}) + n \sin \tilde{\alpha}$$

Returning to the original $\mathbf{H}=0$ equation, dividing by $\frac{\bar{q}V^2}{V_o^2}$, and simplifying

$$\sin \mathbf{f}_v C_{L_a} (\mathbf{a} + \mathbf{a}_{oL}) = \frac{S_t}{S_w} C_{y_b} \mathbf{b} \cos \mathbf{f}_v$$

$$\sin \mathbf{f}_v = \frac{\frac{S_t}{S_w} C_{y_b} \mathbf{b} \cos \mathbf{f}_v}{C_{L_a} (\mathbf{a} + \mathbf{a}_{oL})} \quad (\text{substituting for } \alpha)$$

$$\sin \mathbf{f}_v = \frac{\frac{S_t}{S_w} C_{y_b} \mathbf{b} \cos \mathbf{f}_v}{C_{L_a} \left[\frac{1}{C_{L_a}} \left(\frac{V_o^2 n m g \cos \tilde{\alpha}}{\bar{q}V^2} \cos \mathbf{f}_v \right) - \mathbf{a}_{oL} + \mathbf{a}_{oL} \right]}$$

$$\Rightarrow \sin \phi_v = \frac{C_{y_a} S_t \bar{q}}{V_o^2 n m g S_w} \frac{V^2 \hat{\alpha}}{\cos \tilde{\alpha}} \quad (\text{Eqn. 8})$$

From the trigonometric relationship

$$\cos^2 \mathbf{f}_v = 1 - \sin^2 \mathbf{f}_v = 1 - \left(\frac{\frac{S_t}{S_w} C_{y_b} \mathbf{b} \bar{q} V^2}{V_o^2 n m g \cos \tilde{\alpha}} \right)^2$$

$$\Rightarrow \cos\phi_v = \sqrt{1 - \left(\frac{C_{y_a} S_t \bar{q} V^2 \hat{a}}{V_o^2 n m g S_w \cos \tilde{a}} \right)^2} \quad (\text{Eqn. 9})$$

Substitute $\cos\phi_v$ into α

$$\mathbf{a} = \frac{1}{C_{L_a}} \left(\frac{V_o^2 n m g \cos \tilde{a}}{\bar{q} V^2} \sqrt{1 - \left(\frac{C_{y_a} S_t \bar{q} V^2 \hat{a}}{V_o^2 n m g S_w \cos \tilde{a}} \right)^2} \right) - \mathbf{a}_{o_L}$$

$$\Rightarrow \alpha = \frac{1}{C_{L_d}} \left(\sqrt{\left(\frac{V_o^2 n m g \cos \tilde{a}}{\bar{q} V^2} \right)^2 - \left(\frac{C_{y_a} S_t \hat{a}}{S_w} \right)^2} \right) - \hat{a}_{o_L} \quad (\text{Eqn. 10})$$

Substitute $\cos\phi_v$ into μ

$$\mathbf{m} = \frac{C_{D_a}}{C_{L_a}} \left(n \cos \tilde{a} \sqrt{1 - \left(\frac{C_{y_a} S_t \bar{q} V^2 \hat{a}}{V_o^2 n m g S_w \cos \tilde{a}} \right)^2} \right) + \frac{\bar{q} V^2}{m g V_o^2} (C_{D_o} - C_{D_a} \mathbf{a}_{o_L}) + n \sin \tilde{a}$$

$$\Rightarrow \mu = \frac{\bar{q} V^2}{m g V_o^2} (C_{D_o} - C_{D_a} \hat{a}_{o_L}) + \sqrt{\left(\frac{C_{D_d} n \cos \tilde{a}}{C_{L_d}} \right)^2 - \left(\frac{C_{D_d} C_{y_a} S_t \bar{q} V^2 \hat{a}}{C_{L_d} V_o^2 n m g S_w} \right)^2} + n \sin \tilde{a}$$

(Eqn. 11)

Trim condition 1: $\tilde{\alpha} \leftarrow \tilde{\nu} = \hat{\alpha} = 0^\circ$ (ϕ_v independent) (from Equation 8)

$$\sin\phi_v = \frac{C_{y_a} S_t \bar{q} V^2 \hat{a}}{V_o^2 n m g S_w \cos \tilde{a}}$$

$$\Rightarrow \beta = \frac{V_o^2 n m g S_w \cos \tilde{a}}{C_{y_a} S_t \bar{q} V^2} \sin \mathbf{f}_v \quad (\text{Eqn. 12})$$

From previous equations

$$\Rightarrow \mathbf{a} = \frac{1}{C_{L_a}} \left(\frac{V_o^2 n m g \cos \tilde{\alpha}}{\bar{q} V^2} \cos \mathbf{f}_v \right) - \mathbf{a}_{o_L} \quad (\text{Eqn. 13})$$

$$\Rightarrow \mathbf{m} = \frac{C_{D_a}}{C_{L_a}} (n \cos \tilde{\alpha} \cos \mathbf{f}_v) + \frac{\bar{q} V^2}{m g V_o^2} (C_{D_o} - C_{D_a} \mathbf{a}_{o_L}) + n \sin \tilde{\alpha} \quad (\text{Eqn. 14})$$

Trim Conditions 5, 6, 7, and 9.

Trim condition: $\tilde{\alpha} = \tilde{\psi} = 0^\circ$ and $\dot{\mathbf{H}} = \mathbf{v}_\psi$ (or $H(t) = \mathbf{v}_\psi t$)

$$0 = g \mathbf{m} - \frac{\bar{q} V^2}{m V_o^2} (C_{D_a} \mathbf{a} + C_{D_o}) - n g \sin \tilde{\alpha} \quad (\text{from } \tilde{V} \text{ equation})$$

$$0 = \frac{\bar{q} V^2}{V_o^2} \left(\cos \mathbf{f}_v C_{L_a} (\mathbf{a} + \mathbf{a}_{o_L}) + \frac{S_t}{S_w} C_{y_b} \mathbf{b} \sin \mathbf{f}_v \right) - n m g \cos \tilde{\alpha} \quad (\text{from } \tilde{g} \text{ equation})$$

$$m V \mathbf{v}_\psi \cos \mathbf{g} = \frac{\bar{q} V^2}{V_o^2} \left[\frac{S_t}{S_w} C_{y_b} \mathbf{b} \cos \mathbf{f}_v - \sin \mathbf{f}_v C_{L_a} (\mathbf{a} + \mathbf{a}_{o_L}) \right] \quad (\text{from } \dot{\mathbf{H}} \text{ equation})$$

From the second and third equations

$$\cos \mathbf{f}_v C_{L_a} (\mathbf{a} + \mathbf{a}_{o_L}) + \frac{S_t}{S_w} C_{y_b} \mathbf{b} \sin \mathbf{f}_v = \frac{V_o^2}{\bar{q} V^2} n m g \cos \tilde{\alpha}$$

$$\frac{S_t}{S_w} C_{y_b} \mathbf{b} \cos \mathbf{f}_v - \sin \mathbf{f}_v C_{L_a} (\mathbf{a} + \mathbf{a}_{o_L}) = \frac{V_o^2}{\bar{q} V^2} m V \mathbf{v}_\psi \cos \mathbf{g}$$

$$\begin{bmatrix} C_{L_a} (\mathbf{a} + \mathbf{a}_{o_L}) & \frac{S_t}{S_w} C_{y_b} \mathbf{b} \\ \frac{S_t}{S_w} C_{y_b} \mathbf{b} & -C_{L_a} (\mathbf{a} + \mathbf{a}_{o_L}) \end{bmatrix} \begin{bmatrix} \cos \mathbf{f}_v \\ \sin \mathbf{f}_v \end{bmatrix} = \frac{V_o^2}{\bar{q} V^2} m \cos \tilde{\alpha} \begin{bmatrix} n g \\ V \mathbf{v}_\psi \end{bmatrix}$$

$$\sin \mathbf{f}_v = \frac{1}{C_{L_a}^2 (\mathbf{a} + \mathbf{a}_{o_L})^2 + \left(\frac{S_t}{S_w} C_{y_b} \mathbf{b} \right)^2} \frac{V_o^2}{\bar{q} V^2} m \cos \tilde{\alpha} \left[-C_{L_a} (\mathbf{a} + \mathbf{a}_{o_L}) V \mathbf{v}_\psi + n g \frac{S_t}{S_w} C_{y_b} \mathbf{b} \right]$$

$$\cos \mathbf{f}_v = \frac{1}{C_{L_a}^2 (\mathbf{a} + \mathbf{a}_{o_L})^2 + \left(\frac{S_t}{S_w} C_{y_b} \mathbf{b} \right)^2} \frac{V_o^2}{\bar{q} V^2} m \cos \tilde{\alpha} \left[C_{L_a} (\mathbf{a} + \mathbf{a}_{o_L}) \mathbf{V} \mathbf{v}_\psi + ng \frac{S_t}{S_w} C_{y_b} \mathbf{b} \right]$$

Again, $\cos^2 \mathbf{f}_v + \sin^2 \mathbf{f}_v = 1$

$$1 = \frac{1}{\left[C_{L_a}^2 (\mathbf{a} + \mathbf{a}_{o_L})^2 + \left(\frac{S_t}{S_w} C_{y_b} \mathbf{b} \right)^2 \right]^2} \left(\frac{V_o^2}{\bar{q} V^2} m \cos \tilde{\alpha} \right)^2 \left\langle (ng)^2 C_{L_a}^2 (\mathbf{a} + \mathbf{a}_{o_L})^2 + \left(\mathbf{V} \mathbf{v}_\psi \frac{S_t}{S_w} C_{y_b} \mathbf{b} \right)^2 \right\rangle +$$

$$+ 2 C_{L_a} (\mathbf{a} + \mathbf{a}_{o_L}) ng \mathbf{V} \mathbf{v}_\psi \frac{S_t}{S_w} C_{y_b} \mathbf{b} + C_{L_a}^2 (\mathbf{a} + \mathbf{a}_{o_L})^2 (\mathbf{V} \mathbf{v}_\psi)^2 + \left(ng \frac{S_t}{S_w} C_{y_b} \mathbf{b} \right)^2 - 2 C_{L_a} (\mathbf{a} + \mathbf{a}_{o_L}) ng \mathbf{V} \mathbf{v}_\psi \frac{S_t}{S_w} C_{y_b} \mathbf{b}$$

Simplifying,

$$\left[C_{L_a}^2 (\mathbf{a} + \mathbf{a}_{o_L})^2 + \left(\frac{S_t}{S_w} C_{y_b} \mathbf{b} \right)^2 \right]^2 = \left(\frac{V_o^2}{\bar{q} V^2} m \cos \tilde{\alpha} \right)^2 \left[\left\{ C_{L_a}^2 (\mathbf{a} + \mathbf{a}_{o_L})^2 + \left(\frac{S_t}{S_w} C_{y_b} \mathbf{b} \right)^2 \right\} \{ (ng)^2 + (\mathbf{V} \mathbf{v}_\psi)^2 \} \right]$$

$$C_{L_a}^2 (\mathbf{a} + \mathbf{a}_{o_L})^2 + \left(\frac{S_t}{S_w} C_{y_b} \mathbf{b} \right)^2 = \left(\frac{V_o^2}{\bar{q} V^2} m \cos \tilde{\alpha} \right)^2 \left[(ng)^2 + (\mathbf{V} \mathbf{v}_\psi)^2 \right]$$

$$(\mathbf{a} + \mathbf{a}_{o_L})^2 = \frac{1}{C_{L_a}^2} \left\{ \left(\frac{V_o^2}{\bar{q} V^2} m \cos \tilde{\alpha} \right)^2 \left[(ng)^2 + (\mathbf{V} \mathbf{v}_\psi)^2 \right] - \left(\frac{S_t}{S_w} C_{y_b} \mathbf{b} \right)^2 \right\}$$

$$\Rightarrow \mathbf{a} = \frac{1}{C_{L_a}} \sqrt{\left(\frac{V_o^2}{\bar{q} V^2} m \cos \tilde{\alpha} \right)^2 \left[(ng)^2 + (\mathbf{V} \mathbf{v}_\psi)^2 \right] - \left(\frac{S_t}{S_w} C_{y_b} \mathbf{b} \right)^2} - \mathbf{a}_{o_L} \quad (\text{Eqn. 17})$$

Substitute α into $\cos \phi_v$

$$\cos \mathbf{f}_v = \frac{1}{C_{L_a}^2 \left(\frac{1}{C_{L_a}} \sqrt{\left(\frac{V_o^2}{\bar{q} V^2} m \cos \tilde{\alpha} \right)^2 \left[(ng)^2 + (\mathbf{V} \mathbf{v}_\psi)^2 \right] - \left(\frac{S_t}{S_w} C_{y_b} \mathbf{b} \right)^2} - \mathbf{a}_{o_L} + \mathbf{a}_{o_L} \right)^2 + \left(\frac{S_t}{S_w} C_{y_b} \mathbf{b} \right)^2}$$

$$\cdot \frac{V_o^2}{\bar{q} V^2} m \cos \tilde{\alpha} \left[C_{L_a} \left(\frac{1}{C_{L_a}} \sqrt{\left(\frac{V_o^2}{\bar{q} V^2} m \cos \tilde{\alpha} \right)^2 \left[(ng)^2 + (\mathbf{V} \mathbf{v}_\psi)^2 \right] - \left(\frac{S_t}{S_w} C_{y_b} \mathbf{b} \right)^2} - \mathbf{a}_{o_L} + \mathbf{a}_{o_L} \right) ng + \mathbf{V} \mathbf{v}_\psi \frac{S_t}{S_w} C_{y_b} \mathbf{b} \right]$$

which simplifies to

$$\cos \mathbf{f}_v = \frac{1}{\left(\frac{V_o^2}{\bar{q}V^2} m \cos \tilde{\alpha} \right)^2 \left[(\text{ng})^2 + (\mathbf{v} \mathbf{v}_\Psi)^2 \right] - \left(\frac{S_t}{S_w} C_{y_b} \mathbf{b} \right)^2 + \left(\frac{S_t}{S_w} C_{y_b} \mathbf{b} \right)^2} \frac{V_o^2}{\bar{q}V^2} m \cos \tilde{\alpha} \cdot$$

$$\cdot \left[\left(\sqrt{\left(\frac{V_o^2}{\bar{q}V^2} m \cos \tilde{\alpha} \right)^2 \left[(\text{ng})^2 + (\mathbf{v} \mathbf{v}_\Psi)^2 \right] - \left(\frac{S_t}{S_w} C_{y_b} \mathbf{b} \right)^2} - \mathbf{a}_{o_L} + \mathbf{a}_{o_L} \right) \text{ng} + \mathbf{v} \mathbf{v}_\Psi \frac{S_t}{S_w} C_{y_b} \mathbf{b} \right]$$

\Rightarrow

$$\cos \mathbf{f}_v = \frac{\bar{q}V^2}{mV_o^2 \cos \tilde{\alpha} \left[(\text{ng})^2 + (\mathbf{v} \mathbf{v}_\Psi)^2 \right]} \left[\text{ng} \sqrt{\left(\frac{V_o^2}{\bar{q}V^2} m \cos \tilde{\alpha} \right)^2 \left[(\text{ng})^2 + (\mathbf{v} \mathbf{v}_\Psi)^2 \right] - \left(\frac{S_t}{S_w} C_{y_b} \mathbf{b} \right)^2} + \mathbf{v} \mathbf{v}_\Psi \frac{S_t}{S_w} C_{y_b} \mathbf{b} \right]$$

(Eqn. 15)

Substitute α into $\sin \phi_v$

$$\sin \mathbf{f}_v = \frac{1}{C_{L_a}^2 \left(\frac{1}{C_{L_a}} \sqrt{\left(\frac{V_o^2}{\bar{q}V^2} m \cos \tilde{\alpha} \right)^2 \left[(\text{ng})^2 + (\mathbf{v} \mathbf{v}_\Psi)^2 \right] - \left(\frac{S_t}{S_w} C_{y_b} \mathbf{b} \right)^2} - \mathbf{a}_{o_L} + \mathbf{a}_{o_L} \right)^2 + \left(\frac{S_t}{S_w} C_{y_b} \mathbf{b} \right)^2} \cdot$$

$$\frac{V_o^2}{\bar{q}V^2} m \cos \tilde{\alpha} \left[-C_{L_a} \left(\frac{1}{C_{L_a}} \sqrt{\left(\frac{V_o^2}{\bar{q}V^2} m \cos \tilde{\alpha} \right)^2 \left[(\text{ng})^2 + (\mathbf{v} \mathbf{v}_\Psi)^2 \right] - \left(\frac{S_t}{S_w} C_{y_b} \mathbf{b} \right)^2} - \mathbf{a}_{o_L} + \mathbf{a}_{o_L} \right) \mathbf{v} \mathbf{v}_\Psi + \text{ng} \frac{S_t}{S_w} C_{y_b} \mathbf{b} \right]$$

which simplifies to

$$\sin \mathbf{f}_v = \frac{1}{\left(\frac{V_o^2}{\bar{q}V^2} m \cos \tilde{\alpha} \right)^2 \left[(\text{ng})^2 + (\mathbf{v} \mathbf{v}_\Psi)^2 \right] - \left(\frac{S_t}{S_w} C_{y_b} \mathbf{b} \right)^2 + \left(\frac{S_t}{S_w} C_{y_b} \mathbf{b} \right)^2} \frac{V_o^2}{\bar{q}V^2} m \cos \tilde{\alpha} \cdot$$

$$\cdot \left[\left(\sqrt{\left(\frac{V_o^2}{\bar{q}V^2} m \cos \tilde{\alpha} \right)^2 \left[(\text{ng})^2 + (\mathbf{v} \mathbf{v}_\Psi)^2 \right] - \left(\frac{S_t}{S_w} C_{y_b} \mathbf{b} \right)^2} - \mathbf{a}_{o_L} + \mathbf{a}_{o_L} \right) \mathbf{v} \mathbf{v}_\Psi + \text{ng} \frac{S_t}{S_w} C_{y_b} \mathbf{b} \right]$$

⇒

$$\sin \mathbf{f}_v = \frac{\bar{q}V^2}{mV_o^2 \cos \tilde{\alpha} [(ng)^2 + (V \mathbf{v}_\psi)^2]} \left[-V \mathbf{v}_\psi \sqrt{\left(\frac{V_o^2}{\bar{q}V^2} m \cos \tilde{\alpha} \right)^2 [(ng)^2 + (V \mathbf{v}_\psi)^2]} - \left(\frac{S_t}{S_w} C_{y_b} \mathbf{b} \right)^2 + ng \frac{S_t}{S_w} C_{y_b} \mathbf{b} \right]$$

(Eqn. 16)

Solving the ~~V~~ equation

$$\mathbf{m} = \frac{\bar{q}V^2}{mgV_o^2} (C_{D_a} \mathbf{a} + C_{D_o}) + ng \sin \tilde{\alpha}$$

⇒

$$\mathbf{m} = \frac{\bar{q}V^2}{mgV_o^2} \left(\frac{C_{D_a}}{C_{L_a}} \sqrt{\left(\frac{V_o^2}{\bar{q}V^2} m \cos \tilde{\alpha} \right)^2 [(ng)^2 + (V \mathbf{v}_\psi)^2]} - \left(\frac{S_t}{S_w} C_{y_b} \mathbf{b} \right)^2 - C_{D_a} \mathbf{a}_{o_L} + C_{D_o} \right) + ng \sin \tilde{\alpha}$$

(Eqn. 18)

Trim Condition 9.

Inner-loop equations were defined above. The parameters weapon depression angle, height above the target and orbit radius were defined in Figure 10 in Chapter 3. The equations describing the orbit parameters follow

$$r_t = \frac{V^2}{g\sqrt{n^2 - 1}}$$

$$\mathbf{f}_v = \arccos\left(\frac{1}{n}\right)$$

$$h = r_t \tan(\mathbf{f}_v + \mathbf{e})$$

which combine to produce an equation for the height.

$$h = \frac{V^2}{g\sqrt{n^2-1}} \tan\left(\arccos\left(\frac{1}{n}\right) + e\right)$$

$$h = \frac{V^2}{g\sqrt{n^2-1}} \frac{\sqrt{1-\frac{1}{n^2} + \frac{1}{n} \tan e}}{\frac{1}{n} - \sqrt{1-\frac{1}{n^2} \tan e}}$$

$$\Rightarrow h = \frac{1 + \frac{1}{\sqrt{n^2-1}} \tan e}{1 - \sqrt{n^2-1} \tan e} \frac{V^2}{g} \quad (\text{Eqn. 38})$$

To find the maximum height, Equation 34 was differentiated with respect to n since e was constant

$$0 = -(n^2-1)^{-3/2} n \tan e (1 - \sqrt{n^2-1} \tan e) + \left(1 + \frac{1}{\sqrt{n^2-1}} \tan e\right) \frac{n}{\sqrt{n^2-1}} \tan e$$

which was simplified.

$$(n^2-1)^{-3/2} - \frac{\tan e}{n^2-1} = (n^2-1)^{-1/2} - \frac{\tan e}{n^2-1}$$

$$\frac{1}{n^2-1} = 1$$

$$\Rightarrow n_{\text{hmax}} = \sqrt{2}$$

$$\Rightarrow h_{\text{max}} = \frac{1 + \tan e}{1 - \tan e} \frac{V^2}{g} \quad (\text{Eqn. 39})$$

$$\Rightarrow \mathbf{f}_{v_{\text{max}}} = \arccos\left(\frac{1}{\sqrt{2}}\right) = 45^\circ$$

$$\Rightarrow r_{t_{\text{max}}} = \frac{V^2}{g\sqrt{\sqrt{2}^2-1}} = \frac{V^2}{g}$$

APPENDIX B: MATLAB® ROUTINE

This appendix includes a copy of the Matlab® routine used for the implementation of the open-loop model. The control surface deflections and engine settings were determined by varying the input parameters.

```

% Open-Loop Control Laws for AFIT Thesis
%   Capt Gary Miller
%   AFIT 2004
clear allclc
format compact
%
%   EQUILIBRIUM CONSTANTS
%   Determined by specific flight conditions
%W= 12712;           %A/C weight at equilibrium [lbs]
W= 13500;           %A/C weight at equilibrium [lbs]
S_w=231.8;         %A/C wing area [ft^2]
b=39.5;           %Wing span of the A/C [ft.]
c_bar=9;           %Wing mean chord [ft.]
S_t=76.5;         %Vertical Tail surface area [ft^2]
rho0=0.0023769;   %S-L standard density [slug/ft^3]
g=32.174;        %Force of gravity [ft/s^2]
R=1718;          %Universal gas const.[ft.lbs/slug*R]
m=W/g;           %Mass of A/C at equilibrium [slugs]
%
%   OUTER LOOP CALCULATIONS
%       Specify V/Vo, gamma and omega0 from flight conditions.
%       Beta or phi_v must also be specified.
%h0= 13879;        %specified%   %Equilibrium Height [ft] h0= 13879;
h0= 15000;        %specified%   %Equilibrium Height [ft]
T0=518.69-0.00356616*h0; %S-L standard temperature [deg. R]
%V=475;          %specified%   %Wind axes velocity [ft/s]
%Vo=475;         %specified%   %Wind axes equil. velocity [ft/s]
V=450;           %specified%   %Wind axes velocity [ft/s]
Vo=450;          %specified%   %Wind axes equil. velocity [ft/s]
psi_dot0=0.0;    %specified%   %Equilibrium turn rate [rad/s]
phi_dot0=0.0;    %specified%   %Equil. roll angle change [rad/s]
theta_dot0=0.0; %specified%   %Equil. pitch angle change [rad/s]
rho=rho0*exp(-g*h0/(R*T0)); %Density, altitude corr. [slug/ft^3]
gamma=0.0;       %specified%   %Normalllized flight path angle [rad]
                        %(defined up as positive)
q_bar=rho*(Vo^2)*S_w/2; %Dynamic pressure [lbs.]
C_y_beta=-0.0133*180/pi; %Side-Force Coeff.- sideslip [1/rad]
C_L_alpha=0.086694*180/pi; %Lift coeff.-angle of attack [1/rad]

```

```

C_L_o=0.010544; %Zero-lift lift coefficient [none]
C_Do=0.02350; %Zero-lift drag coefficient [none]
C_D_alpha=0.00200*180/pi; %Drag coeff.-angle of attack [1/rad]
flag0=1; %Flag0=1, beta specified; else phi
% Beta specified equations
if flag0==1; beta=-0.0; %Outer loop eqns. w/ beta specified
    phi=asin(q_bar*((V/Vo)^2)*(C_y_beta*beta*S_t*g/S_w-
psi_dot0*V*sqrt(...
    ((g^2+(psi_dot0*V)^2)*(m*((Vo/V)^2)*cos(gamma)/q_bar)^2)-...
    (C_y_beta*beta*S_t/S_w)^2))/(m*cos(gamma)*(g^2+(psi_dot0*V)^2));
    %Roll angle point mass eqn. [rad]
alpha=(sqrt((g^2+(psi_dot0*V)^2)*(((Vo/V)^2)*m*cos(gamma)/q_bar)^2-...
    (C_y_beta*S_t*beta/S_w)^2)-C_L_o)/C_L_alpha;
    %Angle of attack pt. mass eqn. [rad]
mu=q_bar*((V/Vo)^2)*(C_Do+C_D_alpha*(sqrt((g^2+(psi_dot0*V)^2)*(m*...
    ((Vo/V)^2)*cos(gamma)/q_bar)^2-(C_y_beta*beta*S_t/S_w)^2)-...
    C_L_o)/C_L_alpha)/W+sin(gamma); %Engine throttle setting
% Phi specified equations
else phi=0.0; %Outer loop eqns. w/ phi specified
beta=-((Vo^2)*W*S_w*cos(gamma)*sin(phi))/(C_y_beta*S_t*q_bar*(V^2));
    %Sideslip angle pt. mass eqn. [rad]
alpha=((Vo/V)^2)*W*cos(gamma)*cos(phi)/q_bar-C_L_o)/C_L_alpha;
    %Angle of attack pt. mass eqn. [rad]
mu=q_bar*((V/Vo)^2)*(C_Do-C_D_alpha*C_L_o/C_L_alpha)/W+...
    C_D_alpha*cos(gamma)*cos(phi)/C_L_alpha+sin(gamma);
    %Engine throttle setting
end;
if alpha>0.35; display('Angle of Attack limit exceeded'); end;
if mu<0;
display('Minimum Throttle setting exceeded, cannot maintain
equilibrium');
end
if mu>1; display('Maximum Throttle setting exceeded'); end;
%
% CONVERT A/C wind axis angles to body axis angles
psi=0.0; %specified% %A/C wind heading angle [rad]
c_11=cos(gamma)*cos(psi)*cos(alpha)*cos(beta)+(sin(phi)*sin(gamma)*...
    cos(psi)-cos(phi)*sin(psi))*cos(alpha)*sin(beta)-(cos(phi)*...
    sin(gamma)*cos(psi)+sin(phi)*sin(psi))*sin(alpha);
    %1st row, 1st column term matrix
c_21=cos(gamma)*sin(psi)*cos(alpha)*cos(beta)+(sin(phi)*sin(gamma)*...
    sin(psi)+cos(phi)*cos(psi))*cos(alpha)*sin(beta)-(cos(phi)*...
    sin(gamma)*sin(psi)-sin(phi)*cos(psi))*sin(alpha);
    %2nd row, 1st column term matrix
c_31=
-sin(gamma)*cos(alpha)*cos(beta)+sin(phi)*cos(gamma)*cos(alpha)*...
    sin(beta)-cos(phi)*cos(gamma)*sin(alpha);
    %3rd row, 1st column term matrix
c_32=sin(gamma)*sin(beta)+sin(phi)*cos(gamma)*cos(beta);
    %3rd row, 2nd column term matrix
c_33=
-sin(gamma)*sin(alpha)*cos(beta)+sin(phi)*cos(gamma)*sin(alpha)*...
    sin(beta)+cos(phi)*cos(gamma)*cos(alpha);
    %3rd row, 3rd column term matrix
if abs(-c_31)<pi/2; theta=asin(-c_31);

```

```

elseif (abs(sqrt(c_11^2+c_21^2))<pi) &
(abs(sqrt(c_11^2+c_21^2))>pi/2);
theta=pi-acos(sqrt(c_11^2+c_21^2));%A/C pitch angle <nav. axes> [rad]
end;
if abs(c_21/sqrt(c_11^2+c_21^2))<pi/2;
psil=asin(c_21/sqrt(c_11^2+c_21^2));
elseif (abs(c_11/sqrt(c_11^2+c_21^2))<pi) & (abs(c_11/sqrt(c_11^2+...
c_21^2))>pi/2);
psil=pi-acos(c_11/sqrt(c_11^2+c_21^2));
if psil>pi; psil=psil-pi; end; %Quadrant check
end; %A/C heading angle <nav. axes> [rad]
if abs(c_32/sqrt(c_11^2+c_21^2))<pi/2;
phil=asin(c_32/sqrt(c_11^2+c_21^2));
elseif (abs(c_33/sqrt(c_11^2+c_21^2))<pi) & (abs(c_33/sqrt(c_11^2+...
c_21^2))>pi/2);
phil=pi-acos(c_33/sqrt(c_11^2+c_21^2));
if phil>pi; phil=phil-pi; end; %Quadrant check
end; %A/C roll angle <nav. axes> [rad]
%
flag1=1; %Define Rotation Axis
if flag1==1; %=1>Yaw; =2>Pitch; =3>Roll
% CALCULATE ROTATION RATES FROM EULER ANGLES (STEADY TURN)
P=-psi_dot0*sin(theta); %Equilibrium Roll Rate [rad/s]
Q=psi_dot0*sin(phil)*cos(theta); %Equilibrium Pitch Rate [rad/s]
R=psi_dot0*cos(phil)*cos(theta); %Equilibrium Roll Rate [rad/s]
elseif flag1==2;
% CALCULATE ROTATION RATES FROM EULER ANGLES (PITCH-OVER)
P=0; %Equilibrium Roll Rate [rad/s]
Q=theta_dot0*cos(phil); %Equilibrium Pitch Rate [rad/s]
R=-theta_dot0*sin(phil); %Equilibrium Roll Rate [rad/s]
else
% CALCULATE ROTATION RATES FROM EULER ANGLES (STEADY ROLL)
P=phi_dot0; %Equilibrium Roll Rate [rad/s]
Q=0; %Equilibrium Pitch Rate [rad/s]
R=0; %Equilibrium Roll Rate [rad/s]
end;
% EQUILIBRIUM CONSTANTS
% AIRCRAFT MOMENTS OF INERTIA
I_xx= 20000; %Mom. of Inertia x-axes [slug*ft.^2]
I_yy= 22900; %Mom. of Inertia y-axes [slug*ft.^2]
I_zz= 40000; %Mom. of Inertia z-axes [slug*ft.^2]
I_xz= 1980; %Prod. of Inertia x/z [slug*ft.^2]
% AIRCRAFT STABILITY DERIVATIVES
C_y_delr= 0.002483*180/pi; %Side-Force Coeff.-rud. def. [1/rad]
C_y_dela= -0.00107*180/pi; %Side-Force Coeff.-ail. def. [1/rad]
C_l_beta= -0.00165*180/pi; %Roll Mom. Coeff.- sideslip [1/rad]
C_l_dela= -0.00138*180/pi; %Roll Mom. Coeff.- ail. def. [1/rad]
C_l_delr= 0.000346*180/pi; %Roll Mom. Coeff.- rud. def. [1/rad]
C_l_p= -0.44634*180/pi; %Roll Mom. Coeff.- Roll Rate [s/rad]
C_l_r= 0.387836*180/pi; %Roll Mom. Coeff.- Yaw Rate [s/rad]
C_n_beta= 0.001449*180/pi; %Yaw Mom. Coeff.- sideslip [1/rad]
C_n_dela= -0.00002*180/pi; %Yaw Mom. Coeff.- ail. def. [1/rad]
C_n_delr= -0.0009*180/pi; %Yaw Mom. Coeff.- rud. def. [1/rad]
C_n_p= -0.06415*180/pi; %Yaw Mom. Coeff.- Roll Rate [s/rad]
C_n_r= -0.11635*180/pi; %Yaw Mom. Coeff.- Yaw Rate [s/rad]

```

```

C_y_p= 0.149213*180/pi;           %Side-Force Coeff.-Roll Rate [s/rad]
C_y_r= 0.827684*180/pi;           %Side-Force Coeff.-Yaw Rate [s/rad]
C_l_pq= (I_xz*(I_zz+I_xx-I_yy)/(I_xx*I_zz-I_xz^2));
                                     %Roll Moment Coeff. due Pitch/Roll
C_l_qr= (I_zz*(I_yy-I_zz)-I_xx^2)/(I_xx*I_zz-I_xz^2);
                                     %Roll Moment Coeff. due Pitch/Yaw
C_n_pq= (I_xx^2-I_xx*I_yy+I_xz^2)/(I_xx*I_zz-I_xz^2);
                                     %Yaw Moment Coeff. due Pitch/Roll
C_n_qr= (I_xz*(I_yy-I_xx-I_zz))/(I_xx*I_zz-I_xz^2);
                                     %Yaw Moment Coeff. due Pitch/Yaw
C_mo= 0.052925;                    %Equil. Pitch Moment Coeff. [none]
C_m_dele= -0.01472*180/pi;         %Pitch Mom. Coeff.-elev. def.[1/rad]
C_m_q= -15.0857*180/pi;           %Pitch Mom. Coeff. due Pitch [s/rad]
C_L_q = 0.65200*180/pi;           %Lift Coeff. due Pitch[s/rad]
C_L_de = 0.006337*180/pi;         %Lift Coeff. due elev. Def. [1/rad]
C_m_alpha = -0.01557*180/pi;      %Pitch Mom. Coeff. due alpha [1/rad]
C_m_alpha_dot = -0.09800*180/pi;  %Pitch Mom. Coeff.-alpha_dot [s/rad]
C_d_q = 0.08600*180/pi;          %Drag Coeff. due Pitch Rate [s/rad]
C_m_p2r2= I_xz/I_yy;              %Pitch Mom. Coeff.-Roll Rate [s/rad]
C_m_pr= (I_zz-I_xx)/I_yy;         %Pitch Mom. Coeff.- Roll/Yaw [s/rad]
c_3=I_zz/(I_xx*I_zz-I_xz^2);      %Roll acc. eqn. const. [1/slug*ft^2]
c_4=I_xz/(I_xx*I_zz-I_xz^2);      %Roll/yaw eqns. const. [1/slug*ft^2]
c_7=1/I_yy;                       %Pitch acc. eqn. const.[1/slug*ft^2]
c_8=((I_xx-I_yy)*I_xx+I_xz^2)/(I_xx*I_zz-I_xz^2);
                                     %Yaw acc. eqn. const. [1/slug*ft^2]
c_9=I_xx/(I_xx*I_zz-I_xz^2);      %Yaw acc. eqn. const. [1/slug*ft^2]
% THRUST CHARACTERISTICS
x_T=0.1;                           %estimate%      %x-axis distance c.g. to thrust [ft]
y_T=3;                             %estimate%      %y-axis distance c.g. to thrust [ft]
z_T=0.1;                           %estimate%      %z-axis distance c.g. to thrust [ft]
T_max=5000;                         %estimate%      %Maximum combined thrust [lbs.]
alpha_T=0.0;                       %estimate%      %Engine thrust angle [rad]
T=mu*W;                             %Total engine trust [lbs.]
if T>T_max; display('Maximum thrust limit exceeded'); end;
per=0.5;                            %specified%     %Percentage of right engine thrust
T_1=per*T;                          %Thrust from right engine [lbs.]
T_2=T-T_1;                          %Thrust from left engine [lbs.]
% CONTROL SURFACE DEFLECTION LIMITS
dele_min= -0.2618;                  %Negative Elevator Def.Limit [rad]
dele_max= 0.2618;                  %Positive Elevator Def. Limit [rad]
dela_min= -0.5236;                 %Negative Aileron Def. Limit [rad]
dela_max= 0.5236;                 %Positive Aileron Def. Limit [rad]
delr_min= -0.6109;                %Negative Rudder Def. Limit [rad]
delr_max= 0.6109;                %Positive Rudder Def. Limit [rad]
% TRIM EQUATIONS
P_dot=0.0;                         %specified%     %Roll acceleration rate [rad/s^2]
Q_dot=0.0;                         %specified%     %Pitch acceleration rate [rad/s^2]
R_dot=0.0;                         %specified%     %Yaw acceleration rate [rad/s^2]
alpha_dot=0.0;                    %specified%     %Change in angle of attack [rad/s]
                                     %<related to theta_dot>%
c_p=-P_dot+C_l_pq*P*Q+C_l_qr*Q*R+c_3*y_T*sin(alpha_T)*(T_2-
T_1)+c_4*y_T*...
    cos(alpha_T)*(T_2-
T_1)+q_bar*b*(c_3*(C_l_p*P+C_l_r*R+C_l_beta*beta)+...
    c_4*(C_n_p*P+C_n_r*R+C_n_beta*beta));

```

```

                                %Roll acceleration equation constant
c_r=-R_dot+C_n_pq*P*Q-C_n_qr*Q*R+c_9*y_T*cos(alpha_T)*(T_2-
T_1)+c_4*y_T*...
    sin(alpha_T)*(T_2-
T_1)+q_bar*b*(c_9*(C_n_p*P+C_n_r*R+C_n_beta*beta)+...
    c_4*(C_l_p*P+C_l_r*R+C_l_beta*beta));
                                %Roll acceleration equation constant
den_lat=q_bar*b*((c_3*C_l_dela+c_4*C_n_dela)*(c_9*C_n_delr+c_4*C_l_delr
)...
    -(c_3*C_l_delr+c_4*C_n_delr)*(c_9*C_n_dela+c_4*C_l_dela));
                                %Denomenator lateral control eqns.
dela=(c_r*(c_3*C_l_delr+c_4*C_n_delr)-
c_p*(c_9*C_n_delr+c_4*C_l_delr))/...
    den_lat;                                %Aileron deflection equation [rad]
delr=(c_p*(c_9*C_n_dela+c_4*C_l_dela)-
c_r*(c_3*C_l_dela+c_4*C_n_dela))/...
    den_lat;                                %Rudder deflection equation [rad]
dele=(c_7*(z_T*cos(alpha_T)+x_T*sin(alpha_T))*(T)-C_m_pr*P*R-
C_m_p2r2*...
    (R^2-P^2)-Q_dot)/(C_m_dele*c_7*q_bar*c_bar)-
(C_m_o+C_m_alpha*alpha+...
    C_m_alpha_dot*alpha_dot+C_m_q*Q)/C_m_dele;
                                %Elevator deflection equation [rad]
if dela<dela_min; display('Aileron lower limit exceeded'); end;
if dela>dela_max; display('Aileron upper limit exceeded'); end;
if delr<delr_min; display('Rudder lower limit exceeded'); end;
if delr>delr_max; display('Rudder upper limit exceeded'); end;
if dele<dele_min; display('Elevator lower limit exceeded'); end;
if dele>dele_max; display('Elevator upper limit exceeded'); end;

```

BIBLIOGRAPHY

1. Stevens, Brian L. and Frank L. Lewis. *Aircraft Control and Simulation*. New York: John Wiley & Sons, Inc., 1992.
2. Payne, Jim. Class notes Unaugmented Trim & Stability Course, Flying Qualities Branch, United States Test Pilot School, Edwards AFB CA. April 2003.
3. Nelson, Robert C. *Flight Stability and Automatic Control*, 2nd Edition. Boston: McGraw-Hill Companies, Inc., 1998.
4. Schindeler, Nicholas J. and Meir Pachter. "Phugoid Dynamics Control," AIAA 2001 Guidance, Navigation, and Control Conference proceedings. AIAA paper No. A01-37036. Montreal, Canada: August 2001.
5. Hodgkinson, John. *Aircraft Handling Qualities*. Reston VA: J. S. Przemieniecki/AIAA Education Series, 1999.
6. NASA Dryden Flight Research Center. *Pushover-Pullup*. Edwards, CA. 24 October 2002 <http://www.dfrc.nasa.gov/trc/ftintro/push/naspopu.html>.
7. Russ Easter, Veridian Engineering. 5 Electronic messages. 17 September 2002 through June 2003.
8. Hall, James K. and Meir Pachter. "Formation Maneuvers in Three Dimensions," AIAA 2000 Guidance, Navigation, and Control Conference proceedings. AIAA paper No. A00-37128. Denver: August 2000.
9. Manning, Mary. Class notes Equations of Motion Course, Flying Qualities Branch, United States Test Pilot School, Edwards AFB CA. March 2003.
10. HAVE TRIM Test Team. "An Investigation of Open Loop Flight Control Equations of Motion Used to Predict Flight Control Surface Deflections at Non-Steady State Trim Conditions." Air Force Flight Test Center report, Edwards AFB CA. December 2003.

Vita

Captain Gary D. Miller graduated from Winfield High School in Winfield, Kansas. He completed undergraduate studies at the University of Kansas in Lawrence, Kansas with a Bachelor of Science degree in Aerospace Engineering in May 1993. He was commissioned through Officer Training School in Montgomery, Alabama in August 1995.

His first assignment was to the Oklahoma City Logistics Center at Tinker AFB, Oklahoma where he did flight test for the KC-135 with the 10 Flight Test Squadron for the KC-135 System Program Office modification programs. Following a three-year tour at Yokota AB, Japan working for the 315th Intelligence Squadron, he was selected for the dual Air Force Institute of Technology and United States Air Force Test Pilot School program. In September 2001, he entered the Graduate School of Engineering and Management, Air Force Institute of Technology. In January 2003, he entered United States Air Force Test Pilot School class 03A. Upon graduation, he will be assigned to the 40th Flight Test Squadron, Eglin AFB, Florida.

REPORT DOCUMENTATION PAGE

Form Approved
OMB No. 074-0188

The public reporting burden for this collection of information is estimated to average 1 hour per response, including the time for reviewing instructions, searching existing data sources, gathering and maintaining the data needed, and completing and reviewing the collection of information. Send comments regarding this burden estimate or any other aspect of the collection of information, including suggestions for reducing this burden to Department of Defense, Washington Headquarters Services, Directorate for Information Operations and Reports (0704-0188), 1215 Jefferson Davis Highway, Suite 1204, Arlington, VA 22202-4302. Respondents should be aware that notwithstanding any other provision of law, no person shall be subject to a penalty for failing to comply with a collection of information if it does not display a currently valid OMB control number.

PLEASE DO NOT RETURN YOUR FORM TO THE ABOVE ADDRESS.

1. REPORT DATE (DD-MM-YYYY) 03-03-2004		2. REPORT TYPE Master's Thesis		3. DATES COVERED (From - To) Sep 2001 - Feb 2004	
4. TITLE AND SUBTITLE OUTER-LOOP CONTROL IN ASYMMETRICAL TRIMMED FLIGHT CONDITIONS				5a. CONTRACT NUMBER	
				5b. GRANT NUMBER	
				5c. PROGRAM ELEMENT NUMBER	
6. AUTHOR(S) Miller, Gary D., Captain, USAF				5d. PROJECT NUMBER	
				5e. TASK NUMBER	
				5f. WORK UNIT NUMBER	
7. PERFORMING ORGANIZATION NAMES(S) AND ADDRESS(S) Air Force Institute of Technology Graduate School of Engineering and Management (AFIT/EN) 2950 Hobson Way, Building 641 WPAFB OH 45433-7765				8. PERFORMING ORGANIZATION REPORT NUMBER AFIT/GAE/ENY/04-M12	
9. SPONSORING/MONITORING AGENCY NAME(S) AND ADDRESS(ES) United States Test Pilot School (TPS) 220 S. Wolfe Ave. Edwards AFB, CA 93523 DSN 277-3000				10. SPONSOR/MONITOR'S ACRONYM(S)	
12. DISTRIBUTION/AVAILABILITY STATEMENT APPROVED FOR PUBLIC RELEASE; DISTRIBUTION UNLIMITED.				11. SPONSOR/MONITOR'S REPORT NUMBER(S)	
13. SUPPLEMENTARY NOTES					
14. ABSTRACT Traditionally flight control systems have used linearized equations of motion solved around a single trim point. This thesis proposes a nested-loop controller directly solved from the equations of motion. The control equations were developed as a solution to asymmetrically trimmed flight conditions. A two-loop design was proposed for the controller. The outer loop modeled the aircraft as a point mass and all forces were balanced to find the aircraft states. The equations input the control variables and output the aircraft states. The inner-loop utilizes the six-degree of freedom model of the aircraft to solve the moment equations. With the input states, the required control surface deflections are calculated. The control equations were investigated for typical flight conditions to find the predicted aircraft control settings. The control equations were implemented using aeromodel data for a Learjet-25. The predictions from the control equations were then compared to flight test results. The model was able to predict the required elevator deflection for simple longitudinal cases in level and climbing flight to within tolerances. The simple lateral-directional cases were not as accurate as the longitudinal investigations. As complex maneuvers were investigated, the model predictions did not match the flight test results.					
15. SUBJECT TERMS Flight Control, Equation of Motion (EOM), Trimmed Flight, Flight Test, Control Surface Deflection, Asymmetric Trimmed Flight, Aeromodel					
16. SECURITY CLASSIFICATION OF:		17. LIMITATION OF ABSTRACT		18. NUMBER OF PAGES	
REPORT	ABSTRACT	c. THIS PAGE	UU	145	19a. NAME OF RESPONSIBLE PERSON David R. Jacques, Dr. (ENY) david.jacques@afit.edu
U	U	U			19b. TELEPHONE NUMBER (Include area code) (937) 255-3355 x3329

Standard Form 298 (Rev: 8-98)
Prescribed by ANSI Std. Z39-18